Terahertz (THz) Waveguiding Architecture Featuring Doubly-Corrugated Spoofed Surface Plasmon Polariton (DC-SSPP): Theory and Applications in Micro-Electronics and Sensing

by

Zhao Xu

A dissertation submitted in partial fulfillment
of the requirements for the degree of
Doctor of Philosophy
(Electrical Engineering)
in the University of Michigan
2017

Doctoral Committee:

Professor Pinaki Mazumder, Chair
Professor Igor L. Markov
Emeritus Professor Michael J. Welsh
Professor Herbert G. Winful

Dedication

To my dearest wife Jia, and all my family supporting me throughout these years of scientific research and endeavor

Acknowledgement

I would like to express the deepest appreciation to my academic advisor and committee chair Professor Pinaki Mazumder, who has the attitude and the substance of a genius: he continually and convincingly conveyed a spirit of adventure in regard to research and scholarship and an excitement in regard to teaching. Without his guidance and persistent help, this dissertation would not have been possible.

I would like to equally thank the rest of my committee members, Professor Igor Markov, Emeritus Professor Michael Welsh, and Professor Herbert Winful, for their insightful comments and encouragement to widen my research from various perspectives.

I would also like to express my sincere gratitude to my colleague Kyungjun Song, who has pioneered the exploration of metamaterials and plasmonic nano-architectures. His excellent work has led me into this outstanding field of research and has offered great insight that leads to my success. I thank my fellow lab-mates for all the stimulating discussions, for the long days and sleepless nights we were working together, and for all the fun we have had in the past years.

TABLE OF CONTENTS

List of Tables

List of Figures

Abstract

Terahertz (10^{12} Hz) has long been considered a missing link between microwave and optical IR spectra. This frequency range has attracted enormous research attentions in recent years, with ever-growing anticipation for its applications in remote sensing, molecular spectroscopy, signal processing and next-generation high-speed electronics. However, its development has been seriously hindered by the lack of waveguiding and manipulating architectures that could support the propagation of THz radiations without excessive signal distortion and power loss.

Facing this challenge, this work exploits the spoofed surface plasmon polariton (SSPP) mode of the THz oscillation and introduces the doubly corrugated SSPP (DC-SSPP) architecture to support sub-wavelength, low-dispersion THz transmission. DC-SSPP displays unique bandgap structure, which can be effectively modulated via structural and material variables. These unequaled properties make DC-SSPP the ideal solution to support not only signal transmission but also THz sensing and THz-electronics applications. In this thesis, theoretical analysis is carried out to thoroughly characterize the THz propagation, field distribution and transmission band structures in the novel architecture. Via numerical approximation and finite element simulations, design variations of the DC-SSPP are further studied and optimized to fulfill application-specific requirements. We demonstrate effective DNA sensing by adopting the Mach-Zehnder interferometer (MZI) or waveguide-cavity-waveguide insertions, which showed detectability with minuscule sample size even in the aqueous environment. We manifest high-speed analog-to-digital conversion via a combination of MZI DC-SSPP with nonlinear, partial-coupling detector arrays. Full characterization of the proposed ADC is carried out where high operation speed, small signal distortion, and great output linearity is shown.

Also included in this work is a detailed review of the THz emitters and detectors, which are indispensable constituents of the THz system discussed herein. The future of the DC-SSPP in building THz bio-computing and THz digital circuits, considered as the next step of this research work, is also explored and demonstrated with the novel concept of directed logic network.

CHAPTER I Introduction

1.1 Terahertz: the new frontier

The invention of p-n junction diodes and other solid-state carrier-manipulating elements opened the door of modern electronics in the middle of last century. Since then, the continuous effort of device miniaturization and system integration has brought the field of micro-electronics into a whole new level, where clusters of nano-scale structures can be utilized for data processing with frequency reaching up to tens of gigahertz (GHz) [1, 2, 3]. The design of integrated circuit (IC) chips is therefore widely implemented, where millions of transistors meticulously interconnected can be packed into a small volume. Nowadays various IC chips are employed in almost every corner of the world to realize complicated functions that people use daily in their work and personal lives.

While the very large scale integrated circuits (VLSI) serves as the backbone for in-chip data manipulation and processing, transmission of the electronic signal over distance brought about new obstacles. Waveguiding structures such as co-axial cables and other transmission lines experience signal propagation loss, therefore needs repetitive relay stages that consist of receivers, amplifiers, and emitters. The slow nature of the electronics, as well as the corresponding transmission architectures, limits the bandwidth of the signal transmission, preventing the fast delivery of large amounts of data. In addition, the bulkiness of the transmission line presents issues of cost, maintenance, and deployability. Such difficulties can be best circumvented by using optical waves for data carriage and optical fibers as the transmission media. Introduced in the late 1960s, optical fibers can transmit signals with wavelengths in the range of hundreds of nanometers to several microns. This has brought about a potential bandwidth of $\sim 10^{15}$ Hz, compared with the range of GHz in electronics. In addition, by proper design, optical fibers can operate in the single mode with ultra-low insertion loss and near-zero dispersion. All these properties have made the optical fibers the sole candidate for building long-distance communication and data transmission trunk lines.

Optics and electronics have been developed in parallel for decades before their integration became the natural object to pursue. The ultimate goal is to combine the speed and wide bandwidth of optics with the solid-state monolithic footprint matured in modern integrated electronics. A critical challenge for the convergence of optics and electronics is that the micron scale of optics is significantly larger than the nanometer scale of modern electronic devices [4]. The conversion from photons to electrons is therefore highly inefficient as a result of such incompatibility, resulting in huge power penalty and excessive loss [5, 6, 7]. In light of these difficulties, terahertz (THz) frequencies have been proposed as the potential inter-stage between electronics and optics. With ~1/100 of the conventional optical frequency, THz radiations are more likely to be resonantly coupled into electronic devices [8, 9]. The surface plasmonic mode for THz transmission makes the signal coupling structure sub-wavelength, which can best match the diffraction-limited spot size of the incident signal [10, 11, 12]. The speed and bandwidth of the electro-optic circuit nowadays are by far limited by the electronics, which in turn is determined by the carrier mobility as well as other factors such as loading and parasitic impedances. In this sense, employing THz in lieu of optical frequency shall minimally affect the bandwidth of the hybrid system, if at all.

Moreover, in the past decade or so, THz frequencies are found to be essential in a variety of other applications including imaging, bio-sensing, and spectroscopy. Unlike visible and near- to mid-infrared light, electro-magnetic waves in THz frequencies can penetrate most dry, nonmetallic and nonpolar objects commonly seen in daily life, including paper, wood, and plastics [13]. At the same time, it allows spectroscopic identification of chemical substances and compounds, including semiconductor materials, through their characteristic molecular fingerprints [14, 15]. It can, therefore, be used in various applications such as astronomical remote sensing, environment monitoring, production line quality control, and homeland security systems [16, 17, 18, 19, 20]. In recent years, THz bio-sensing has also emerged as a hot research area as a result of the characteristic vibrational resonances of macro-molecules, such as proteins, enzymes, and DNA/RNAs, which are largely in this frequency range. A non-invasive, tag-free sensing scheme can be therefore realized using THz probing beams, which can overcome many disadvantages of the widely-used fluorescent tagging method [21, 22, 23, 24].

Despite its potential application in a wide range of areas, integration of THz radiation in most of the circumstances requires reliable means of transmission and manipulation of the signal. Due to the unique properties of most of the materials when THz radiations present, the waveguiding of the signal at these frequencies needs to be different from other conventional ways typically seen in electronic and photonic domains. The goal is to discover a mechanism, which can transmit THz waves with small loss, low dispersion, and preferably with small dimensions that are comparable with electronic standards.

1.2 THz transmission: challenges and limitations

Electromagnetic oscillations in the majority of media can be described by the Lorentz model, which depicts the charge carriers as forced harmonic oscillators with damping. As a result, the electric susceptibility of any material comprising such charge carriers can be expressed as:

$$\chi(\omega) = \frac{1}{\omega_0^2 - \omega^2 + i\omega\gamma} \frac{Ne^2}{\varepsilon_0 m^*} = \frac{\omega_p^2}{\omega_0^2 - \omega^2 + i\omega\gamma} \tag{1}$$

The variables in the above equation are summarized in Table 1. This susceptibility, in general, predicts the existence of dispersion and resonant absorptions in dielectric materials. When a sandwiched structure is formed by several layers of dielectrics with step-like susceptibility differences, transverse modes with either oscillating or evanescent nature can be formed in different layers, giving rise to the mode confinement. In this case, waveguiding can be realized, which is referred to as index-guiding mechanism.

TABLE 1 LIST OF VARIABLES IN THE GENERAL SUSCEPTIBILITY MODEL

ε_0	Dielectric constant of vacuum
ω_p	Plasmonic resonance frequency
ω_0	Dipole resonance frequency
ω	Frequency
γ	Relaxation constant
N	Free carrier concentration
e	Charge of electron
m^*	Effective mass of electron

In optical frequencies, the conventional index-guiding method is employed in optical fibers. A fiber core, usually with the diameter of several to several tens of microns, is surrounded by a much thicker cladding layer to provide the refractive index difference in order to confine the

signal field inside the fiber. Single mode fiber is the most widely used fiber type. Its core size needs to comply with the following criteria in order to have the single-mode operation:

$$D < \frac{2.4048\lambda}{\pi\sqrt{n_1^2 - n_2^2}} \tag{2}$$

In the above equation, D is the diameter of the fiber core, λ is the wavelength, n_1 and n_2 are the refractive indices of the core and cladding respectively. Depending on the wavelength and choice of materials, the fiber core size can be adjusted accordingly. In the current international standard (ISO/IEC 11801) for single mode fiber (SMF) working in telecommunication wavelengths (1310 nm and 1550 nm), the core and cladding diameters are set to be 9 μm and 125 μm respectively. SMF has relatively large dimensions compared with the wavelength of the light traveling within. It is therefore considered as the opposite to the so-called sub-wavelength transmission, which is aimed at transmitting signals with smaller-than-wavelength structures.

In THz domain, the application of the same index-guiding method is deemed as impractical when the size of the optical fibers needs to be proportionally enlarged by an order of ~100. What's more, the high loss coefficient of dielectric materials in THz range also prevents the signal from propagating over long distances [25, 26, 27]. In order to miniaturize the waveguiding architecture and minimize the loss, the most effective solution is to employ a mode with tight field confinement. Fortunately, surface modes with such properties do exist on dielectric-metal interfaces, known as the surface plasmon (SP).

In metal, as a result of free carriers, we have $\omega_0 = 0$ in (1). Therefore the equation becomes:

$$\chi(\omega) = -\frac{1}{\omega^2 - i\omega\gamma}\frac{Ne^2}{\varepsilon_0 m^*} \tag{3}$$

This susceptibility leads to the surface plasmon mode which is evanescent in both the metal and the dielectric, making the sub-wavelength transmission possible. In physics, the surface plasmon is explained as the charge density oscillation of a 2-dimensional electron gas (2-DEG) in metal, in accordance with the *E-M* oscillation in the dielectrics. The hybridized excitation is therefore referred to as the surface plasmon polariton (SPP). Such mode can exist prevalently in optical domain on common dielectric and metal interfaces, as the refractive index of metal has a small negative real part and a small imaginary part in optical frequencies.

The potential of using SPP mode for THz transmission is, however, difficult. The permittivity of metal in this frequency range will have a huge negative real part, indicating weak confinement of the mode in the proximity of the surface. In order to have similar strongly localized mode profile for *E-M* waves in THz frequencies, modifications need to be made to the waveguiding architectures, and as a result, a spoofed surface plasmon polariton transmission mechanism can be realized.

1.3 Spoofed surface plasmon polaiton (SSPP)

In the effort of realizing surface mode-like THz propagation, various structures have been employed and studied. For example, K. Wang *et al.* first proposed the transmission of THz radiation as a radially polarized mode on metal wires [28]. Due to the small surface area of the metal wire, the loss is shown to be much smaller than any conventional waveguiding structures available at that time. The TEM-like dispersion relation also minimized the group velocity dispersion, which is critical for time-domain applications where pulsed THz radiations are typically used.

The real breakthrough in THz waveguiding technology, however, struck the area when Pendry *et al.* discovered the connection between intrinsic surface plasmons on the smooth metal surface and the surface mode generated when a conductive surface is modified with sub-wavelength, periodic features [29]. Such features can be holes, slits, or dimples. Although extraordinary optical transmission for light impinging on such surfaces has been observed even before Pendry's work, the main contribution of this work is to conclude that the enhanced sub-wavelength transmission and *E-M* field localization can be explained by the existence of "spoofed" surface plasmon mode on the modified surfaces. Such mode is characterized by an effective permittivity of the structure as a whole. For example, for a conductive surface with a 2-dimensional periodic array consisting of squared holes of the dimension of $a \times a$, the effective permittivity can be expressed as:

$$\varepsilon_{eff} = \frac{\pi^2 d^2 \varepsilon_h}{8a^2}\left(1 - \frac{\pi^2 c_0^2}{a^2 \omega^2 \varepsilon_h \mu_h}\right) = \varepsilon\left(1 - \frac{\omega_p^2}{\omega^2}\right) \tag{4}$$

Where

$$\varepsilon = \frac{\pi^2 d^2 \varepsilon_h}{8a^2} \tag{5}$$

$$\omega_p = \frac{\pi c}{a\sqrt{\varepsilon_h \mu_h}} \tag{6}$$

In the above equations, d is the period of the square holes, ε_h and μ_h are the permittivity and permeability of the material that may be filling the holes, and c_0 is the speed of light in vacuum. It is obvious that ε_{eff} mimics the permittivity of metal, where intrinsic surface plasmon mode at optical frequencies is originally observed.

Moreover, the effective permittivity is apparently dependent on the geometric dimensions as well as the choice of materials of the modified surface. In this sense, the significance of Pendry's work not only lies in the unified theoretical treatment of the (spoofed) surface plasmon on smooth/modified surfaces, but also in the fact that such effective plasmonic resonance can be modified by adjusting the design of the periodic surface features. This has opened whole new vistas for the designer surface mode with almost arbitrary dispersion in frequency and in space, including the extension of it into THz domains.

Following Pendry's work, various conductive surfaces with periodic features are studied by different research groups for the transmission, guiding and focusing of *E-M* radiations, a lot of which are at THz frequencies. Maier *et al.* proposed metal wire structures with a periodic array of radial grooves for the transmission of THz waves [30]. Compared with Wang's work, the corrugated metal wire shows better confinement of the propagating signal and can be tailored by different designs of the grooves. Superfocusing can also be realized by forming the corrugated metal wire into a conical shape. Ultrawide bandwidth slow light structure has been designed by Q. Gan *et al.*, where a corrugated metallic grating structure with gradient groove depth are used to slow down the THz propagating signal [31]. The wide bandwidth covering 0.6-0.9THz is realized by the fact that grooves with different depth have different spoofed surface plasmon resonance frequencies. Fernandez-Dominguez *et al.* have proposed a corrugated, v-shaped channel with sub-wavelength lateral dimensions [32]. Using FDTD simulations, they have shown that such architecture has long propagation length for THz radiations and small bending loss, therefore can be potentially used for routing THz waves at planar surfaces.

C. R. Williams *et al.* have both quasi-analytically and numerically studied the metal surface decorated with 2-D periodic square pits [10]. They also performed experiments to characterize the mode confinement factor by using an aperture formed by a razor blade. An increase of approximately two orders of magnitude in terms of mode confinement has been observed for the modified surface compared with flat ones. This work proves the theoretical prediction in Pendry's work, where strong mode localization within the surface features is anticipated. The extraordinary optical transmission through sub-wavelength holes in metal films with periodic surface modifications is best summarized in the review paper by Garcia-Vidal *et al.*, in which analytical tools are used to study the enhanced transmission of THz radiation through surfaces decorated with various features, including single aperture, array of apertures and apertures flanked with periodic corrugations [33]. The beaming, collimation, and routing of the THz radiation have also been demonstrated with the 2-D periodically decorated surfaces by works of several other research groups [11, 34, 35, 36, 37].

Among those structures, metal-dielectric interface corrugated with 1-D periodic grooves are of particular interest. Compared with conductive surfaces with 2-D modifications where the incident wave in most cases impinges in the normal direction, in the corrugated structure, the THz wave propagates in parallel with the metal-dielectric interface, resulting in longer interaction distances. This unique property is essential in many applications, such as active device and sensor designs, where the responsivity of the THz wave to the external stimuli needs to be maximized. It is also relatively easy to fabricate, making it readily implementable with current monolithic fabrication techniques.

1.4 1-D periodic corrugated SSPP architecture

1-dimensional periodic groove structure in microwave domain has been studied decades back. It has been used to generate and amplify microwave signals, taking advantage of its slow wave nature. The theoretical characterization of the *E-M* waves scattering off single or multiple square-shaped corrugations has been provided in the work of J. Esteban *et al.* and Y.-L. Kok [38, 39, 40]. In both the works the corrugated waveguiding structure is divided into multiple regions. Field equations are written out in each of the regions and boundary conditions are used to match the modes at discontinuities. In the work of Esteban *et al.*, the structure is treated as a transmission line and as a result, admittance matrices are used to form an eigenvalue problem.

Corrugated waveguides with both circular and rectangular cross-sections can be characterized using this method, both of which are common waveguide types seen at microwave frequencies. Y.-L. Kok, on the other hand, used scattering matrices and Bessel series representation of the scattered field angular spectrum. The effect of multiple grooves is treated as a combination of single groove diffractions and their cross-couplings. Numerical methods for root-finding are used in both works, and dispersion relation for the complex modes can be obtained.

When the corrugations are periodic, the problem can be greatly simplified by using Floquet mode expansion to represent the effect of the structural periodicity. Such problem is first treated by Collin, where a dispersion relation with asymptotic limit and discrete transmission band is demonstrated [41]. Collin's method served as the basis for treating similar structures in the years to follow, including works by B. D. McVey *et al.* and J. Joe *et al.* on the design of microwave amplifiers with sub-wavelength periodic grooves [42, 43]. A. A. Maragos *et al.* expanded the formulation to include structures with arbitrary groove dimensions and a numerical algorithm has been developed accordingly [44]. Only recently has the mathematical formulation been applied to THz frequencies. Metal surfaces with 1-D periodic grooves are studied for applications such as travelling wave tubes (TWT), backward wave oscillators (BWO) and beam routers in THz frequencies [45, 46, 47]. In those works the dispersion relation of the THz SSPP mode supported by the corrugated structures is calculated to have the same asymptotic nature as its counterparts in the microwave range. Numerical simulations, as well as experiments, have been carried out to verify the theoretical calculations.

Despite the fact that the 1-D corrugated metal surface has been studied intensively in both microwave and THz domains, only one-sided corrugation is used as the waveguiding structure in almost all the cases as stated above. With this structure, the THz field in the dielectric layer is always evanescent, vanishing at the terminating smooth metal surface or at infinity. It is always interesting, however, to consider the case where two corrugated conductive surfaces are placed opposite to each other to form a closed waveguide. The cross-coupling of groove diffractions, in this case, will happen not only between corrugations on one side of the structure but also between those on opposing sides. Such unique property could give rise to novel SSPP behaviors, which can be applied to various applications when properly designed. The analytical treatment of

the doubly-corrugated structure by itself, on the other hand, can serve as an important supplementation to the theoretical framework of the 1-D grooved structure as a whole.

In this thesis, THz waveguiding structure comprising two 1-D periodically grooved metal-dielectric interfaces placed vis-a-vis, named doubly-corrugated spoofed surface plasmon polariton (DC-SSPP) architecture is thoroughly studied. Such structure is shown to have surface-plasmon-like dispersion relation and discrete transmission bands. Its spectral output strongly depends on the geometric dimensions of the grooves and their periodicity, as well as the choice of dielectric materials. Moreover, a super-flat mode with near-zero group velocity can be supported in the DC-SSPP structure, which is a unique feature as a result of its mirror-symmetry. Various applications including sensing and analog-to-digital conversion can be realized using the designer SSPP mode of this architecture.

In Chapter II a complete mathematical treatment of the DC-SSPP structure based on full-field analysis will be described in detail. Using similar method as dividing the waveguide into separate regions, 3-dimensional *E-M* fields are written out in all regions and boundary conditions are used to connect them together. The symmetry of the DC-SSPP structure dictates symmetry of the transverse mode profile. Both symmetric and anti-symmetric modes are studied using our analytical model and their dispersion relations can be obtained. Moreover, the S-parameters can also be theoretically calculated and as a result, the transmission property of the structure can be obtained. Calculation results are compared with simulations and their validity is tested.

Chapter III introduces the combination of two DC-SSPP waveguides to form a Mach-Zehnder interferometer (MZI). The phase information of the THz signal propagating in both branches, which can also be predicted by the analytical model, can be extracted by the means of interference. The combination of the amplitude and phase selectivity of the MZI structure results in much sharper spectral features. In application, a DNA sensing element is designed which can effectively distinguish between single-stranded and double-stranded DNA molecules by depositing the bio-samples on one branch of the MZI. The highly localized field at frequencies close to SSPP resonance is shown to reduce the sample amount needed to produce interference patterns without affecting the selectivity of the sensing structure.

Chapter IV reviews the beam steering effect of the MZI DC-SSPP structure and the possibility of active control with external stimuli. Doped semiconductor materials are used to partially fill the groove area, and modulation of the free carrier concentration is used to modulate the phase of the traveling THz signal. Effective beam deflection in both enhancement and depletion modes are studied in detail. The rest of the chapter will be dedicated to the design of an analog-to-digital converter (ADC) using THz wave based on the beam bender structure. A differential implementation and use of nonlinear detector arrays enable a 3-bit ADC with a direct digitized output. Both theoretical analysis and numerical simulation demonstrate the critical specifications of this ADC design including linearity, effective number of bits (ENOB), and operation bandwidth.

In Chapter V, a review session will be provided on the THz emitters and detectors. With well-known difficulties in traditional thermal- and photovoltaic-based THz generation/detection, this chapter will summarize several state-of-the-art, room temperature solutions employing wave-mixing, semiconductor photoconductive effect, and resonant tunneling diode (RTD). Facing particular challenges with the footprint and working frequency range in the DC-SSPP THz applications, novel approaches of monolithic THz generation and detection are also discussed in detail, where exceptional material and smart architecture designs are adopted.

The last chapter of this thesis will be dedicated to the potential application of the DC-SSPP THz architecture in digital Boolean logic circuitry. The fundamentals of the directed logic concept are introduced as the solution to small-latency, ultrafast logic networks. Featuring narrow band structure, a modified DC-SSPP architecture is proposed as the universal building block for a 2-D directed logic network utilizing THz frequencies. A DC-SSPP directed logic node is demonstrated to function via its frequency-selective transmission. Most interestingly, external stimuli of various forms are shown to effectively reconfigure the logic nodes to any desired Boolean functionality. This unique phenomenology is manifested to be used to realize 2-D digital logic networks and even revolutionary ideas such as bio-computing.

CHAPTER II Doubly-Corrugated Spoofed Surface Plasmon Polariton (DC-SSPP) Architecture: Theoretical Analysis

2.1 Dispersion relation

The doubly-corrugated SSPP structure under investigation consists of dielectric materials surrounded by metal and is illustrated in Figure 1. The structure is in general divided into two regions: Region I is the waveguiding dielectric section without corrugations, and Region II represents the periodic groove areas. In our conventions, d is the period of the grooves, a and h are the width and depth of the grooves respectively, $2t$ is the height of the smooth part of the structure, and W represents the width of the structure. The coordinate system is also shown in Figure 1, with $z = 0$ positioned at the mid-point of the structure and $x = 0$ at the center of one of the grooves.

Based on Maxwell's Equations, mathematical expressions of the *E-M* fields are explicitly written out for both Region I and Region II. As is common in the treatment of structures with similar geometry, the x-dependency of the *E-M* field is best expressed by a Floquet mode expansion due to the periodic nature of the structure [41, 42, 44]. The mirror symmetry of the structure also indicates that the field distribution along z-axis must be either symmetric or anti-symmetric. In other words, the z-dependency of mode distributions needs to be in the form of either *cosine* or *sine* functions. This term represents the cross-coupling of field diffraction off the grooves on the opposite corrugations of the structure.

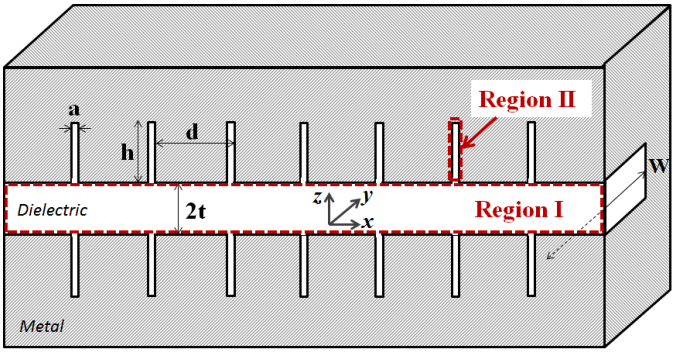

Figure 1: Cross-section of the single-armed DC-SSPP structure with different geometric dimensions labeled. *W* is the width of the waveguide along the *y*-direction. The structure can be divided into Region I and Region II as shown in the sketch

In our convention, we refer to the symmetry of our modes using the *y*-polarized *H*-field. Therefore for anti-symmetric modes, the *E-M* fields in both regions are expressed as:

In Region I:

$$\begin{bmatrix} H_x^I \\ H_y^I \\ H_z^I \end{bmatrix} = \sum_{n=-\infty}^{\infty} \rho_n e^{jk_{x,I}^{(n)}x} \begin{bmatrix} j\dfrac{k_y k_{x,I}^{(n)}}{\nu_y^2}\cos(k_y y)\sin\left(k_{z,I}^{(n)}z\right) \\ \sin(k_y y)\sin\left(k_{z,I}^{(n)}z\right) \\ \dfrac{k_y k_{z,I}^{(n)}}{\nu_y^2}\cos(k_y y)\cos\left(k_{z,I}^{(n)}z\right) \end{bmatrix} \tag{7}$$

$$\begin{bmatrix} E_x^I \\ E_y^I \\ E_z^I \end{bmatrix} = \frac{1}{\omega\epsilon}\frac{k_0^2}{\nu_y^2}\sum_{n=-\infty}^{\infty} \rho_n e^{jk_{x,I}^{(n)}x}\sin(k_y y) \begin{bmatrix} -jk_{z,I}^{(n)}\cos\left(k_{z,I}^{(n)}z\right) \\ 0 \\ -k_{x,I}^{(n)}\sin\left(k_{z,I}^{(n)}z\right) \end{bmatrix} \tag{8}$$

In Region II:

$$\begin{bmatrix} H_x^{II} \\ H_y^{II} \\ H_z^{II} \end{bmatrix} = \begin{bmatrix} -\dfrac{k_y k_{x,II}}{\nu_y^2}\left(A^+e^{jk_{z,II}z} + A^-e^{-jk_{z,II}z}\right)\cos(k_y y)\sin(k_{x,II}x) \\ \left(A^+e^{jk_{z,II}z} + A^-e^{-jk_{z,II}z}\right)\sin(k_y y)\cos(k_{x,II}x) \\ j\dfrac{k_y k_{z,II}}{\nu_y^2}\left(A^+e^{jk_{z,II}z} - A^-e^{-jk_{z,II}z}\right)\cos(k_y y)\cos(k_{x,II}x) \end{bmatrix} \tag{9}$$

$$\begin{bmatrix} E_x^{II} \\ E_y^{II} \\ E_z^{II} \end{bmatrix} = \frac{1}{\omega\epsilon}\frac{k_0^2}{\nu_y^2}\sin(k_y y) \begin{bmatrix} k_{z,II}\left(A^+e^{jk_{z,II}z} - A^-e^{-jk_{z,II}z}\right)\cos(k_{x,II}x) \\ 0 \\ -jk_{x,II}\left(A^+e^{jk_{z,II}z} + A^-e^{-jk_{z,II}z}\right)\sin(k_{x,II}x) \end{bmatrix} \tag{10}$$

In the above expressions, $k_{x,I}^{(n)}$ and $k_{z,I}^{(n)}$ denote the wavevectors of the n^{th}-order Floquet mode along *x*- and *z*-axis in Region I, and ρ_n signifies its amplitude coefficient. Correspondingly, $k_{x,II}$ and $k_{z,II}$ denote the wavevectors along the two axis in Region II. Other variables are defined as follows

$$v_y^2 = k_0^2 - k_y^2 = \left(k_{x,I}^{(n)}\right)^2 + \left(k_{z,I}^{(n)}\right)^2 \text{ in Region I}$$

$$v_y^2 = k_0^2 - k_y^2 = k_{x,II}^2 + k_{z,II}^2 \text{ in Region II, and}$$

$$k_y = \frac{m\pi}{W}, m = 1,2, \ldots$$

$$k_{x,II} = \frac{l\pi}{a}, l = 0,1,2, \ldots$$

By expressing the *E*-*M* field distributions using above expressions, these modes automatically satisfy the boundary conditions that the tangential *E*-field and normal *H*-field shall vanish at all dielectric-metal interfaces. In addition, boundary conditions at the interface between Region I and Region II requires the transverse *E*-*M* field to be continuous:

$H_y^I = H_y^{II}$:

$$\sum_{n=-\infty}^{\infty} \rho_n \sin(k_y y) \sin\left(k_{z,I}^{(n)} t\right) e^{jk_{x,I}^{(n)} x} = \left(A^+ e^{jk_{z,II}t} + A^- e^{-jk_{z,II}t}\right) \sin(k_y y) \cos(k_{x,II} x) \tag{11}$$

$E_x^I = E_x^{II}$:

$$-\frac{1}{\omega\epsilon}\frac{k_0^2}{v_y^2} \sum_{n=-\infty}^{\infty} jk_{z,I}^{(n)} \rho_n \sin(k_y y) \cos\left(k_{z,I}^{(n)} t\right) e^{jk_{x,I}^{(n)} x} = \frac{1}{\omega\epsilon}\frac{k_0^2}{v_y^2} k_{z,II} \left(A^+ e^{jk_{z,II}t} - A^- e^{-jk_{z,II}t}\right) \sin(k_y y) \cos(k_{x,II} x) \tag{12}$$

In our structure, *a* is small compared to the wavelength of the propagating field. As a result higher order modes in Region II as denoted by the expression $k_{x,II} = \frac{l\pi}{a}, l = 0,1,2, \ldots$ are always evanescent in all other directions. It is therefore safe to assume that only the lowest order of the $k_{x,II}$ modes is significant in our calculation. In that condition if we denote $B^+ = A^+ e^{jk_{z,II}t}$ and $B^- = A^- e^{-jk_{z,II}t}$, for any given order of $k_y = \frac{m\pi}{W}, m = 1,2, \ldots$the above equations can be simplified as:

$$\sum_{n=-\infty}^{\infty} \rho_n \sin\left(k_{z,I}^{(n)} t\right) e^{jk_{x,I}^{(n)} x} = B^+ + B^- \tag{13}$$

$$-\sum_{n=-\infty}^{\infty} jk_{z,I}^{(n)} \rho_n \cos\left(k_{z,I}^{(n)} t\right) e^{jk_{x,I}^{(n)} x} = k_{z,II}(B^+ - B^-) \tag{14}$$

By integrating both sides of (13) and (14) for one period along *x*-axis, and by imposing boundary conditions such that tangential *E*-field must vanish at the horizontal surface at $z = t$ in interval $x \in [a, d]$, the following equation can be obtained:

$$j \sum_{n=-\infty}^{\infty} \frac{k_{z,II}}{k_{z,I}^{(n)}} |T_n|^2 \tan\left(k_{z,I}^{(n)} t\right) (B^+ - B^-) = (B^+ + B^-) \tag{15}$$

with

$$|T_n|^2 = \left| \sqrt{\frac{1}{ad}} \int_0^a e^{jk_{x,I}^{(n)} x} dx \right|^2 = \frac{a}{d} \left| \mathrm{sinc}\left(\frac{k_{x,I}^{(n)}}{2} a\right) \right|^2 \tag{16}$$

To solve for B^+ and B^-, another equation is needed. Such equation can be obtained when we consider another boundary condition, which is that the tangential *E*-field must vanish at the bottom of the groove:

$$B^+ e^{jk_{z,II}h} - B^- e^{-jk_{z,II}h} = 0 \tag{17}$$

By combining (15) and (17), a matrix equation is obtained for variables B^+ and B^-. In this manner, the problem is formulated into an eigenvalue equation problem. In order for the equation to have non-trivial solutions, we need to force the determinant of the matrix to be 0. As a result, the dispersion relationship for the anti-symmetric modes of the DC-SSPP structure could be finally obtained as:

$$1 - \sum_{n=-\infty}^{\infty} \frac{k_{z,II}}{k_{z,I}^{(n)}} |T_n|^2 \tan\left(k_{z,I}^{(n)} t\right) \tan\left(k_{z,II} h\right) = 0 \tag{18}$$

Other than the anti-symmetric modes, the doubly corrugated SSPP structure can also support symmetric modes, as expressed by following mode expressions:

In Region I:

$$\begin{bmatrix} H_x^I \\ H_y^I \\ H_z^I \end{bmatrix} = \sum_{n=-\infty}^{\infty} \rho_n e^{jk_{x,I}^{(n)}x} \begin{bmatrix} j\dfrac{k_y k_{x,I}^{(n)}}{\nu_y^2}\cos(k_y y)\cos\left(k_{z,I}^{(n)}z\right) \\ \sin(k_y y)\cos\left(k_{z,I}^{(n)}z\right) \\ -\dfrac{k_y k_{z,I}^{(n)}}{\nu_y^2}\cos(k_y y)\sin\left(k_{z,I}^{(n)}z\right) \end{bmatrix} \tag{19}$$

$$\begin{bmatrix} E_x^I \\ E_y^I \\ E_z^I \end{bmatrix} = \frac{1}{\omega\epsilon}\frac{k_0^2}{\nu_y^2}\sum_{n=-\infty}^{\infty} \rho_n e^{jk_{x,I}^{(n)}x}\sin(k_y y) \begin{bmatrix} jk_{z,I}^{(n)}\sin\left(k_{z,I}^{(n)}z\right) \\ 0 \\ -k_{x,I}^{(n)}\cos\left(k_{z,I}^{(n)}z\right) \end{bmatrix} \tag{20}$$

In Region II:

$$\begin{bmatrix} H_x^{II} \\ H_y^{II} \\ H_z^{II} \end{bmatrix} = \begin{bmatrix} -\dfrac{k_y k_{x,II}}{\nu_y^2}\left(A^+e^{jk_{z,II}z} + A^-e^{-jk_{z,II}z}\right)\cos(k_y y)\sin(k_{x,II}x) \\ \left(A^+e^{jk_{z,II}z} + A^-e^{-jk_{z,II}z}\right)\sin(k_y y)\cos(k_{x,II}x) \\ j\dfrac{k_y k_{z,II}}{\nu_y^2}\left(A^+e^{jk_{z,II}z} - A^-e^{-jk_{z,II}z}\right)\cos(k_y y)\cos(k_{x,II}x) \end{bmatrix} \tag{21}$$

$$\begin{bmatrix} E_x^{II} \\ E_y^{II} \\ E_z^{II} \end{bmatrix} = \frac{1}{\omega\epsilon}\frac{k_0^2}{\nu_y^2}\sin(k_y y) \begin{bmatrix} k_{z,II}\left(A^+e^{jk_{z,II}z} - A^-e^{-jk_{z,II}z}\right)\cos(k_{x,II}x) \\ 0 \\ -jk_{x,II}\left(A^+e^{jk_{z,II}z} + A^-e^{-jk_{z,II}z}\right)\sin(k_{x,II}x) \end{bmatrix} \tag{22}$$

Following the same procedure as in the case of anti-symmetric modes, the dispersion relationship of the symmetric modes can be obtained by solving the following equation:

$$1 + \sum_{n=-\infty}^{\infty} \frac{k_{z,II}}{k_{z,I}^{(n)}}\frac{|T_n|^2}{\tan\left(k_{z,I}^{(n)}t\right)}\tan(k_{z,II}h) = 0 \tag{23}$$

While (18) represents a mode that uniquely exists in DC-SSPP architecture, the solutions of (23) feature dispersion curves that closely resemble those of other corrugated structures. For example, the dispersion relationships of single-sided SSPP structure are very similar in general shape [31, 42, 45]. However, here the inclusion of the dimension t indicates the influence of the waveguide thickness. This term, which represents the effect of the cross-coupling between the opposing grooves, does not exist in any analysis with only one-sided corrugations.

As an example, a doubly-corrugated SSPP THz structure with dimensions d = 100 μm, a = 10 μm, h = 80 μm, t = 33.33 μm, and W = 300 μm is considered in our calculation. For meanings of different notations, please refer to Figure 1. We use MATLAB as the software environment for

our entire analytical calculation [48]. The dispersion curves of the 1st and 2nd symmetric mode, as well as the 1st anti-symmetric mode of the structure, are shown in Figure 2. Due to the non-zero width of the structure in the y-direction, a cut-off frequency of 0.5 THz is presented. One must note that such cut-off wavelength should not be used as a benchmark in the description of sub-wavelength transmission, since in the THz domain the conventional index-guiding mechanism of a waveguide does not apply.

Figure 2(a) shows our calculation result, while in Figure 2(b) simulation result obtained by CST simulation software are included for comparison [49]. As can be observed, the two sets of dispersion curves from both approaches coincide with each other very well.

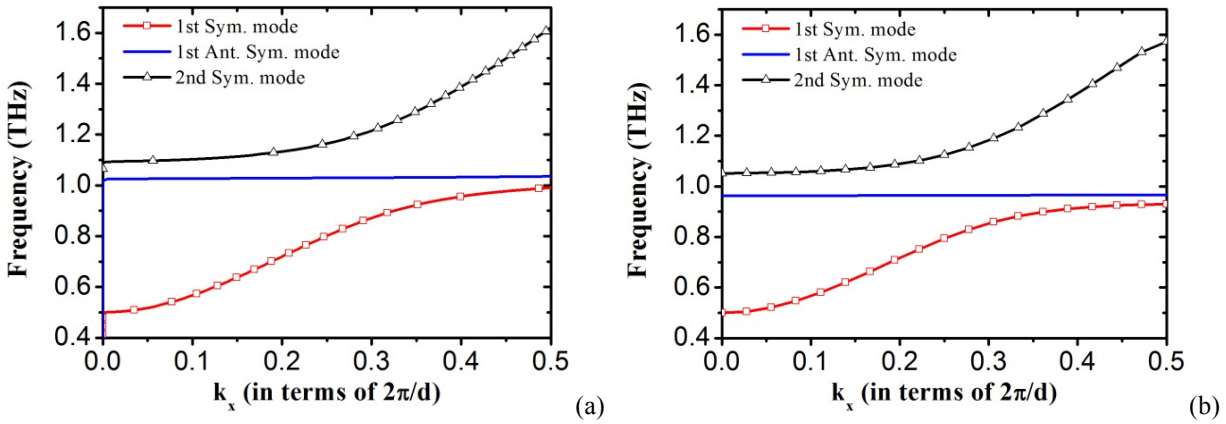

Figure 2: Dispersion relationship of the DC-SSPP structure using the stated dimensions (a) as calculated using our analytical model, and (b) as obtained using CST software package.

In Figure 2(a), the dispersion curve of the 1st symmetric mode resembles closely the shape of the surface plasmon mode on a smooth metal-dielectric interface. It is an SSPP mode, and its resonance frequency is by principle determined by the dimensions of the periodic structure. By examining (18) and (23), the plasmonic resonance frequency of the fundamental mode can be estimated to the first order by the following expression:

$$f_{pl} = \sqrt{\left(\frac{c_0}{4nh}\right)^2 + f_y^2}\,, f_y = \frac{c_0}{2nW} \tag{24}$$

In (24), f_y stands for the cut-off frequency due to the non-zero y-dimension of the structure, n is the refractive index of the dielectric material ($n = 1$ with air filling in this case), and c_0 is the speed of light in vacuum. For the DC-SSPP structure under investigation, f_{pl} is calculated to be

1.06 THz. In our analytical model, the same resonance frequency at 1.025 THz can be observed in Figure 2(a), which is a close agreement with the estimation. This resonance frequency corresponds to a wavelength of $\lambda = 293\mu m$, which is much larger than the height of the waveguide ($2t = 66.7\mu m$). Therefore this mode represents a sub-wavelength resonance of the structure.

From Figure 2(a) a slow-light mode can also be observed, which is the 1st anti-symmetric mode (as represented by the blue line). This mode has a nearly flat dispersion curve, which suggests the existence of a pass-band very sharp and narrow. On the downside, this flatness also indicates a mode group velocity of almost 0, which will severely lower the energy coupling efficiency into and out of the structure.

To better illustrate the effect of cross-coupling between opposing grooves in the DC-SSPP architecture, the dispersion relations with different *t* for the same structure are plotted in Figure 3. In accordance with the analytical formulations, it is easy to observe the great influence of the distance between opposing grooves to the dispersion relations. With decreasing *t*, the bandgap between the 1st and 2nd symmetric mode increases dramatically. Such effect is missing in the single-sided grooved structures. It can be utilized to modify the designer bandgap for different applications. The anti-symmetric modes, in this case, are super-flat as is suggested by Figure 2. They mostly coincide with each other for different *t* values, therefore are not included in the plot.

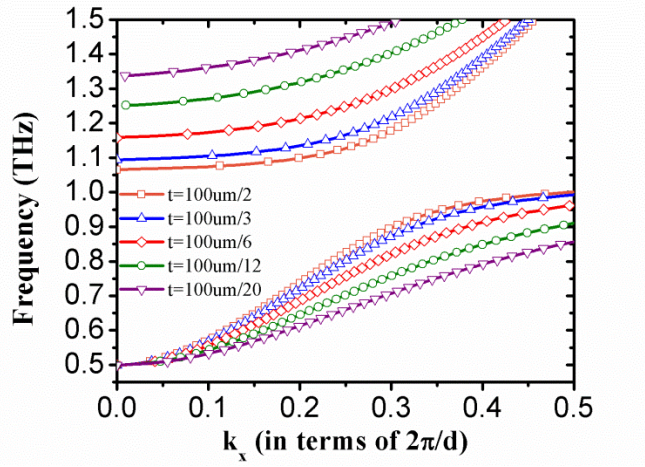

Figure 3: Dispersion relation of the DC-SSPP structure with different *t*, namely the height of the waveguide (smooth part). Only symmetric modes are depicted here as the flat anti-symmetric modes mostly coincide with each other.

Moreover, our simulation is able to draw the dispersion map of all the higher order modes of the DC-SSPP structure, which is included here in Figure 4. It shows the dispersion curves of the first 5 modes of the same DC-SSPP structure from which the complex nature of those modes can be clearly seen. In general, those higher order SSPP modes can be categorized into two kinds. One kind consists of modes that are separated by the band-gaps, as a natural solution to (18) and (23). They are also the same higher order modes as we referred to in all previous figures and analysis. The other kind, on the other hand, consists of modes that are merely pushed up from lower orders as higher *y*-direction orders are used in the calculation (represented by larger m values in the expression $k_y = \frac{m\pi}{W}, m = 1,2,\ldots$). Therefore they are almost clones in shape to the lower order modes and can be easily recognized. Since the mode solutions with different *y*-dimension orders are themselves independent, modes from different *y*-orders can intersect with each other without affect the accuracy of our calculations.

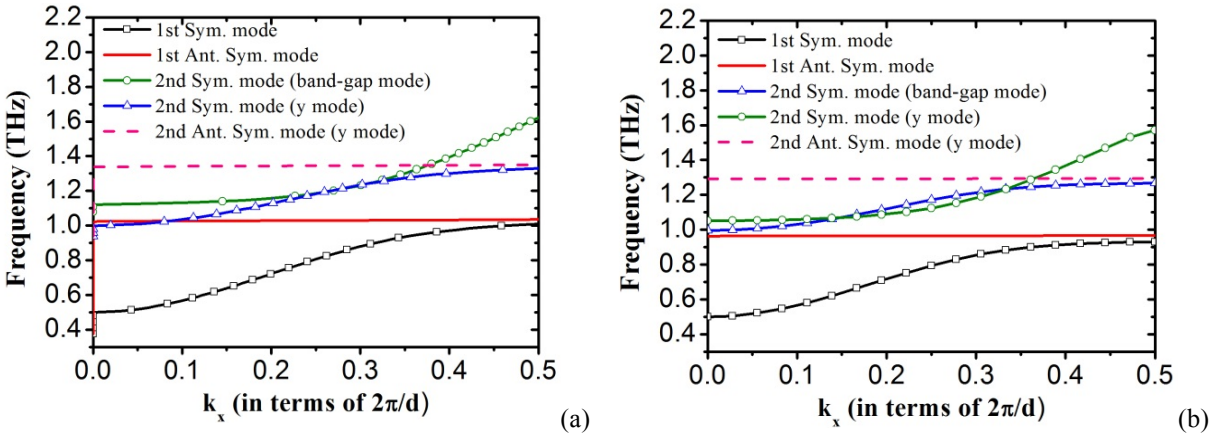

Figure 4 Dispersion map of the first 5 modes of the DC-SSPP structure using the stated dimensions, (a) as simulated using our analytical model, and (b) as obtained using CST software package.

From Figure 4, it is straightforward to observe that single-mode operation can be achieved for frequencies below 1 THz. As the spectral response will be significantly different when multiple modes can propagate simultaneously in the waveguide, the ability to operate in single mode is critical for many, if not all applications of the DC-SSPP structure. With different geometric dimensions, the frequency range in which only one SSPP mode is supported can be adjusted accordingly. Therefore, one can choose to include an almost arbitrary number of pass bands in the single mode zone depending on the needs of the applications. The ability to design the single

mode operation zone is another advantage of such architecture over the conventional, non-modified waveguiding structures.

2.2 Transmission properties

As an important part of the complete characterization of the doubly-corrugated SSPP structure, the transmission properties contain the information of the frequency-dependent reflectance and transmittance (conventionally denoted as *R* and *T*) of the SSPP device. We use scattering matrix method to study such properties.

We first divide each of the single "cells" (meaning one periodic unit which repeats itself to form the whole structure) in the *x*-direction into four sections, as shown in Figure 5. To be explicit, the four sections are: 1. the abrupt change from the narrow part to the wide part of the structure which can be understood as a step junction; 2. the straight wide part (containing the groove), which is an analogy to a smooth transmission line; 3. the abrupt change from the wide part back to the narrow part of the structure, which is another step junction; and 4. the smooth narrow part, which again, is an analogy to a homogeneous transmission line.

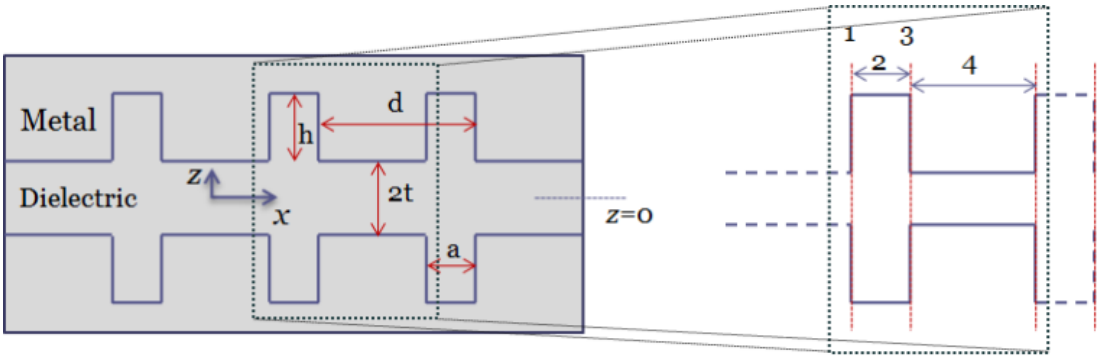

Figure 5 The break-down of a single "cell" of the doubly corrugated SSPP structure into four sections

The treatment of periodic microwave structures using scattering/transmission matrices (S/T-matrices) is studied in detail by Naini *et al* [50]. Here a similar approach is used to describe the S-matrices of each section of the single cell as delineated above. While the S/T-matrices for section 2 and 4 are rather straightforward, our main effort is to obtain the same matrices regarding the discontinuities, namely section 1 and 3. Mode matching is the key in describing the scattering event at those abrupt structural changes. If we define *H* as the mode matching efficiency across the boundary, it can be expressed as:

$$H = \frac{\int_{-(t+h)}^{t+h} \langle h_2 | h_1 \rangle dz}{\int_{-(t+h)}^{t+h} \langle h_1 | h_1 \rangle dz} \tag{25}$$

In the above expressions, h_1 and h_2 denote the transverse magnetic fields on the two sides of the boundary and $\langle \quad \rangle$ denotes an inner product. Unlike the classical waveguide modes used in [50], in our case the mode profile inside the structure is described by SSPP modes as solved in the previous section of 2.1. Accordingly, the mode coupling efficiency needs significant modifications. In our case, the mode distributions are obtained by combining equations (13), (14) and (17) for anti-symmetric modes, and their equivalents for symmetric modes. As an example, if we consider the case for symmetric modes, and assume that only the lowest order Floquet mode is significant, which is usually the case since higher order modes are in most circumstances evanescent waves, we can have:

In Region I:

$$H_y^I = -2\sqrt{\frac{a}{d}} T_0^* \frac{k_{z,II}}{k_{z,I}^{(0)}} \frac{A\sin\left(k_{z,II}h\right)}{\sin\left(k_{z,I}^{(0)}t\right)} \cos\left(k_{z,I}^{(0)}z\right) e^{jk_{x,I}^{(0)}x} \tag{26}$$

and in Region II:

$$H_y^{II} = 2A\cos\left(k_{z,II}[z-(t+h)]\right) \tag{27}$$

In the above expressions, A is the amplitude constant, and * denotes the complex conjugate.

Take section 1 as an example. Using (25), H in this case can be calculated as:

$$H = \frac{\frac{a}{d}|T_0|^2 \left(\frac{2k_{z,II}}{k_{z,I}^{(0)}} \frac{\sin\left(k_{z,II}h\right)}{\sin\left(k_{z,I}^{(0)}t\right)}\right)^2 \left(t + \frac{1}{2k_{z,I}^{(0)}} \sin\left(2k_{z,I}^{(0)}t\right)\right)}{4h + \frac{2}{k_{z,II}} \sin\left(2k_{z,II}h\right) + \frac{a}{d}|T_0|^2 \left(\frac{2k_{z,II}}{k_{z,I}^{(0)}} \frac{\sin\left(k_{z,II}h\right)}{\sin\left(k_{z,I}^{(0)}t\right)}\right)^2 \left(t + \frac{1}{2k_{z,I}^{(0)}} \sin\left(2k_{z,I}^{(0)}t\right)\right)} \tag{28}$$

In order to obtain the four elements of the scattering matrix, it is helpful to pre-define a number of variables and to use them directly in the formulation. First of all, the characteristic admittances of the waveguide on both sides of the interface can be calculated as:

$$\begin{cases} Y_{01} = A\dfrac{jk_0}{k_{x,I}^{(0)}}\sqrt{\dfrac{\varepsilon_0}{\mu_0}} \\ Y_{02} = \dfrac{jk_0}{k_{x,I}^{(0)}}\sqrt{\dfrac{\varepsilon_0}{\mu_0}} \end{cases} \tag{29}$$

We then define the complex power of the *E-M* field on both sides of the discontinuity along with their complex conjugates to be:

$$\begin{cases} P_1 = Y_{01}^* \displaystyle\int_{-(t+h)}^{t+h} \langle h_1|h_1\rangle dz\,, Q_1 = P_1^* \\ P_2 = Y_{02}^* \displaystyle\int_{-(t+h)}^{t+h} \langle h_2|h_2\rangle dz\,, Q_2 = P_2^* \end{cases} \tag{30}$$

Finally, we define T_2 to represent the equivalent voltage coupling efficiency:

$$T_2 = \sqrt{2\int_{-(t+h)}^{t+h} \langle h_2|h_1\rangle dz} \tag{31}$$

Using these variables, the effective admittance of mode coupling can be calculated as:

$$Y_2 = 2(T_2)^{-1*} H^* P_1^* H (T_2)^{-1} \tag{32}$$

The S-matrix of section 1 can then be obtained using the following formulas:

$$\begin{cases} S_{22} = T_2^{-1}(Y_{02} + Y_2)^{-1}(Y_{02} - Y_2)T_2 \\ S_{12} = H(S_{22} + I) \\ S_{21} = Q_2^{-1} S_{12}^T Q_1 \\ S_{11} = HS_{21} - I \end{cases} \tag{33}$$

In order to combine S-matrices of 4 sections together, as well as to obtain the S-matrix of the whole structure from that of the single cell, there are in general two approaches. One is to transform the S-matrices into transmission or transfer matrices (T-matrices), which can be simply multiplied together to get the overall T-matrix (and henceforth the S-matrix of the whole structure). This approach is conceptually straightforward; however it could introduce significant numerical errors to the end result when there are evanescent wave terms in the unit T-matrices.

An alternative approach is to use the S-matrices themselves in the entire calculation. Unlike the T-matrices, since mathematically the S-matrices are not directly stackable, there is no closed-form solution to the end result. Instead, an iterative algorithm is needed to solve the problem [51,

52]. Suppose we have an n-layer structure. The S-matrix of the previous p layers can be obtained from the S-matrix of the previous $(p-1)$ layers and that of the p^{th} layer, in the form of:

$$\begin{cases} S_{11}^{(p)} = s_{12}^{(p)} S_{11}^{(p-1)} \left[1 - s_{22}^{(p)} S_{11}^{(p-1)}\right]^{-1} s_{21}^{(p)} + s_{11}^{(p)} \\ S_{12}^{(p)} = s_{12}^{(p)} \left[1 - S_{11}^{(p-1)} s_{22}^{(p)}\right]^{-1} S_{12}^{(p-1)} \\ S_{21}^{(p)} = S_{21}^{(p-1)} \left[1 - s_{22}^{(p)} S_{11}^{(p-1)}\right]^{-1} s_{21}^{(p)} \\ S_{22}^{(p)} = S_{21}^{(p-1)} s_{22}^{(p)} \left[1 - S_{11}^{(p-1)} s_{22}^{(p)}\right]^{-1} S_{12}^{(p-1)} + S_{22}^{(p-1)} \end{cases} \tag{34}$$

In the above formulations, $S_{ij}^{(m)}$ is the S-matrix element of the previous m layers, and $s_{ij}^{(m)}$ is the S-matrix element of the m^{th} layer alone. The four expressions in (34) therefore present a way to iteratively obtain the S-matrices of arbitrary number of layers. Please note that here, one single layer consists of the layer itself and the interface it has with the adjacent layer directly after it. In this sense it is a combination of section 1 and 2 (or 3 and 4) in our circumstance as shown in Figure 5. Such method is proved to be effective in terms of eliminating the numerical instabilities as stated above.

For the same DC-SSPP structure that we studied in the dispersion relation calculations, the S-parameters for the symmetric mode as obtained using our analytical model are presented in Figure 6(a). The structure under consideration has 5 sets of grooves. The curve can be divided in general into two parts, namely the pass-band on the left half and the stop-band on the right half of the graph. The transition point corresponds to the SSPP resonance frequency above the 1st symmetric mode. Within the pass band, Fabry-Perot effect caused by multiple reflections from different groove edges gives rise to the multiple ripple features that can be observed on both S_{21} and S_{22} curves. For comparison, the same S-parameter curves are obtained using CST simulation packages and the result is included here in Figure 6(b). As we can see, the two curves resemble each other reasonably well.

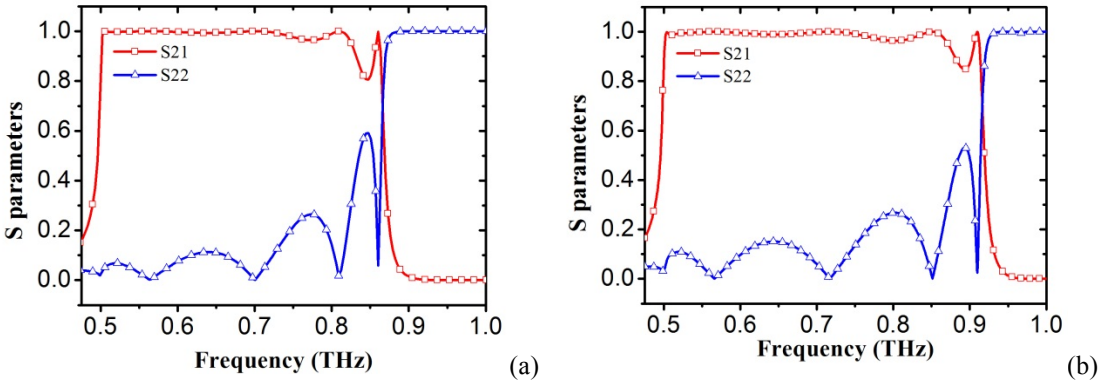

(a) (b)

Figure 6 S-parameters of the DC-SSPP structure using the stated dimensions, (a) as calculated using our analytical model, (b) as obtained using CST software package

In this structure, discrete transmission bands are observed in sub-wavelength frequencies. One can also observe from (24) that the width W of the waveguide determines the cut-off frequency of the DC-SSPP structure by affecting f_y. When W increases, the cut-off wavelength f_y decreases and so will the SSPP resonance frequency, resulting in even larger passable wavelength for the same height of the waveguide.

The existence of sub-wavelength transmission band and sharp transmission peaks under certain device designs enable us to employ the DC-SSPP structure in various applications such as frequency filters and active switches. Such property is a unique feature of the DC-SSPP structure when compared with unmodified, smooth metal-dielectric THz waveguides.

2.3 Limitations and discussion

From the simulation results demonstrated in the previous two sections, it is fair to conclude that our calculation of both dispersion relationship and S-parameters show a very close match to the result obtained from elaborate simulation software packages. Nonetheless, there are visible discrepancies in both the result for dispersion curves and that of S-parameters between the two approaches. For example, when we consider the frequency where the first anti-symmetric mode starts for the DC-SSPP structure we studied in the previous sections, our result shows 1.025 THz while the CST simulation suggests 0.963 THz, which demonstrates a difference of 6%.

We conclude such discrepancy to be caused largely by the fact that edge effect is not included in our analysis of the structure. In real situations, *E-M* field inside the grooves (namely in Region II in our convention) and outside them (in Region I) are coupled with each other near the

boundaries. In other words, the field lines are not strictly horizontal or perpendicular to the boundary when they are crossing it; instead, they are bent to ensure a smooth transition between mode profiles in two different regions. This physics phenomenon is called the *edge effect* since they tend to happen at the edge of transitions. It usually becomes more significant when the wavelength of the *E-M* field becomes smaller, especially when it is comparable with the periodic structural dimensions.

For the DC-SSPP structure under investigation, the SSPP resonance frequency at 1.025 THz corresponds to a wavelength of $\lambda = 293$ μm. Although this wavelength is larger than the longitudinal dimension of the structure (d = 100 μm), the magnitude is still somewhat comparable. In this case, the edge effect can introduce small yet visible errors into our analysis, as the division of mode profiles strictly into two separate regions is not an accurate description of the mode distribution anymore.

The influence is even more significant when the frequency is near the plasmonic resonance frequency, as at resonance most of the energy is localized inside the groove region and the bending of *E-M* field is more emphasized. Figure 7 illustrates the ratio of energy stored inside the groove as compared with total energy in the structure as a function of frequency. A maximum of the curve can be clearly seen when the frequency is near resonance.

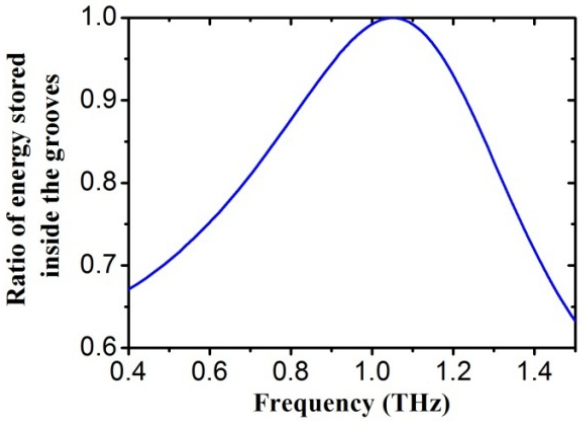

Figure 7 The percentage of energy stored in the groove regions as compared with the total *E-M* field energy, plotted against frequencies.

On contrary, if the resonance frequency of the structure is much larger than its periodic dimensions, edge effect will become negligible and the accuracy of our calculation will be improved. As an example, we simulated the structure with h = 200 μm, and with all other

dimensions staying the same. In this case, the SSPP resonance frequency of the structure as calculated by (24) has become 0.625 THz, which corresponds to a wavelength $\lambda = 480\mu m$. In Figure 8 the dispersion relationship of the first 5 modes of such structure is shown, along with the results from the CST simulations. As can be seen, here the results from both approaches are almost identical to each other. For example, the frequency where the 1st anti-symmetric mode resides is at 0.620 THz in our simulation, while the same frequency point in the CST result is located at 0.613 THz (both in close agreement with our estimation using (24)), indicating a diminished error down to 1.1%.

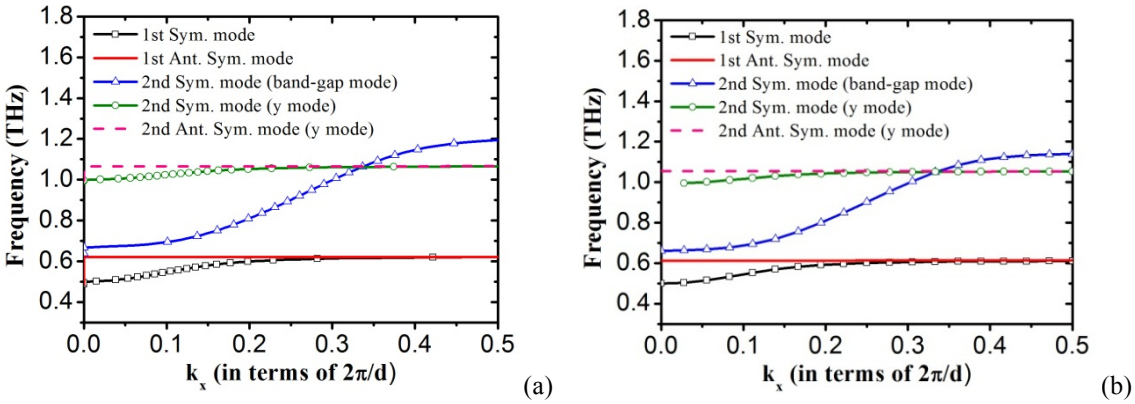

Figure 8 Dispersion map of the first 5 modes of the DC-SSPP structure with the same dimensions except for h = 200 μm, (a) as calculated using our analytical model, and (b) as obtained using CST software package.

CHAPTER III THz DNA Bio-Sensing Employing DC-SSPP Architectures

3.1 Background

As technology progresses, we begin to face not less, but more challenges in detecting and reacting to the potential threat and hazardous materials in real life scenarios. To name just a few, this may include the sudden breakout of epidemic diseases, the menace of potential bio-weapon attacks in warfare, the constant threat of unknown 'white powder' concealed in envelopes, the attempt to bring hazardous materials onboard mass transportations, etc. In these cases, effective methods to quickly detect, identify and neutralize the threats are the objectives pursued by many. The sensing of bio-related events often calls for the identification of certain bio-materials or their interactions. Substances of interest consist of a wide range of molecules including enzymes, DNA, bio-hazard chemicals and a variety of organic compounds. Examples of bio-molecular interactions include antigen-antibody binding, DNA/RNA binding, DNA hybridization and denaturation, cell-cell specific affinity binding and other binding assays [53, 54]. Such detections must rely on the mechanical, chemical, electrical or optical properties of the sample under inspection. For decades, bio-sensing systems of various designs have been developed with the aim of detecting and differentiating bio-molecules and substances with high sensitivity and selectivity.

In any bio-sensing strategy, a ligand is chosen to interact specifically with the analyte of interest in order to generate a signal to be recorded and interpreted. To label and detect the signal, the most popular approach is to tag the bio-materials of interest with fluorescent agents [55, 56, 57]. Despite its wide use, fluorescence-based bio-sensing methods suffer from the disadvantages of low sensitivity (weak fluorescent signal), interference with the target of interest, and fluorophore degradation over time [54, 58, 59, 60, 61]. In addition, the involvement of a fluorescent tag also mandates extra preparatory steps which are usually time-consuming. The ultimate goal of any biosensing scheme is to obtain high responsivity and selectivity with

minimal perturbation to the analyte. Added to these conditions are other goals of convenience such as ease of sample preparation, portability, low-cost and possibly reusability. In light of these requirements, THz biosensing has been put forward as a non-invasive, marker-free alternative to the fluorescent tagging method.

A wide range of bio-molecules, as well as their interactions, possess spectral features, due to their vibrational, rotational or translational resonance modes that largely reside in the THz frequency range. Macromolecules such as proteins and DNA molecules all have numerous vibrational modes in THz frequencies, and such spectral features are shifted or altered when chemical or conformational changes to the molecules take place [62, 63, 64, 65, 66, 67]. In this sense, by detecting a spectral change using a probing THz beam, the intensity of bio-molecular interactions can be quantitatively determined.

This THz bio-sensing approach has several advantages when compared with fluorescent-tagging methods. First and foremost, it does not require the attachment of extra agents to the analyte, therefore eliminating possible interference and excessive background signal. Secondly, in the traditional tag-based method, the variability from one assay to another cannot be effectively accounted for unless a universal fluorophore attachment exists. However, flexible analysis can be achieved with ease using THz sensing with tunable emitters and detectors. Thirdly, the speed of THz sensing is potentially greater since the tagging step in the sample preparation process can be eliminated. In addition, the energy levels at THz frequencies are low (4meV at 1 THz), enabling probing of biological samples with no concerns of tissue damage. These advantages are further assisted by the fact that THz radiation can easily penetrate paper, plastic, cloth and even wood, reaching samples buried deep within. The positive phenomenology of non-invasive THz sensing has triggered extensive research activities in this area. Bio-molecules including chromophore retinals, various types of proteins, DNA, RNA, antigen-antibody pairs have all been used for the demonstration of THz biosensing capabilities [21, 22, 23, 68, 69, 70, 71, 72, 73, 74]. THz sensing has even been applied to detect and identify entire bacteria cells and spores [75, 76].

Among the variety of THz biosensing, DNA sensing is of great research interest due to its indispensable role in numerous applications including disease prevention, bio-hazard material identification, and gene sequencing. The key interactions of DNA molecules are the

denaturation and hybridization events, which signify the transition between single-stranded and double-stranded DNA pieces. These interactions dictate the way DNA molecules reproduce and the way they conjugate with different types of RNA molecules, which are known as the basis for any life to exist, function, regenerate and evolve. The strong pairing of single-stranded DNA only takes place between complementary base sequences. Therefore, if we mix the unknown sequences with single-stranded "probe" DNA molecules with known sequences, the similarity of the probe and the DNA piece under investigation will be determined by examining the density of binding events in the mixture [77].

Traditionally, the detection of the binding event is fulfilled by fluorescent tagging [58, 59, 60, 61]. In the context of THz biosensing, however, DNA molecules with different binding states are differentiated by detecting the change in their characteristic vibrational resonances and refractive indices. In some pioneering studies, THz time-domain spectroscopy (THz-TDS) was used to detect the spectral shift induced by the hybridization event. In 2000, M. Brucherseifer *et al*. first used THz-TDS and a free-space experimental setup to study the difference in refractive index for denatured and hybridized DNA molecules [21]. In their study, a refractive index change of $\Delta n \approx 0.1$ was observed for hybridized and denatured DNA almost regardless of the sample thickness and segment length. Various DNA samples and different laser systems were used in the experiment and the reproducibility of the result was successfully demonstrated. Brucherseifer's work has opened the gate for THz sensing of DNA molecules of different binding states, though large amounts of samples were needed in order to compensate for the method's relatively low sensitivity.

Subsequent works by Nagel *et al*. have used planar and ring resonators made of thin-film microstrip lines (TFML) as resonator cavities in order to increase the Q factor of the transmission spectrum, and DNA binding state detection with a *fmol* level of sample concentrations has been realized [78, 79, 80]. Although DNA biosensing with minute sample amounts was reported in these works, the spectral selectivity of the TFML resonators is far from satisfactory. Q factors of less than 100 were typical in the detector architectures as mentioned above, which plagued the repeatability of the result and hindered the further increase of the device sensitivity.

The real challenge of THz DNA sensing lies in the subtle change in the dielectric property when DNA molecules hybridize. The relative shift of the refractive index, defined as $\Delta n/n$, is typically in the order of merely a few percent. Faced with this challenge, sensing structures with localized field concentration and highly selective transmission spectrum must be introduced. In Chapter II, the spectral output of the DC-SSPP structure has been shown in (18), (23), and (24) to be a function of the geometric dimensions as well as the choice of materials. The concentrated field distribution in the groove region is also calculated and shown in Figure 7. As a result, this study on the DC-SSPP waveguide structure has quickly converged to the design of a variety of DNA biosensors.

In order to achieve sharp spectral selectivity, structural modifications are made to the simple SSPP waveguide. These modifications include the combination of two branches of DC-SSPP waveguide to form a Mach-Zehnder interferometer (MZI), as well as the addition of gap structures to create a local resonant cavity. In the MZI architecture, the extraction of phase information as a result of the coherent interference can boost the extinction ratio of the THz output between different DNA binding states. In the gapped structure, the additional coupling mechanism between the SSPP waveguide and the resonant cavity contributes to the enhanced Q factor of the selective transmission peak. These structural modifications have given rise to the designs of DNA biosensors with higher sensitivity and minimized sample amount required for successful detection.

3.2 Phase shift in DC-SSPP architecture: theoretical analysis

The same DC-SSPP waveguide is used as in Chapter II. The dispersion relation of this structure is given as:

$$1+\sum_{n=-\infty}^{\infty}\frac{k_{z,II}}{k_{z,I}^{(n)}}\frac{|T_n|^2}{\tan\left(k_{z,I}^{(n)}t\right)}\tan\left(k_{z,II}h\right)=0 \tag{35}$$

for the symmetric mode, and

$$1-\sum_{n=-\infty}^{\infty}\frac{k_{z,II}}{k_{z,I}^{(n)}}|T_n|^2\tan\left(k_{z,I}^{(n)}t\right)\tan\left(k_{z,II}h\right)=0 \tag{36}$$

for the anti-symmetric mode. The wavevectors as mentioned above are functions of refractive index *n* of the dielectric material. Therefore, when a modulation on *n* is introduced in some way, it is possible to modulate the wavevector, hence the phase accumulation of the THz wave traveling within the structure. As an example, the dispersion relationship of the DC-SSPP structure of dimensions d = 100 μm, a/d = 0.1, h/d = 0.8, t/d = 1/3, W = 300 μm as calculated from (35) using MATLAB is shown in Figure 9. The waveguide is filled with materials with refractive indices $n_0 = 1$, $n_1 = 1.05$ and $n_2 = 1.15$ respectively. In the figure the dispersion curve is seen to be significantly lowered when higher refractive index sample is loaded.

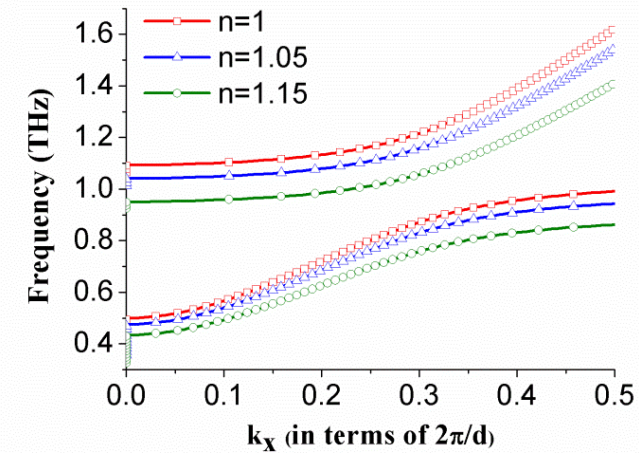

Figure 9 Dispersion relation of the single-armed DC-SSPP structure with three different refractive indices

A natural result of this modified dispersion relations is the difference in phase accumulations when the THz signals propagate through such DC-SSPP structures with different dielectric constant. In Figure 10 we show the phase difference of THz signals after it travels through 7 grooves of the DC-SSPP waveguide with three refractive indices ($n_0 = 1$, $n_1 = 1.05$ and $n_2 = 1.15$). The solid lines represent the result obtained from our mathematic model and the dashed lines show the simulation results obtained using HFSS software [81]. It is observed that the two curves are close to each other with frequencies far from the SSPP resonance. Near the band-gap region, despite the observable disparities, both curves show a sharp increase of the phase difference, as is predicted from Figure 9 with flattened dispersion curves.

The two curves have a diverging discrepancy near the band-gap, to which various reasons may apply. The main factor contributing to this difference is the *edge effect*, which signifies the distorted strong *E-M* field around the edges of the grooves near resonance. As is discussed in

Chapter II, under such circumstance the waveguide cannot be accurately described as the combination of the distinctive Region I and Region II, which can give rise to errors in the analytical calculation. For the same structure, in Chapter II we have observed a difference of ~ 0.07 THz in resonance frequency as obtained by the analytical model and CST simulation software. Such number agrees with the results we obtained here.

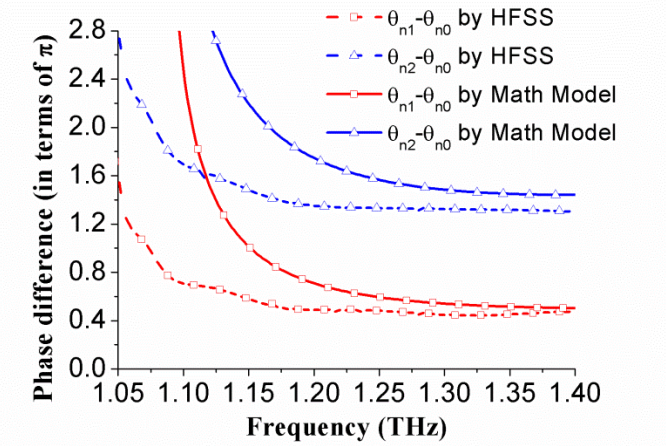

Figure 10 Difference in phase accumulation for THz signals as a function of frequency between three refractive indices ($\boldsymbol{n_0 = 1}$, $\boldsymbol{n_1 = 1.05}$ and $\boldsymbol{n_2 = 1.15}$), as obtained using both the analytical model and HFSS simulations

Another basic difference in the two approaches is the assumption of an infinite waveguide in our mathematic model, whereas in HFSS simulation we modeled the structure to have a finite length in the propagation direction. To study the effect of the latter, we simulated similar structures in HFSS with different numbers of periods up to 20 grooves. The results demonstrate close to a linear change of the signal phase delay and no significant alleviation of the discrepancy with the increase in the waveguide length, therefore ruled out its contribution to such disparities. We will hence consider the SSPP waveguide with as few as 7 grooves to be effectively periodic and will use it as the basic building block for our MZI structures.

As phase modulation by changing refractive index *n* is demonstrated, we can combine two arms of DC-SSPP waveguides to form a Mach-Zehnder interferometer (MZI). The THz signal from two arms of the MZI, when recombined after they propagate through different dielectric materials, will be either enhanced or reduced in magnitude as a result of coherent interference. The combined effect of the selectivity of single-armed DC-SSPP waveguide and that of the interferometer will result in a transmission curve with sharper features as well as better sensitivity to structural and material variations caused by external modulations.

3.3 DC-SSPP MZI architecture with material variation: finite-element simulation

In order to verify the idea, the DC-SSPP MZI structure as depicted in Figure 11 is simulated using finite-element method in the environment of Ansoft HFSS. Various dimensions are labeled in the figure, with *D* denoting the distance between the two waveguide arms. The first structure we simulate has the dimensions of $d = 100$ μm, $a/d = 0.1$, $h/d = 0.8$, $t/d = 1/3$, $W = 300$ μm, and $D = 250$ μm, and each arm consists of a DC-SSPP waveguide with 7 grooves. Similarly, as in the theoretical study, we use three refractive indices of $n_0 = 1$, $n_1 = 1.05$, and $n_2 = 1.15$. In fact, these refractive indices are the first-order approximation to represent air, denatured DNA and hybridized DNA, respectively, which are obtained from Brucherseifer's work under the assumption of no material loss [21]. With the samples filling up one of the arms and air filling up the rest of the structure, the transmission curves of the MZI are shown in Figure 12(a). For comparison, the transmission curves of the single arm DC-SSPP structure of the same dimensions are shown in Figure 12(b).

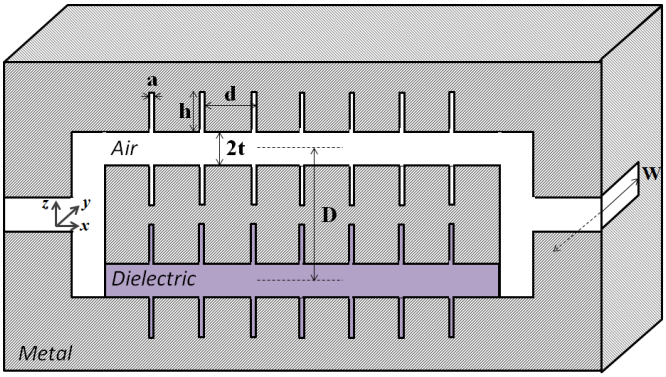

Figure 11 Cross-section of the DC-SSPP MZI structure with different geometric dimensions labeled. *W* is the width of the waveguide along the *y*-direction. The lower arm of the MZI structure (shaded in purple) designates the volume with dielectric loading

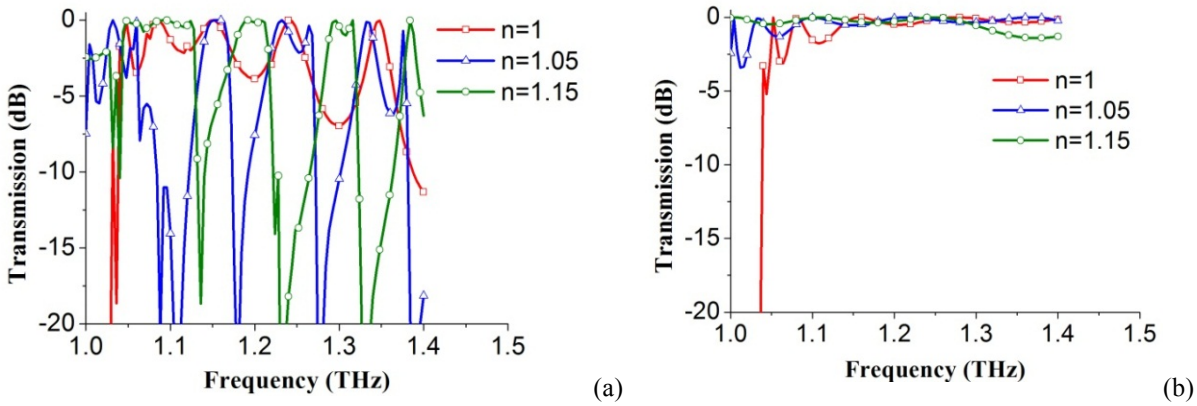

Figure 12 Transmission spectrum of (a) the DC-SSPP MZI structure and (b) the single-armed DC-SSPP structure. Three different refractive indices corresponding to air, denatured DNA, and hybridized DNA molecules are selected as the dielectric loading. For MZI structure such loading only applies to one of the arms as depicted in Figure 11

It is quite obvious that by combining the DC-SSPP waveguide into an MZI structure, the spectral features of the transmission curves are greatly enhanced. Above the first band-gap, single-armed waveguide barely shows any suppression of the transmitted signal beyond 5dB, while the distinction between the pass and the stop bands of the MZI structure is quite significant. The peaks and valleys of the transmission curves of the single-armed waveguide, and those of the MZI structure with $n_0 = 1$ (*i.e.* when both arms are filled with air) come from the Fabry-Perot etalon effect. While the F-P ripples are caused only by the periodicity of the grooves for the single-armed waveguide, for MZI structure they also come from multiple reflections from the walls that bound the interferometer.

In Figure 12(a) there are several frequencies where the MZI structure demonstrates distinct ON/OFF states when different dielectric materials are loaded. Some of those frequencies, along with the magnitude of transmission (T) and the phase difference as predicted in Figure 10 are listed in Table 2.

TABLE 2 TRANSMISSION (T) AND PHASE DIFFERENCE (Δϕ) AT SOME FREQUENCIES FOR THE DC-SSPP MZI STRUCTURE

Frequency	1.084THz	1.152THz	1.240THz	1.348THz
T when n=1	-0.03dB	-0.01dB	-0.03dB	-0.03dB
T when n=1.05	-10.25dB	0.00dB	-0.78dB	-3.79dB
Δϕ: n_1-n_0	0.824π	0.571π	0.486π	0.453π
T when n=1.15	-0.10dB	-6.20dB	-18.18dB	-15.11dB
Δϕ: n_2-n_0	1.873π	1.473π	1.334π	1.319π

By correlating the transmission with the phase difference, it is observed that significant suppression of the THz signal tends to happen when the phase difference between two arms of the interferometer is close to odd numbers of π. The transmission peaks and valleys do not correspond perfectly to integers of π in phase difference due to the fact that the transverse mode profile from two arms of the MZI structure is different when different materials are loaded, resulting in non-perfect enhancement or cancellation. The more complicated geometry of the interferometer also contributes to the disparity, when mode deflection of the additional walls and material interfaces cannot be neglected. Nonetheless, in Figure 10 if we compare the phase difference between two arms in the cases of $n_1 = 1.05$ and $n_2 = 1.15$, an almost constant difference of π is observed. This is consistent with the simulation results that the transmission peaks and valleys in the two cases are almost always inversed.

In Figure 13 we have included the *E*-field distributions on the cross-section of the structure at the frequency of f = 1.084THz. The constructive or destructive interference between the two arms in different cases can be clearly seen. It is noticed that for frequencies close to the SSPP resonance, the *E*-*M* field is greatly localized in the groove region of the structure. It is consistent with the theoretical analysis we did in Chapter II, where a strongly confined energy distribution of the THz wave is predicted near resonance. This property indicates the possibility of using less amount of dielectric loading to achieve the same selectivity of the structure, which is essential in achieving a lower detection limit of such biosensor design.

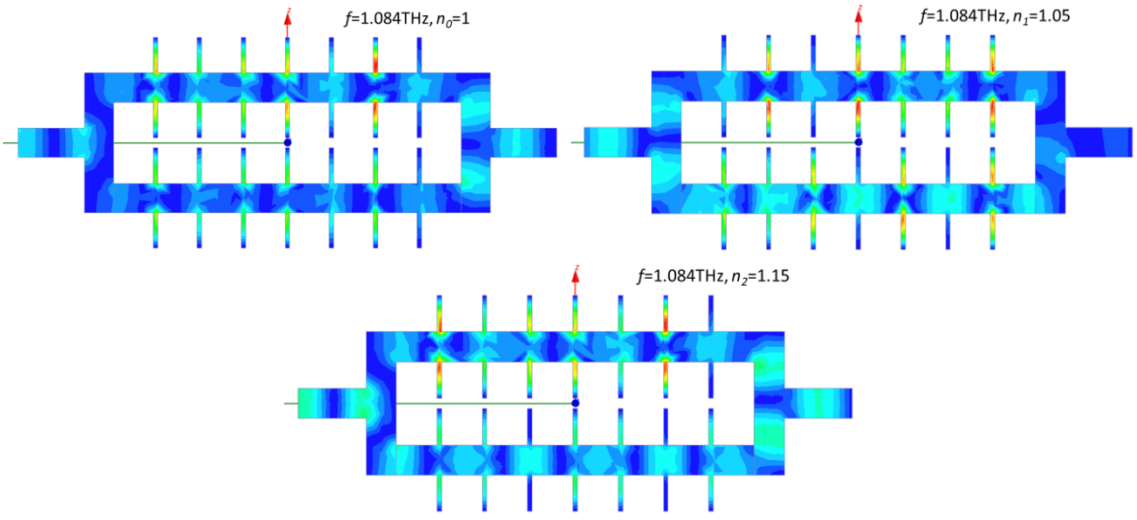

Figure 13 An example of *E*-field distribution in the DC-SSPP MZI structure at f = 1.084 THz for three different refractive indices (magnitude of the overall *E*-field is plotted). The different dielectric loadings and frequencies are labeled on the upper right corner of each plot

For that purpose we have simulated the MZI DC-SSPP structure with dimensions of d = 100 μm, a/d = 0.1, h/d = 0.8, t/d = 1/3, W = 300 μm, and D = 250 μm, this time with only the grooves plus a thin layer on each wall (with t'/d = 0.2) loaded with DNA samples (as shown in Figure 14). The simulation result is shown in Figure 15, and the magnitudes of transmission for the same set of frequencies are summed up in Table 3.

From both Figure 15 and Table 3, it is observed that when the frequency is close to resonance (f = 1.084 THz and 1.152 THz for example), the difference in ON/OFF state as induced by different sample loadings still exists and is consistent with the cases in Table 2. However, with frequencies far away from the resonance, the difference in phase accumulation with different sample loadings will not be significant due to the delocalization of the *E*-*M* field, resulting in the mostly coinciding transmission peaks. This way, it is demonstrated that the spectral sensitivity of the MZI DC-SSPP structure to the refractive index change is not harmed by the localized loading of the dielectric sample near the groove region, should the probe frequency be close to the SSPP resonance. When compared with the fully loaded case, the amount of sample needed in this case can be reduced by as much as 50%.

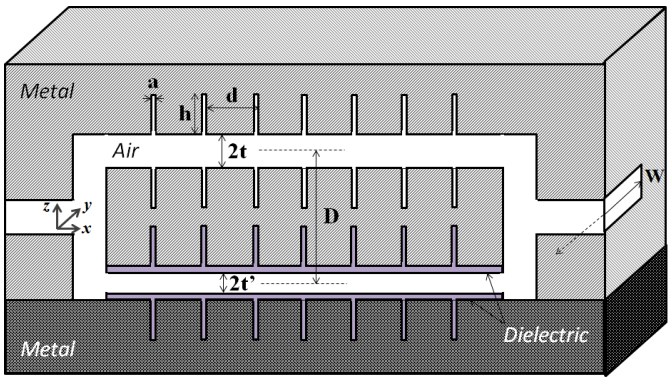

Figure 14 Cross-section of the DC-SSPP MZI structure with different geometric dimensions labeled. W is the width of the waveguide along the *y*-direction. Localized DNA loading is depicted as the purple-shaded area in the sketch. The dark and light gray coloring of the metal part is mere to show the modular design of the sensor

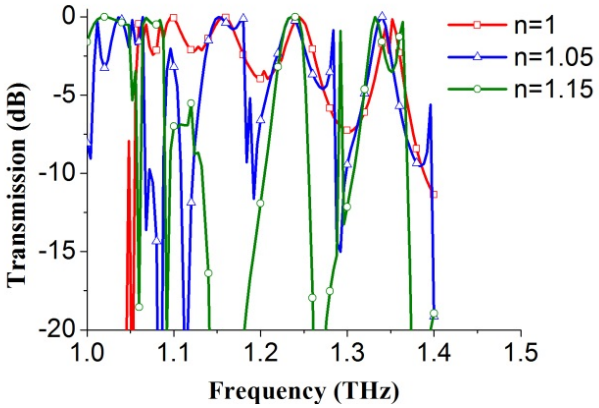

Figure 15 Transmission spectrum of the DC-SSPP MZI structure with localized sample loadings. Three different refractive indices corresponding to air, denatured DNA, and hybridized DNA molecules are selected as the dielectric loading. For MZI structure such loading only applies to one of the arms as depicted in Figure 14

TABLE 3 TRANSMISSION (T, IN DB) AT SOME FREQUENCIES FOR THE DC-SSPP MZI STRUCTURE, WITH LOCALIZED LOADING OF DNA SAMPLES NEAR THE GROOVE REGION

Frequency	1.084THz	1.152THz	1.240THz	1.348THz
T when *n*=1	-0.35dB	-0.19dB	-0.24dB	-2.30dB
T when *n*=1.05	-39.2dB	0.00dB	-0.24dB	-1.71dB
T when *n*=1.15	-0.21dB	-21.36dB	0.00dB	-3.38dB

The enhancement of the ON/OFF ratio is proven to be effective for differentiating small changes in the refractive index, in this case representing DNA molecules with distinct binding states. This phenomenon can be readily used in various real-world scenarios where a specific target DNA needs to be identified. One area of its potential application is the emerging technology of gene chips, where the DC-SSPP DNA sensing can provide quick detection of mutations on a specific gene section for the purpose of disease diagnosis. Another example is the screening of suspicious bio-hazard substances with the resemblance to harmless materials, where the real threat can be quickly identified from hoax attacks by a simple DNA matching test using the DC-SSPP bio-sensor.

In addition, the MZI DC-SSPP structure can in general produce sharper transmission peaks. To better illustrate this property, we conducted HFSS simulation on a second MZI DC-SSPP structure with dimensions of d = 100 μm, a/d = 0.1, h/d = 0.3, t/d = 1/3, W = 300 μm, and D = 250 μm. In Figure 16(a), we show the transmission spectrum of this structure in the presence of different refractive indices. From the curves, with denatured DNA ($n = 1.05$) filling up one arm, the Q factor for the first peak is estimated to be ~400 and that for the third peak to be ~1300.

Such peaks with high quality-factor are in direct contrast with the broad transmission peaks in other resonating structures such as TFML based planar and ring resonators.

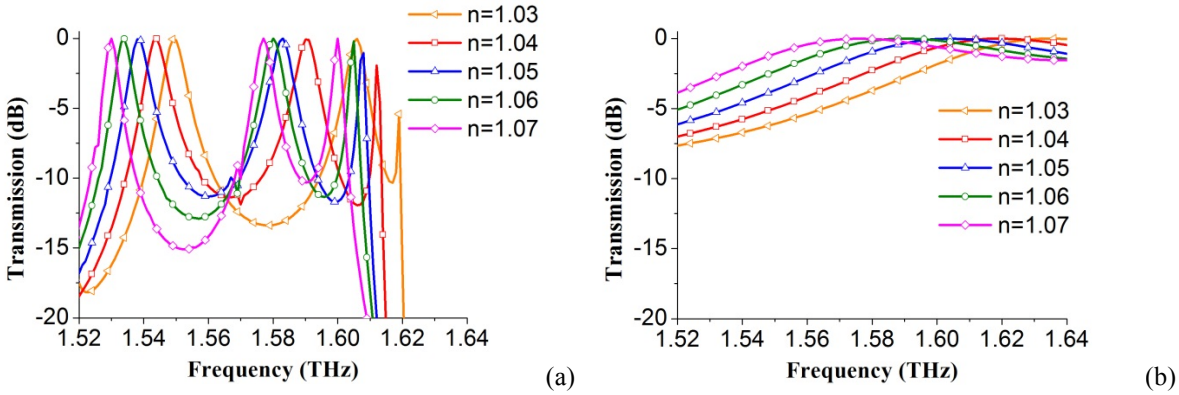

Figure 16 The transmission spectrum of (a) the DC-SSPP MZI structure and (b) the single-armed DC-SSPP structure. Five different refractive indices are selected as the dielectric loading, and for MZI structure such loading only applies to one of the arms as depicted in Figure 11

As observed from Figure 16(a), if we use the first peak of the transmission curves, a complete shift from ON to OFF state with a contrast of 15 dB at $f = 1.548$ THz can be induced by a refractive index change of 0.04. If the third peak is considered, such switching of state with an extinction ratio exceeding 20 dB can be achieved for a refractive index change of merely 0.01 (for example, at $f = 1.612$ THz with $n = 1.05$ and $n = 1.06$). The transmission curves for the single-armed waveguide with same dimensions is included in Figure 16(b) for comparison. Contrastingly, the flatness of those transmission spectra would prevent it from being much useful in the effective detection of such minute changes.

This enhanced Q factor of the transmission peaks is the desired property in a variety of applications, especially when a continuous, subtle change in the refractive index of the bio-sample needs to be detected. For example, in gene sequencing, the unknown DNA section can be mapped by mixing it simultaneously with known probes having different base sequences. In this case, a gradual density change from denatured DNA to hybridized DNA will be observed across the sensor array, giving rise to a continuous change in the mixture's refractive index. The DC-SSPP MZI sensing structure can then be used in this application to generate higher contrast for the detection of minute changes to the refractive index of the loaded DNA samples.

In reality, the sensor based on MZI SSPP structure can be constructed with two modules as shown by the different shading of the metal part in Figure 14. With the localized sample loading proved to be effective, the DNA preparation and immobilization process can be performed separately on the two modules of the sensor before they can be combined in a flip-chip manner and ready for tests. A similar idea of the modular design has been implemented by other groups and its effectiveness has been demonstrated [82]. Such design is the key for disposable sensor constructions and can greatly reduce the running cost of the technique.

3.4 DC-SSPP gapped structure with local resonant cavity

DC-SSPP structure is shown to have enhanced selectivity when the phase of the propagating THz signal can be extracted using an MZI setup. Besides this approach, structural modifications can also be made to the single-arm DC-SSPP waveguide for the purpose of achieving sharper spectral features. We introduce a gap structure within the DC-SSPP to form a local resonance. The additional cavity and its coupling with the rest of the waveguide result in much-enhanced responsivity to the changes in the sample's dielectric constant.

The gapped DC-SSPP structure is illustrated in Figure 17. The waveguide section between the gap structure acts as a resonant cavity, and the structure can also be referred as the waveguide-cavity-waveguide (WCW) structure. The overall transmission of the SSPP architecture is modified by the transmission property of this extra cavity, which is given by [83]:

$$T(\omega) = \frac{(\Gamma_c)^2}{(\omega - \omega_0)^2 + (\Gamma_c)^2} \tag{37}$$

$$R(\omega) = \frac{(\omega - \omega_0)^2}{(\omega - \omega_0)^2 + (\Gamma_c)^2} \tag{38}$$

In the above equations, T and R are the transmittance and reflectance of the cavity structure respectively. ω_0 is the resonant frequency of the cavity, and Γ_c is the waveguide-cavity coupling rate. As indicated by (37) and (38), when $\Gamma_c \ll |\omega - \omega_0|$, namely when the frequency is far away from the cavity resonance, the signal will be reflected by the cavity. When $\Gamma_c \gg |\omega - \omega_0|$, however, most of the energy will be transmitted through. This spectral selectivity, when combined with the transmission spectrum of the SSPP waveguide, can greatly enhance the responsivity of the structure to the refractive index changes. Compared with periodic SSPP

waveguide, it indicates the possibility of using reduced amount of samples without affecting the overall sensitivity of the structure.

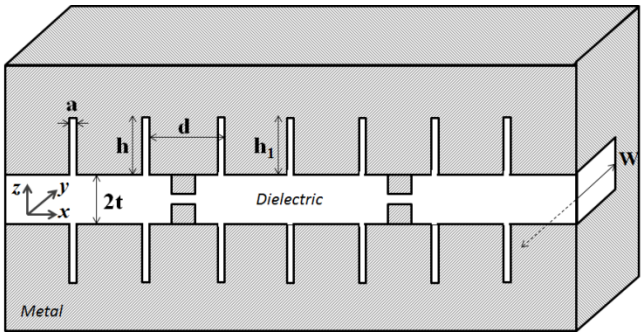

Figure 17 Cross-section of the modified SSPP structure with gap blocks

For the cavity structure, the quality factor of the transmission peak is inversely proportional to Γ_c as described by the following formula:

$$Q = \frac{\omega_0}{2\Gamma_c} \propto \frac{1}{(1-R)v_g} \tag{39}$$

From (39), it is indicated that higher quality factor is achieved with small group velocity v_g of the propagating wave and large reflectance R. Small v_g is obtained when the signal frequency is close to the band gap, as is observed from Figure 9. The reflectance, on the other hand, is determined by the geometries of the gap design. These two factors are the main design parameters for the gapped SSPP architecture.

Figure 18 shows the transmittance of the structure with different block dimensions. In the context of bio-sensing, refractive index n is the primary variable to be sensed. It is therefore chosen to be the x-axis of the plot in order to better illustrate the functionality of our structure. The probe signal frequency is chosen to be f = 1.08 THz so that it is close to the band gap. The dimensions of the structure are d = 100 μm, a/d = 0.1, h/d = 0.8, h/h_1 = 1.05, t/d = 0.3, and W = 300 μm. The transmission peak is located at n = 1, which mimics the case of air filling.

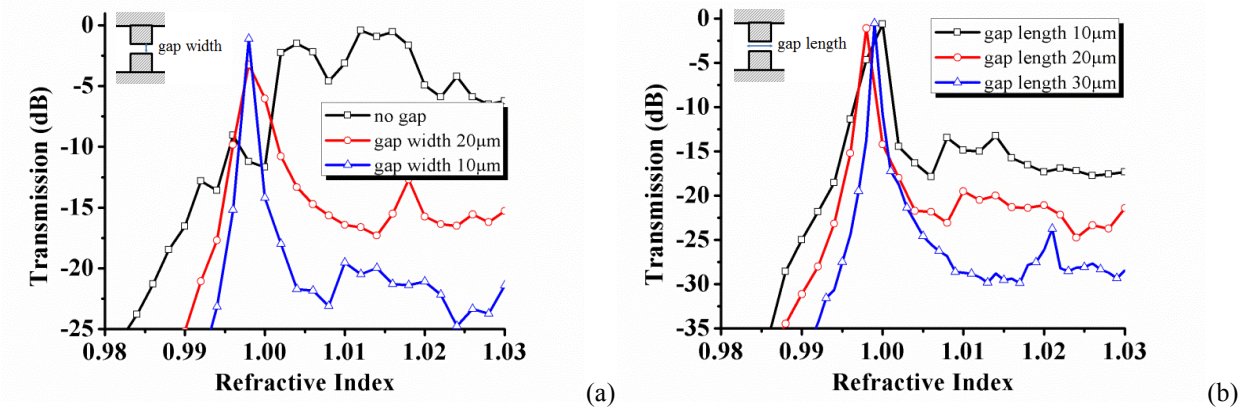

Figure 18 Transmission of gapped SSPP structure as a function of sample refractive index at f = 1.08 THz, a) with different gap widths, and b) with different gap lengths

The geometry of the block structure determines the width and length of the gap section. Figure 18(a) shows the evolution of the transmission curve with the change in gap width, which is defined as the distance between the blocking structures. With decreasing width, sharpening of the transmission peak as a function of sample refractive index is quite obvious. When no gap exists in the structure, the ON/OFF extinction ratio is merely 6 dB over a refractive index change of $\Delta n/n = 0.02$. With a gap width of 10 μm, the extinction ratio increased to over 20 dB for a refractive index change of merely $\Delta n/n = 0.006$, a huge enhancement compared with the other case. Similarly, the transmission curve with different lengths of the gap section is shown in Figure 18(b). The enhancement to the quality factor of the transmission peak is also observed as longer block structures are added to the waveguide. Narrower and longer gap structures are associated with a larger reflectance R, which explains this trend of increasing ON/OFF switching ratio in both comparisons.

The increased quality factor of the transmission peaks indicates the possibility of reducing the sample amount needed for successful detection. This is investigated by changing the sample-loading pattern as shown in Figure 19. SSPP architecture is known to have highly concentrated *E-M* field inside the groove region when it is close to resonance. As a result, sample deposition patterns that are localized inside the groove are used to compare with the fully loaded case. The four different patterns are denoted by A) sample fully loaded; B) sample in groove volume only; C) thin layers of 2 μm thickness on the groove wall, and D) thin layers of 1 μm thickness on the groove wall.

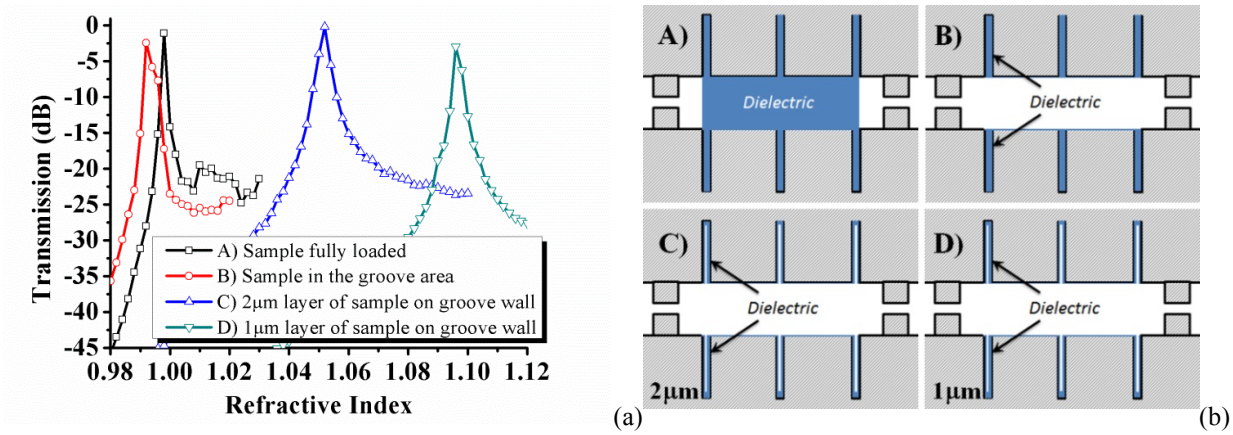

Figure 19 (a) Transmission of gapped SSPP structure as a function of sample refractive index with different sample deposition patterns. (b) Illustration of the sample deposition patterns

As shown in Figure 19, with the reduced amount of sample usage, the detected refractive index value is increased, while a minor deterioration in the quality factor of the peak is observed. The trend of increasing refractive index is explained by the larger contrast of n needed with smaller sample volumes. Broadened peak notwithstanding, in real bio-sensing scenarios the sample distribution in the form of case C) and D) is easier to realize, where thin layers of DNA molecules can be formed by immobilization to the metallic surface through atomic links. Moreover, the sample amount in case D) is two orders of magnitude smaller than that needed in case A), indicating a much-enhanced detection limit. From a practical standpoint, there are already mature procedures to deposit DNA in the form of thin layers or films. For example, the hexanethiol-modifier ($–(CH_2)_6–SH$) can be used to link DNA molecules to the gold surface via a stable S–Au linkage [80]. Furthermore, due to the large wavelength of the THz probe signal, the surface roughness of the DNA thin film will have a negligible effect on the detector output.

DNA sensing is therefore realized with localized sample deposition in the gapped SSPP architecture. This is illustrated in Figure 20, where the transmission peak, in the case of the sample load pattern D), is plotted as a function of probe THz frequency. High transmission can be achieved for a wide range of refractive index from $n = 1.15$ to $n = 0.97$, corresponding to the frequency change from $f = 1.073$ THz to $f = 1.095$ THz. It covers the n values for both denatured ($n_1 = 1.05$) and hybridized DNA molecules ($n_2 = 1.15$) [21].

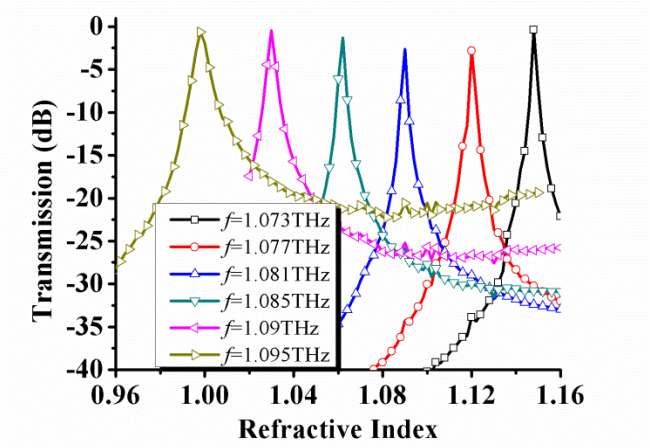

Figure 20 Transmission of gapped SSPP structure as a function of sample refractive index at different probe frequencies with sample load pattern D)

The location of the transmission peak, probe frequency, and the corresponding ON/OFF switching ratio for the detection of three refractive indices of $n_0 = 1$, $n_1 = 1.05$, and $n_2 = 1.15$ are summarized in Table 4. The extinction ratio for a refractive index change of $\Delta n/n = 0.02$ is over 20 dB for $n_1 = 1.05$, and $n_2 = 1.15$, representing denatured and hybridized DNA samples, indicating sharp peaks with high selectivity. In this way, with a single-arm sensor design based on gapped SSPP structure and tuning of the probe frequency, the differentiation of extremely small amount of DNA molecules with distinct binding states can be realized.

TABLE 4 DIFFERENCES IN PROBE FREQUENCY FOR THE DETECTION OF NO SAMPLE, DENATURED DNA, AND HYBRIDIZED DNA SAMPLES

Probe Frequency	Transmission Peak	On/Off switching ratio over $\Delta n/n = 0.02$
f=1.095THz	*n*=1(air)	15dB
f=1.087THz	*n*=1.05(denatured DNA)	23dB
f=1.073THz	*n*=1.15(hybridized DNA)	26dB

3.5 Analysis of lossy samples and samples with hydration

DNA, as a macro-sized bio-molecule, demonstrates strong interaction with *E-M* waves in the sub-THz to THz frequencies. This interaction is primarily detected as the shift of the dielectric constant of the molecules with the change of their binding states. This phenomenon is used to our advantage in the design of THz DNA sensors. As described in the previous sections of this chapter, various designs based on DC-SSPP structures are capable of differentiating subtle changes in the dielectric constant with only small amount of samples.

The dielectric constant of a molecule is a macroscopic manifestation of the motions of its chemical bonds and structural lattices. Therefore, a more comprehensive development of our work, in principle, should be based on the complete understanding of the DNA molecular structures. Unfortunately, this path is still largely uncharted, as the most comprehensive modeling of the molecular dynamics reported to-date could yet explain the spectral response of the bio-molecules in a satisfactory fashion. With macro-sized molecules such as DNA, the existence of complex chemical bonds and higher order molecular structures indicates complicated interaction with *E-M* waves in THz. The lack of progress in the molecular dynamic theory for macro-molecules, along with the limitation in the computational capabilities, contributes to the rather ambiguous and debatable interpretation of data when the state-of-the-art bio-molecular models are compared with experiment measurements [84, 24, 76, 85, 86].

Despite the obvious hurdle in modeling the DNA-THz interaction, we can still test our designs with more realistic assumptions. In addition to the refractive index model studied in the previous sections, the loss is added to account for the resonant absorption of DNA molecules in different binding states. Represented by the imaginary part of the dielectric constant, the loss factor will not only affect the output level of the bio-sensor design but will also change the dynamics of the sensing mechanism if it is comparable or significantly larger than the real part of the dielectric constant.

One can categorize the loss in DNA samples into two different types. Pure and dry DNA molecule has an intrinsic imaginary part in its dielectric constant, which gives rise to observable absorptions in the THz range [80]. In addition, water has a broad Debye relaxation peak in THz frequencies, which gives rise to a significant absorption band if the DNA sample is either hydrated or in the solution form. Using the parameters of the double-Debye model, the complex refractive index and loss factor of water are illustrated in Figure **21** [24, 87].

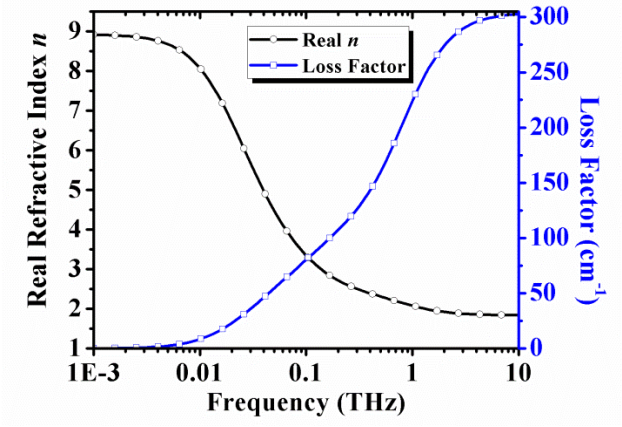

Figure 21 The real refractive index (black) and the loss factor (blue) of bulk water in sub-THz to THz frequencies

In the frequency range of 1 - 1.4 THz, the dielectric responses of both dry DNA and water are fairly constant. We take the average of the obtained values of all three materials over this frequency range, and their dielectric responses are obtained as [24, 80, 87]:

$$n_{denat-DNA} = 1.065 + i0.045, \varepsilon_{denat-DNA} = 1.132 + i0.097 \quad (40)$$

$$n_{hybri-DNA} = 1.18 + i0.136, \varepsilon_{hybri-DNA} = 1.374 + i0.321 \quad (41)$$

$$n_{water} = 2 + i0.5, \varepsilon_{water} = 3.75 + i2 \quad (42)$$

The efficacy of the DC-SSPP DNA sensor is tested using the values in (40), (41), and (42). The DC-SSPP MZI structure remains the same as the one we studied in **3.3**, and is shown in Figure 22. The dimensions of the structure are d = 100 μm, a/d = 0.2, h/d = 0.8, t/d = 1/3, W = 300 μm, and D = 250 μm.

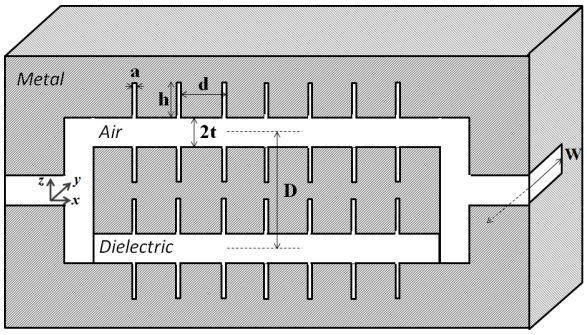

Figure 22 Illustration of the DC-SSPP MZI sensing architecture

Due to the fact that the *E-M* field is concentrated near the groove region when close to the SSPP resonance, one can choose to deposit the DNA samples in different manners. In a lossy

scenario, the localized sample deposition will not only reduce the amount of sample used, but it will also alleviate the total signal attenuation along propagation. We use three types of sample loading patterns, as illustrated in Figure **23**. They are (a) sample filling up one arm; (b) sample forming a thin layer on the opposing walls and (c) sample forming thin layers on the groove walls only, respectively.

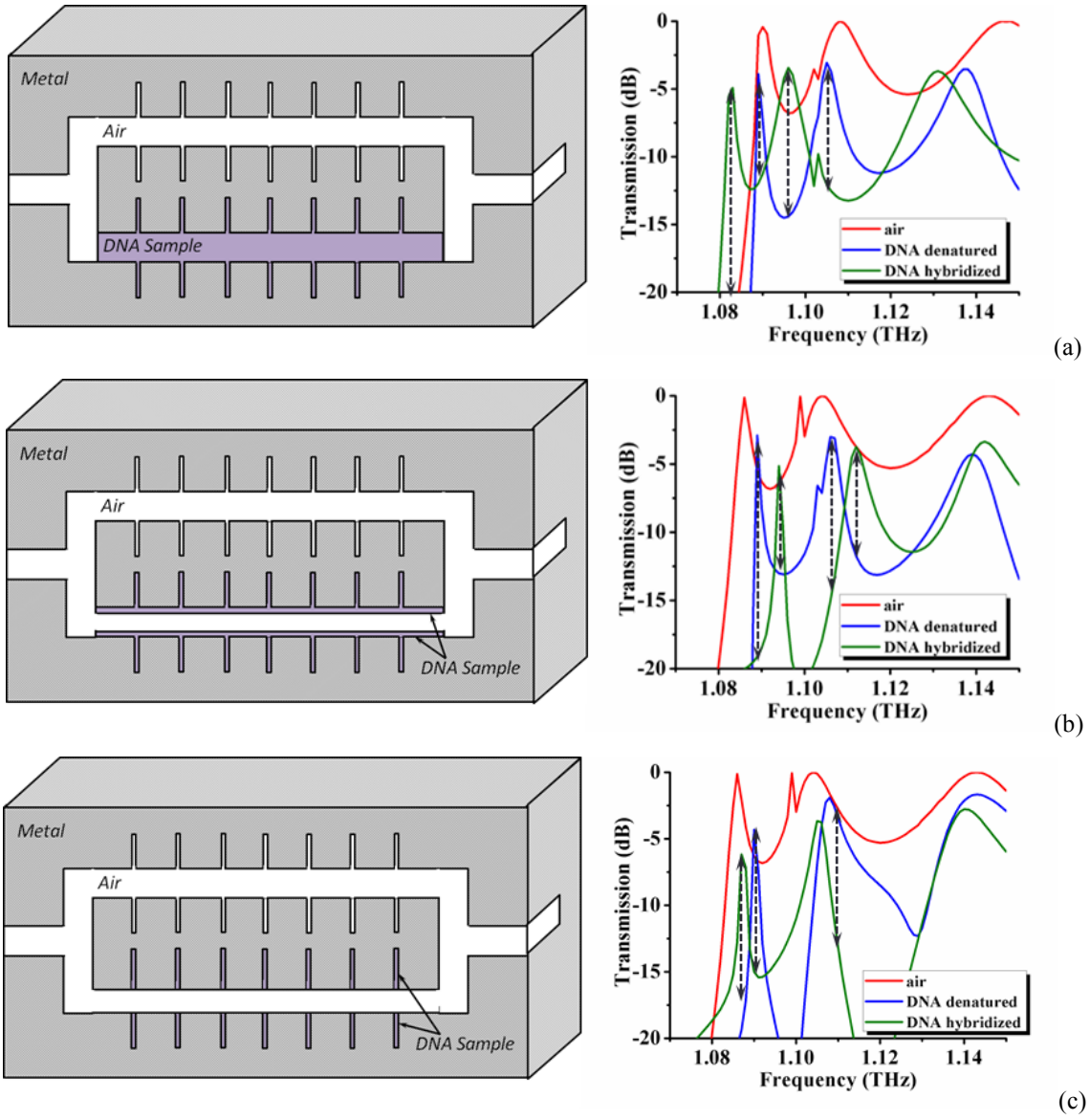

Figure 23 Transmission curves of the MZI SSPP sensing architecture with air, denatured DNA, and hybridized DNA molecules with complex dielectric constant. Three sample deposition patterns are included here, which are: (a) DNA sample fully loaded in one arm; (b) DNA samples form a thin layer on the opposing walls of one arm; and (c) DNA sample form a thin layer only within the groove area

In case (a), the spectral output of the sensing architecture is shown in Figure **23**(a). When compared with the ideal case where no imaginary part of the refractive index is considered, the transmission peaks are visibly lowered due to the material absorption. The differentiation between the curves of denatured and hybridized DNA is not pronounced when the frequency is far from the resonance. However, such differentiation is prominent when close to such resonance, where peaks are located at distinct frequencies with extinction ratio reaching and even far exceeding 10 dB.

In case (b) and (c), the lowering of the transmission curves is alleviated due to the smaller amount of sample used (Figure 23(b) and (c)). Similarly, when far from resonance, the spectral output of different DNA samples is less prominent. However, when close to the band gap, the distinct transmission peaks remain even with a minimum amount of sample forming only a thin layer on the groove walls. It is worth noting that the sample amount in case (c) is two orders of magnitude smaller than that in case (a), indicating enhanced detection limit even with the presence of loss.

With the MZI setup, we can still effectively differentiate DNA molecules in distinct binding states when loss factor of the dry molecular sample is considered. Such differentiation is much harder with hydration, as a result of the enormous imaginary part of refractive index of water. In fact, one major obstacle one has to overcome before the tag-free bio-sensing method can be widely applied to many biological assays is the sensing of humid, and ultimately, aqueous samples. Most of the biological processes take place in the solution phase. Sensing of these molecules and processes, therefore, needs to take place in the presence of water to best imitate the realistic scenario. Moreover, in the ultimate phase of bio-sensing which calls for *in-vivo* operation, water cannot be eliminated from the sample of interest, and its effect needs to be considered, and somehow separated to generate meaningful results.

We studied the effect of various hydration levels on the sensing performance of the DC-SSPP structure. In a DNA-water mixture, the effective complex dielectric constant is calculated using the Bruggeman model of the effective media theory, which is expressed as [85]:

$$\sum_{k=1}^{N} p_k \left(\frac{\varepsilon - \varepsilon_k}{\varepsilon_k + 2\varepsilon} \right) = 0 \tag{43}$$

$$\sum_{k=1}^{N} p_k = 1 \tag{44}$$

In (43) and (44), ε is the effective dielectric constant, p_k is the volume ratio of the k^{th} constituent in the mixture with the complex dielectric constant ε_k. As an example, we use a volume ratio of 10% and 25% of water in the wet DNA sample and apply them in a localized manner to the DC-SSPP MZI sensing structure. The transmitted output in these two cases is shown in Figure 24. The two types of DNA molecules can still be effectively differentiated when the chosen THz probe frequency is close to the SSPP resonance. Such differentiability indicates the potential of the SSPP sensing architectures in the humid and even aqueous environment (note 25%vol already represents a significant presence of bulk water).

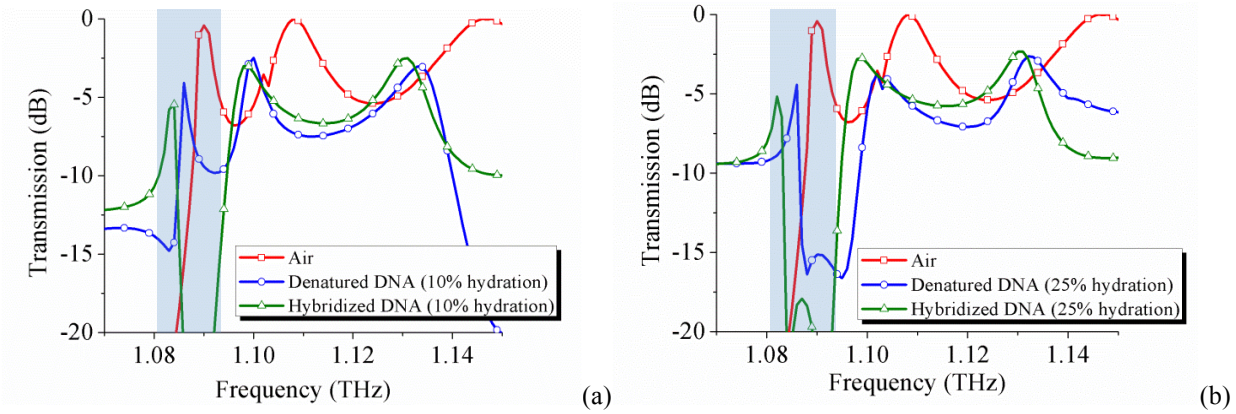

Figure 24 Transmission curves of the MZI SSPP sensing architecture with air, denatured DNA, and hybridized DNA molecules mixed with water. The wet DNA samples are deposited in the groove region only. The shaded area shows the frequency range with high differentiability of two types of wet DNA samples

CHAPTER IV Mach-Zehnder Interferometer (MZI) Comprising DC-SSPP Architectures and Its Application in Analog-to-Digital Conversion

4.1 Background

Analog-to-digital conversion is today an enabling technology for a wide range of applications, as digital signal processing, transmission, and storage have already replaced all-analog alternatives in many areas. Electronic analog-to-digital converters (ADC) have been primarily used for the task, although their performance is limited by the inherently small bandwidth and large clock instability [88, 89]. The sampling jitter, or known as the aperture jitter, is defined as the inability of electronic ADCs to sample at precisely defined times. Due to this factor, the bit resolution (the effective number of bits -- ENOB) and sampling rate are significantly limited for these ADC designs, making them incapable of meeting the ever growing demand for the device bandwidth and speed.

Optical ADC designs have therefore attracted much attention, due to its high carrier frequency and low temporal jitter obtainable through mode-locked lasers [90]. Optically assisted as well as all-optical ADCs have been studied by numerous research groups. The former takes advantage of the stable optical clock signal, but still relies on electronics for analog-to-digital conversion [91, 92, 93, 94]. The all-optical architectures, on the other hand, eliminate electronic sampling and conversion units at the same time, therefore are more likely to meet the stringent requirement in building faster and more accurate ADC components.

All-optical ADC can be realized in different ways. In the works by M. Johansson *et al.*, C. Pala *et al.,* and H. Zmuda *et al.*, for example, tunable lasers are used to first convert the analog electronic input into different output frequencies [95, 96, 97]. A frequency selective architecture is then used to spatially deflect signals at different wavelengths for them to be separately detected. The lack of widely tunable mode-locked lasers is the main drawback of this approach,

and its operating bandwidth is limited by the tuning speed of the laser. Other architectures, as represented in the work of M. J. Hayduk *et al.*, H. Sakata, and S. Oda *et al.*, use different amplitudes of the optic signal as the digitization standard [98, 99, 100, 101]. The amplitude modulation can be induced by the analog input through absorption stages, photonic crystals or nonlinear optical effects. The limitation of this method lies in the instability of the source laser powers, which cannot be differentiated from the power change induced by the actual analog input. The disadvantage of the source instability can be circumvented, however, with the introduction of reference beams. The all-optical ADC based on phase shifter arrays are therefore proposed by Taylor, where the interference of signals propagating through multiple phase modulators can result in a change in their far-field radiation patterns [102]. Such change is represented by the shift of the main radiation peak direction, which can be differentiated spatially by the detector arrays. Binary encoding can then be realized based on the spatial detection of the deflected optical signal.

In Taylor's work, in order to realize an *n*-bit digital readout, a multitude of phase shifters with geometrically increasing length are required. Although theoretically effective, the performance of this ADC suffers from the large number of the phase shifters and their mismatches, which both increase exponentially with the resolvable bits. The fundamental conflict comes from the fact that the full-width-at-half-maximum (FWHM) of the center peak of the far-field radiation pattern δ needs to be smaller than the separation between adjacent detectors Δ in order for it to be independently detected. For an *n*-bit ADC, without unwrapping a total number of 2^n detectors need to be placed within the limit of 2π phase shift. In this case, the ratio between Δ and δ is calculated to be equal to $N_p/2^n$, with N_p being the total number of phase shifters. Apparently with $N_p < 2^n$, an independent coupling of the deflected radiation maximum cannot be realized.

To decrease the number of phase shifters, digitized readout has to be obtained under partial coupling conditions, *i.e.*, when each of the detectors can receive only part of the energy of the main radiation peak. Following Taylor's work, J. Stigwall *et al.* proposed the structure comprising only a Mach-Zehnder interferometer (MZI) as the phase shifting element [103, 104]. Without arranging the detectors in a binary manner, the direct digital readout is impossible in this structure and invalid bits can give rise to increased bit error rate. However, with an optimized algorithm of treating the forbidden bits and unwrapping technique, the authors have successfully

demonstrated a 21-level ADC that can operate at 40 Giga-sample/sec (GS/s). Recently, Jarrahi *et al.* has also employed the MZI structure as the phase shifting stage to construct the all-optical ADC. To replace the power-hungry electro-optic stage which is employed in Stigwall's structure, in this work the quantum-confined Stark effect (QCSE) is used to induce the phase change in one or both arms of an MZI phase shifter. The diverted output is received by detector arrays arranged in a binary manner, and digitized output is read out directly [105]. Experimentally, the ADC has demonstrated up to 18 GS/s operation speed with the power consumption level of pJ/bit.

4.2 THz analog-to-digital converter: motivation

Although optical ADC has attracted much research interest, the big gap between electronics and optics makes it hard to be integrated with the VLSI system. The fundamental difference lies within the resonant transition between optical photons and electrons, which is rather inefficient due to the significant difference between their oscillation frequencies. The architectures reported in the previous section are mostly constructed with bulk optics components for the generation and manipulation of light waves. With separate light sources not considered as part of the architecture, the minimum size reported for all-optical ADC is still of millimeter scale [105].

On the other hand, THz electromagnetic oscillations are easier to interact resonantly with semiconductor electronics, making this frequency domain a more promising candidate for building higher speed and broader bandwidth integrated components. In fact, the accelerated progress in the THz research has been initiated by the discovery of resonant THz generation using semiconductor photoconductive switch as reported by D. Grischkowsky *et al.* in the late 1980's [106, 107, 108]. While details will be discussed in the subsequent Chapter, to-date a variety of technologies have been employed to generate and detect THz radiations in both pulsed and continuous-wave (CW) mode, and THz components and systems employing these technologies have steadily matured [109, 110]. Compared to the broad bandwidth of optics which has yet been fully utilized due to the lack of resonant coupling, the great increase in operating speed by the THz component can be more readily applied to the state-of-the-art electronic circuits. It is therefore very helpful if the all-optical components can be scaled down to THz frequencies.

In this chapter, we design a THz structure for the purpose of analog-to-digital conversion. The spatially resolved ADC design is chosen in this task due to its numerous advantages such as the enhanced stability, the direct binary readout, and the potential high-speed operations. As the most recent progress in spatially resolved all-optical ADC architecture, the work of Jarrahi *et al.* requires layered semiconductor structure comprising quantum wells for the transmission and phase modulation of light waves in optical frequency [105]. In THz domain, however, such index-guiding waveguide design shows small modal confinement factor and high signal power loss, therefore is incapable of delivering signals at these frequencies with good beam quality and radiation efficiency over distance. In fact, current works applying the conventional layered structure (including quantum wells) in THz frequencies must include certain modifications, such as using metal as the cladding material or operating under cryogenic conditions. They are mostly applied to emitter and detector designs and seldom do people use such structure as THz waveguiding solutions [111, 112, 113, 114, 115]. Applying the same concept of inducing phase change with QCSE is therefore quite difficult in THz domain.

With the help of the DC-SSPP structure, the confined propagation of THz signal in the form of a spoofed surface mode is made possible. As a result, room-temperature ADC operation in THz frequencies can be realized by using the DC-SSPP structure for beam deflection, replacing the QCSE stage in the optical ADC design. The architecture of the THz ADC will be explained in detail in the sections to follow.

4.3 THz beam steering using DC-SSPP MZI architecture: Theoretical analysis

The core stage of a spatially resolved ADC is the beam deflector. In our work, we design the beam deflector stage as depicted in Figure 25, where two arms of DC-SSPP waveguide are combined in the form of an MZI. This structure is similar to one of our DNA bio-sensor designs in Chapter III, only with the difference that the outputs from both branches are separate and are allowed to travel to the far field. With relative phase difference between two arms, the far-field radiation can be deflected significantly, as qualitatively sketched in the figure.

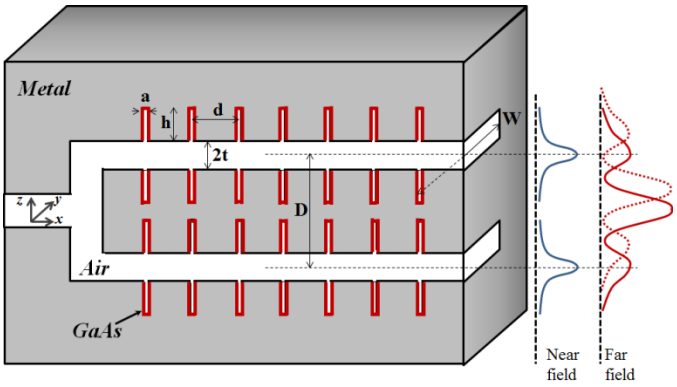

Figure 25 Cross section of the DC-SSPP beam steering structure with different geometric dimensions labeled. *W* is the width of the waveguide along the *y*-axis. The near-field and far-field radiation pattern are qualitatively sketched

The dispersion relation of DC-SSPP structure is calculated in Chapter II. The wavevectors as solved by (18) and (23) are functions of the refractive index *n*. As a result, when *n* is modulated by certain external stimuli, the wavevector will be altered correspondingly. Figure 26 shows the dispersion relation of a DC-SSPP waveguide with dimensions $d = 5.1$ μm, $a/d = 0.1$, $h/d = 0.7$, $t/d = 0.3$, and $W/d = 3$, as numerically calculated using MATLAB. The refractive index is set to change from 2.45 to 2.75, and phase modulation is clearly observed.

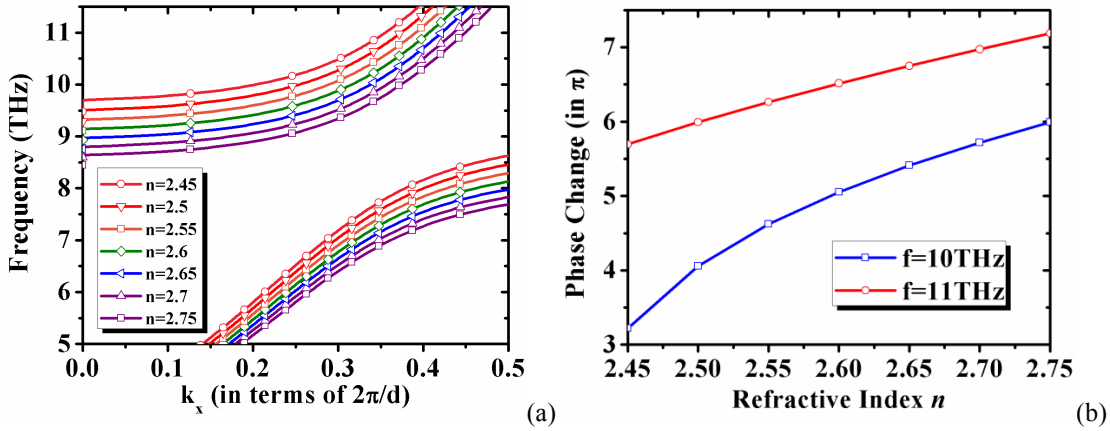

Figure 26 (a) Dispersion relations of the DC-SSPP waveguide with changing refractive index; (b) Phase change of the THz wave after propagating through 7 grooves. Both frequencies selected are slightly above the SSPP resonance

One may notice the strong similarity between Figure 26 and Figure 9 from Chapter III. In fact, both plots share the same mathematical formula. The difference, however, stems from the origin of the refractive index modulation. While the refractive index change in the bio-sensing scenario comes from the change of state in bio-molecules, in an ADC application, such change needs to be initiated by certain external control signals. In other words, instead of having the sample

immobilized to the structure prior to the measurement, in this case, the analog control signal serves as the input, which is expected to continuously modify the dielectric parameters of the structure.

A mechanism of transcribing the change of the external stimuli to the change in material property, and hence to the modulation of the propagating THz wave is therefore required in the design of the ADC. One effective mechanism of doing so is by changing the free carrier concentration in doped semiconductor, which can result in the modulation in its dielectric constant. Such mechanism has been used in a number of designs of phase modulators featuring different architectures. H.-T. Chen *et al.* has demonstrated a metamaterial THz phase modulator based on metallic split-ring resonator (SRR) design, after their pioneering works on the amplitude THz modulator using similar architectures [116, 117]. In their design, the voltage across the Schottky contact formed by the doped semiconductor (GaAs) layer and metal electrode causes depletion of free carriers in the semiconductor, changing the complex transmittance of the structure at THz frequencies. Phase modulators in the form of waveguides have also been proposed and fabricated by a number of research groups, where doped Si is used to form a thin strip ring resonator [118, 119, 120, 121]. The phase of the propagating signal can be adjusted by free carrier injection through a p-i-n junction, and as a result, the coupling efficiency of the ring resonator can be modulated. Due to the large loss tangent of Si in THz domain, however, such design can only be effectively applied up to near-infrared frequencies.

These works have inspired this study to incorporate doped semiconductor material in the THz ADC design to induce phase changes. Kramers-Kronig relationship dictates coupled evolution of the real and imaginary parts of the dielectric constant. A simplified yet accurate formulation of this relationship in describing the dielectric constant of semiconductors as a function of frequency is the Drude model. In optical frequencies (visible ~ mid-infrared), such model is expressed as:

$$\varepsilon(\omega) = \varepsilon_\infty - \frac{\omega_p^2}{\omega(\omega + i\Gamma)} \tag{45}$$

$$\omega_p = \sqrt{\frac{Ne^2}{\varepsilon_0 m^*}} \tag{46}$$

The variables in the Drude model are summarized in Table 5. The second term in (45) represents the contribution of plasmonic oscillation and coherent decay of electrons. Via ω_p, the dielectric constant is dependent on the free carrier density N of the semiconductor.

TABLE 5 LIST OF VARIABLES IN THE DIELECTRIC CONSTANT MODEL FOR HETEROPOLAR SEMICONDUCTORS

ε_∞	High-frequency dielectric constant
ε_s	Static dielectric constant
ε_0	Dielectric constant of vacuum
ω_p	Plasmonic resonance frequency
ω_{TO}	Transverse optical phonon resonance
ω	Frequency
Γ	Coherent decay factor of free carriers
γ	Phonon damping constant
N	Free carrier concentration
e	Charge of electron
m^*	Effective mass of electron

At longer wavelength, the Drude model needs to be modified due to the existence of optical phonon vibrations that largely reside in THz frequencies. For heteropolar semiconductors, an improved model describing the dielectric constant as a function of frequency is given as [122]:

$$\varepsilon(\omega) = \varepsilon_\infty + \frac{\omega_{TO}^2(\varepsilon_s - \varepsilon_\infty)}{\omega_{TO}^2 - \omega^2 - i\omega\gamma} - \frac{\omega_p^2}{\omega(\omega + i\Gamma)} \tag{47}$$

An extra term representing the contribution of phonon resonance is added in the modified model, with extra variables also described in Table 5. As an example, we calculated the dielectric constants of GaAs and InSb as a function of frequency and free carrier density using (47), which are illustrated in Figure 27 [123]. With the free carrier concentration of $N = 2{\times}10^{16} cm^{-3}$, the phonon resonances can be clearly marked by the sharp peak in the imaginary dielectric constant curve versus frequency (and abrupt change in the real curve), to be 8.05 THz for GaAs and 5.34 THz for InSb respectively. For comparison, the dielectric constant calculated using (45) is also included in Figure 27 (dashed line), where large discrepancies can be clearly observed.

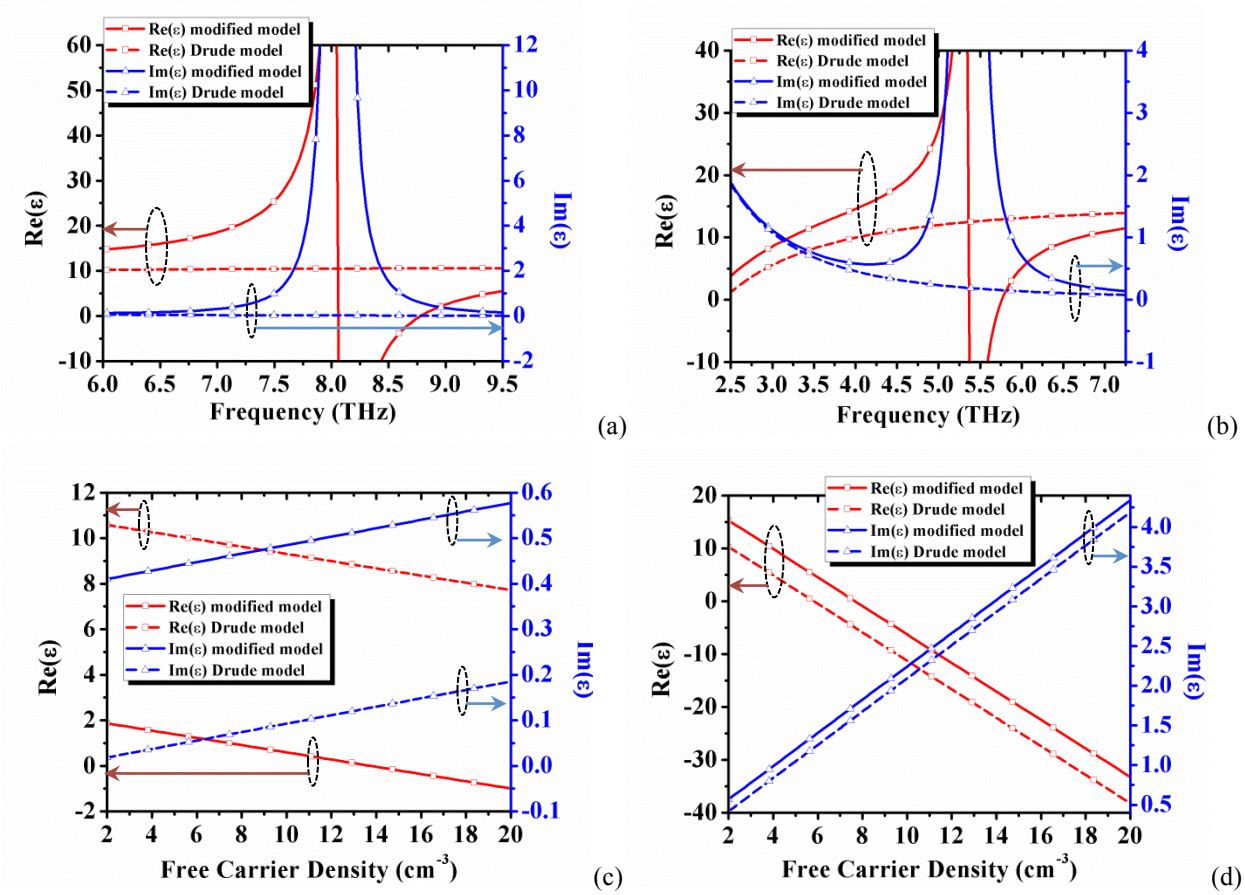

Figure 27 Complex dielectric constant (a) as a function of frequency for GaAs at $N = 2\times10^{16}cm^{-3}$; (b) as a function of frequency for InSb at $N = 2\times10^{16}cm^{-3}$; (c) as a function of free carrier density for GaAs at f = 8.92 THz; (d) as a function of free carrier density for InSb at f = 4.12 THz. The sharp peaks in (a) and (b) represent the optical phonon resonance.

Among the common semiconductor materials, GaAs has low intrinsic free carrier density, moderate carrier mobility and electron effective mass. As observed from Figure 27(c), in THz frequencies GaAs demonstrates an effective change of the Real ε with different free carrier densities and a mild change to the small Imaginary ε at the same time. Such properties are desirable in our application, where large modulation depth and stable power output throughout the working range are required. As a result, we choose GaAs as the semiconductor material in our design of the THz beam bender.

The working modes based on injection and depletion of free carriers in doped semiconductors are known as enhancement mode and depletion mode, respectively. We borrow these terminologies and will use them to refer to two different types of THz beam bender designs in

the following sections. As the mathematical model can only predict phase modulation of simple architectures with accuracy, we perform finite-element simulations on the realistic beam bender structures in order to verify the idea and optimize the design.

4.4 THz beam deflector: Enhancement mode

In enhancement mode, the DC-SSPP MZI structure can be either constructed with a hollow waveguide or with solid semiconductor fillings. The structure of the beam bender, in this case, has already been illustrated in Figure 25. Doped *n*-type GaAs is applied to both arms as thin deposition layers on the groove walls. Since the SSPP mode profile is largely confined to the groove area near resonance, the localized deposition of *n*-GaAs can effectively lower the insertion loss of the device without sacrificing the performance. In operation, free carriers are injected into the *n*-GaAs layer of one arm, resulting in refractive index changes. Such injection can be electrical, optical or thermal depending on its specific applications.

We use HFSS to simulate the structure as described above. The structure has the dimensions of d = 15 μm, a/d = 0.1, h/d = 0.7, t/d = 0.3, W = 45 μm, D = 37.5 μm. and the *n*-GaAs thickness is 0.3 μm. The angular output radiation from the MZI modulated by the free carrier concentration is illustrated in Figure 28. The *n*-GaAs in this case has an initial doping concentration of $N = 2\times10^{16}cm^{-3}$. At the operating frequency of 8.85 THz, such carrier density corresponds to the dielectric constant of $\varepsilon = 1.01 + i0.49$ ($n = 1.03 + i0.24$). In our simulation, the free carrier concentration is changed from $N = 2\times10^{16}cm^{-3}$ to $N = 2\times10^{17}cm^{-3}$ as a result of carrier injection. Figure 28(a) shows the change of the angular radiation power density up to $N = 1\times10^{17}cm^{-3}$. Accordingly, the angle of the maximum power of radiation as a function of the carrier density is plotted in Figure 28(b). A change up to 13° in the angle of radiation is observed for the MZI output, with the slope efficiency being $\sim 3°/10^{16}cm^{-3}$ in the linear region.

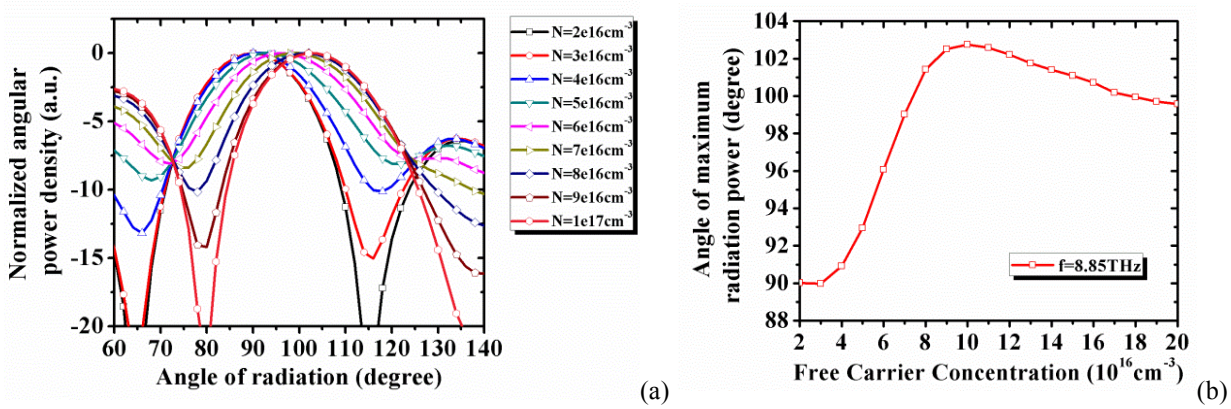

Figure 28 (a) Normalized angular power density of the beam bender output at f = 8.85 THz with different free carrier concentrations up to $N = 1\times10^{17}cm^{-3}$. (b) The angle of maximum radiation power as a function of free carrier concentration. 90° represents the case of normal output. In this plot, below $N = 9\times10^{16}cm^{-3}$ is the linear region, and beyond $N = 9\times10^{16}cm^{-3}$ is the saturation region

The beam bending effect is saturated beyond the free carrier density of $N = 9\times10^{16}cm^{-3}$, as a result of the Real dielectric constant becoming smaller than 0. In the saturation region, the deflection angle of the beam stays relatively constant, with a slightly decreasing trend due to the metal-like behavior of *n*-GaAs becoming more prominent, which effectively decreases the groove volume of the architecture. The deflection angle is stabilized when the *n*-GaAs acts completely like a metal, and in this case, the stabilized deflection angle of ~9° is achieved with $N > 2\times10^{17}cm^{-3}$.

As an alternative, DC-SSPP MZI beam deflector with semiconductor filling is proposed for its less stringent requirement on fabrication. In this case, the entire structure is made of intrinsic GaAs covered by metal, with the only exception in the grooves, where dopants are introduced to create a thin layer of *n*-type GaAs. Similarly, the localized *n*-GaAs can effectively lower the insertion loss of the device without sacrificing the performance of the beam bender.

We use HFSS to simulate the structure as described above, with the dimensions of each SSPP arm being d = 4.9 μm, a/d = 0.1, h/d = 0.7, t/d = 0.3, W/d = 3, and the separation between the arms being D/d = 2.5 [81]. The angular output radiation from the MZI modulated by the free carrier concentration is illustrated in Figure 29. The *n*-GaAs in this case has an initial doping concentration of $N = 2\times10^{16}cm^{-3}$. At the operating frequency of 10THz, such carrier density corresponds to the dielectric constant of $\varepsilon = 6.91 + i0.09$ ($n = 2.63 + i0.02$). In our simulation,

the free carrier concentration of the n-GaAs layer of thickness $\delta = 100\text{nm}$ is changed in one arm from $N = 2\times10^{16}cm^{-3}$ to $N = 2\times10^{17}cm^{-3}$ as a result of carrier injection. Figure 29(a) shows the change of the angular radiation power density. Accordingly, the angle of the maximum power of radiation as a function of the carrier density is plotted in Figure 29(b). A change up to 18° in the angle of radiation is observed for the MZI output.

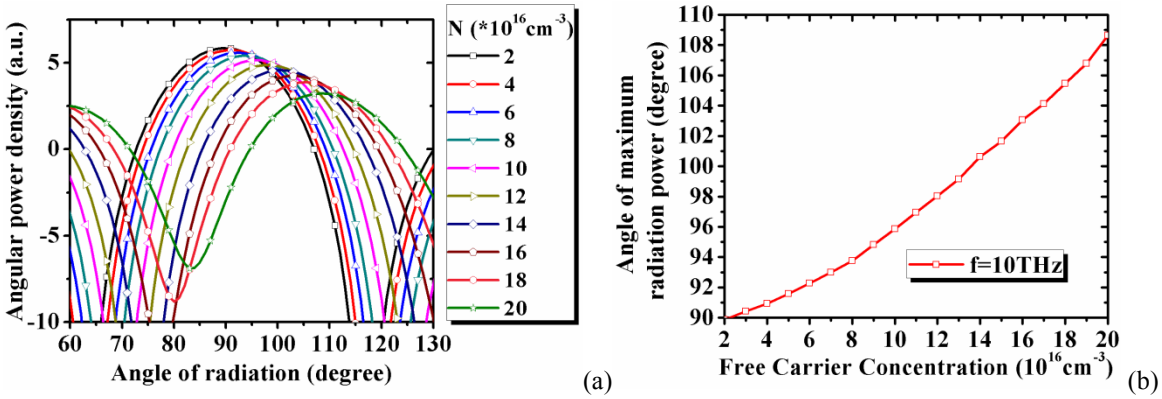

Figure 29 (a) Angular power density of the beam bender output at f = 10 THz with different free carrier densities. (b) Angle of maximum radiation power as a function of free carrier density. 90° represents normal output.

When compared with the hollow structure design, the slow decreasing of the diversion angle in the saturation region disappears in this case, as the Real refractive index of the n-GaAs is far from being negative. The slight nonlinearity of the curve in Figure 29(b) comes from the modified Drude model. From (46), (47) and Figure 27, it is easy to notice the linear evolution of ε with N. The phase change, on the other hand, is proportional to $n = \sqrt{\varepsilon} \propto \sqrt{N}$. A simple mathematic routine of Taylor expansion, however, shows that such nonlinearity can be mostly corrected when carriers are injected in both arms in a differential manner.

4.5 THz beam deflector: Depletion mode

Since the doping concentration of GaAs layer is much higher than its intrinsic free carrier density ($N_i = 2.1\times10^6 cm^{-3}$), the THz beam bender can also operate in depletion mode. In this mode, a Schottky contact is formed between the metal electrode and the GaAs layer. When applying a voltage across the contact, the free carriers will be extracted and a depletion zone will be formed. The thickness of the depletion zone as a function of the external voltage is given by [124]:

$$D_{dep} = \sqrt{\frac{2\varepsilon_s\varepsilon_0(V_{bi}+V)}{eN}} \tag{48}$$

Descriptions of the variables in (48) are also included in Table 5. V_{bi} = 0.75 V is the built-in voltage for the metal-GaAs junction, and V is the applied voltage [125]. Such relationship is plotted in Figure 30 for the doping density of $N = 1\times10^{17}cm^{-3}$ in GaAs and V from 0 to 3V.

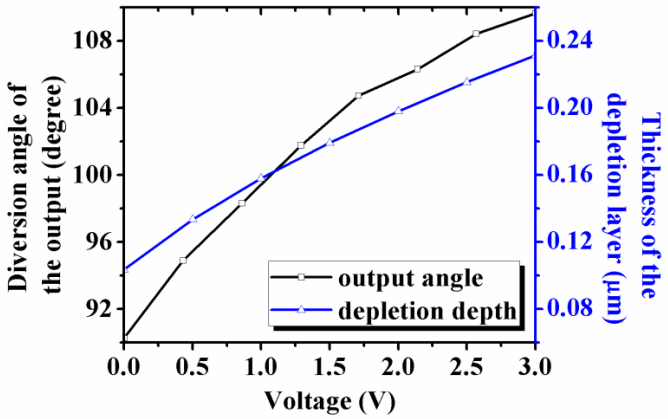

Figure 30 Thickness of the depletion layer in *n*-GaAs (blue) and the deflection angle of the beam output (black) as a function of voltage with the initial doping concentration of $N = 1\times10^{17}cm^{-3}$.

In depletion mode, the metal needs to form a thin electrode layer that covers the DC-SSPP structure, so that voltage modulation of the Schottky contact can be applied. This requirement has made the hollow waveguide design rather impractical from the standpoint of fabrication. Instead, the beam bender can only be constructed with solid semiconductor materials. As illustrated in Figure 31, the entire beam bending structure is made of intrinsic GaAs covered by metal, with the only exception in the grooves, where it is occupied entirely by *n*-type GaAs. When the *n*-GaAs layer in one arm is depleted by various thicknesses via external voltage, the phase of the propagating THz signal is changed and the output radiation is deflected accordingly.

Such deflection effect is also illustrated in Figure 30 for the structure with dimensions d = 4.75 μm, a/d = 0.1, h/d = 0.7, t/d = 0.3, W/d = 3, D/d = 2.5 and the initial free carrier concentration of $N = 1\times10^{17}cm^{-3}$. The operating frequency of the structure in this case is f = 10 THz, and a maximum deflection angle of 19° is achieved with the voltage of 3 V.

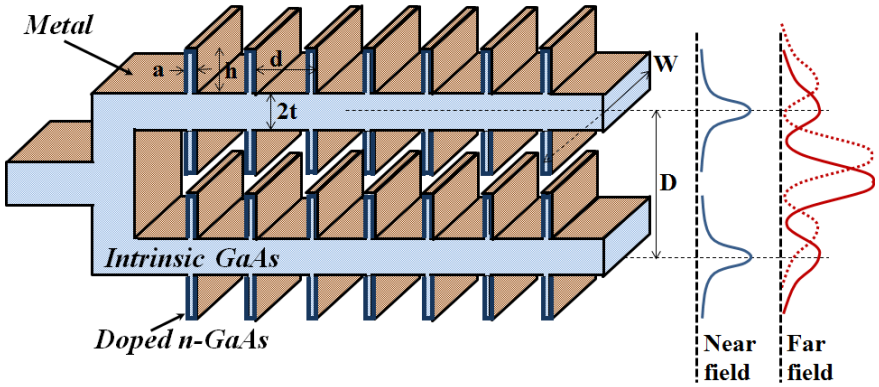

Figure 31 Cross section of the DC-SSPP beam steering structure with different geometric dimensions labeled. *W* is the width of the waveguide along the *y*-axis. The near-field and far-field radiation pattern are qualitatively sketched

In addition to the given example, the beam bending effect is not confined to specific structural dimensions. In fact, the initial doping concentration of *n*-GaAs and operating frequency of the structure can change in pairs, as long as the imaginary refractive index is not too large to prevent effective wave propagation. Correspondingly, the dimensions of the structure can be adjusted in scale, making this design highly adaptable to various requirements. In Figure **32**, the output angles as a function of the control voltage for different initial doping concentrations up to $N = 4\times10^{17}cm^{-3}$are shown and compared. The dimension of the structure is adjusted to d = 4.4 μm and d = 3.7 μm for the cases of $N = 2\times10^{17}cm^{-3}$ and $N = 4\times10^{17}cm^{-3}$, respectively, and similar beam bending effect can be observed.

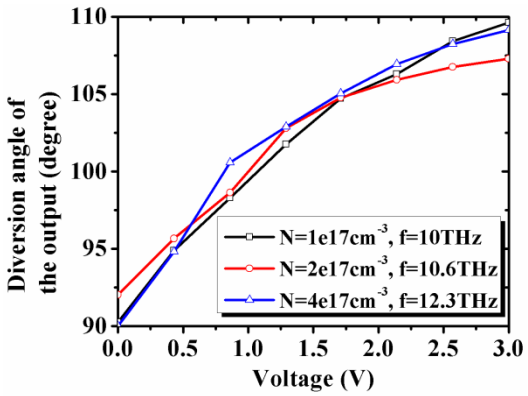

Figure 32 Deflection angle of the beam output as a function of voltage for initial doping density of $N = 1\times10^{17}\mathrm{cm}^{-3}$, $2\times10^{17}\mathrm{cm}^{-3}$, and $4\times10^{17}\mathrm{cm}^{-3}$.

In all circumstances, the nonlinear increase of the deflection angle is caused by the proportionality between D_{dep} and $\sqrt{V_{bi}+V}$. Again, such nonlinearity can be mostly corrected when a differential voltage is applied to both arms of the MZI structure.

4.6 THz analog-to-digital converter (ADC) comprising DC-SSPP MZI architecture

With the help of the DC-SSPP structure, the confined propagation of THz signal in the form of a spoofed surface mode is made possible. As a result, room-temperature ADC operation in THz frequencies can be realized by having the DC-SSPP beam bender as the first stage, followed by free-propagation region and detector arrays. The architecture of the ADC is shown in Figure 33. In our design, depletion mode is chosen to enable beam steering, and the control voltage serves as the analog input. The change in the position of radiation maxima can be interpreted into binary bits by the detector arrays when their positions and properties are carefully designed.

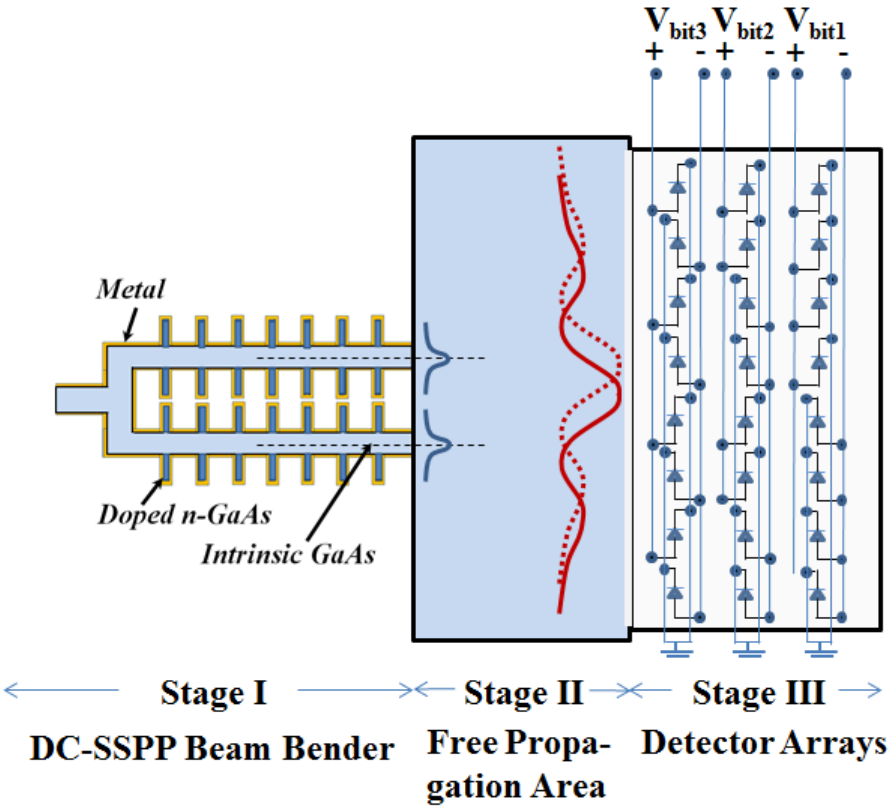

Figure 33 Sketch of the ADC based on the DC-SSPP beam bender as the first stage

The beam deflector stage of the THz ADC consists of 10 periods of grooves on each branch of the MZI and has dimensions of d = 4.75 μm, a/d = 0.1, h/d = 0.7, t/d = 0.3, W/d = 3, and D/d =

2.5. The initial doping concentration of the *n*-GaAs in the groove region is $N = 1\times10^{17}cm^{-3}$. When compared with the structures in the previous sections of this Chapter, a fully differential implementation is adopted here, where voltages are simultaneously applied to both arms of the MZI. This design is intended for a significant increase of the maximum deflection angle of the output. Additionally, the linearity of the deflection angle as a function of the input voltage is also notably improved by the differential design. In this section, the key output of the ADC will be reviewed and the digitization mechanism will be discussed. The detailed mathematical formulation of the SSPP ADC architecture, including the full-field analysis, the deflection angle calculation and the linearity will be included in the sections to follow.

As shown in Figure 34(a), with a voltage change of 0~3 V applied to the above-mentioned structure, the deflection angle of the THz output can change in a wide range of $\pm20°$. The symmetric shift of the beam peak position over normal radiation (90°) is important in ADC operations since the detector arrays are arranged in a mirror-symmetric manner. From Figure 34(b), this symmetry along with the perfect linearity of the output angle as a function of the input voltage is observed. To better illustrate the beam steering effect, the *E*-field distribution within the structure under the three voltages of V = 0 V, 1.5 V and 3 V are included in Figure 34(c)-(e), respectively.

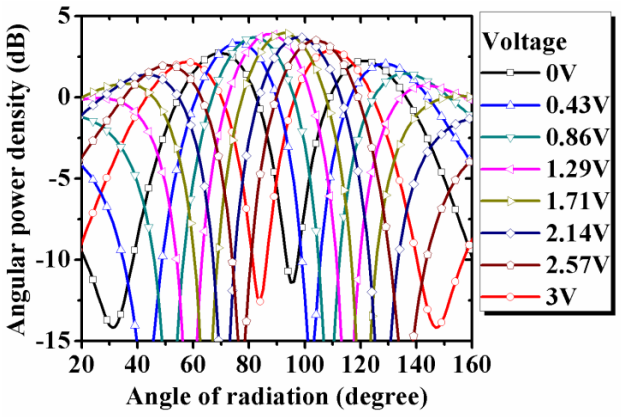

(a)

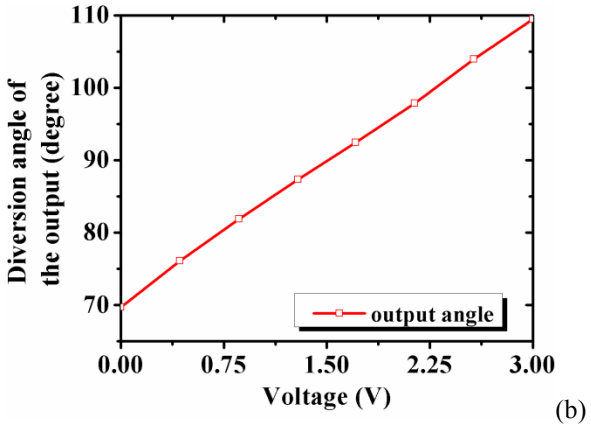

(b)

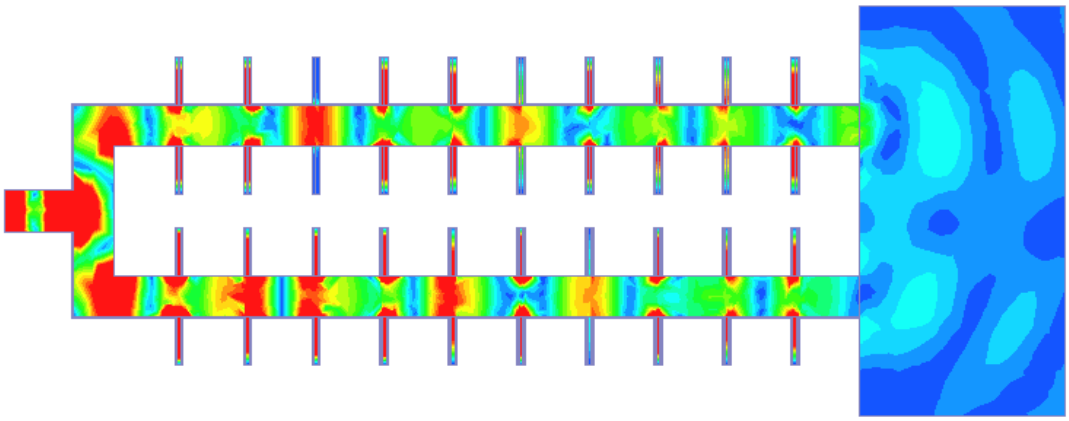

(c)

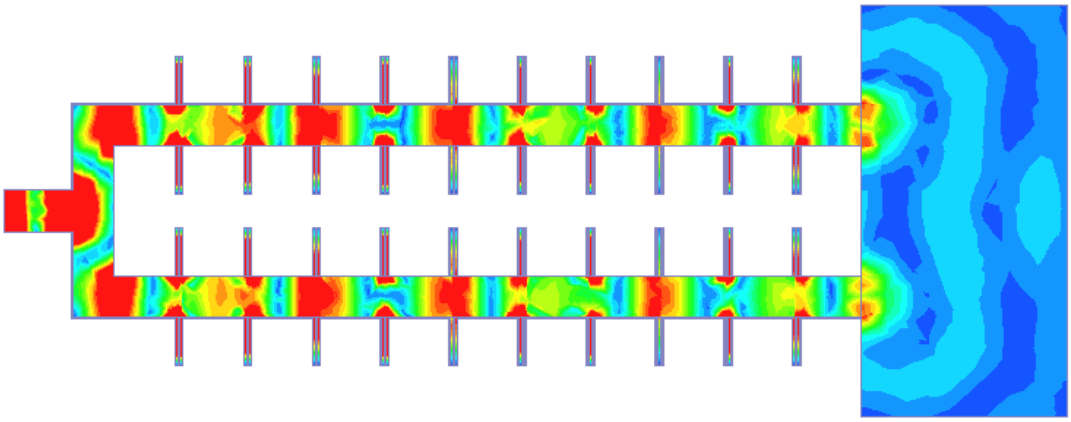

(d)

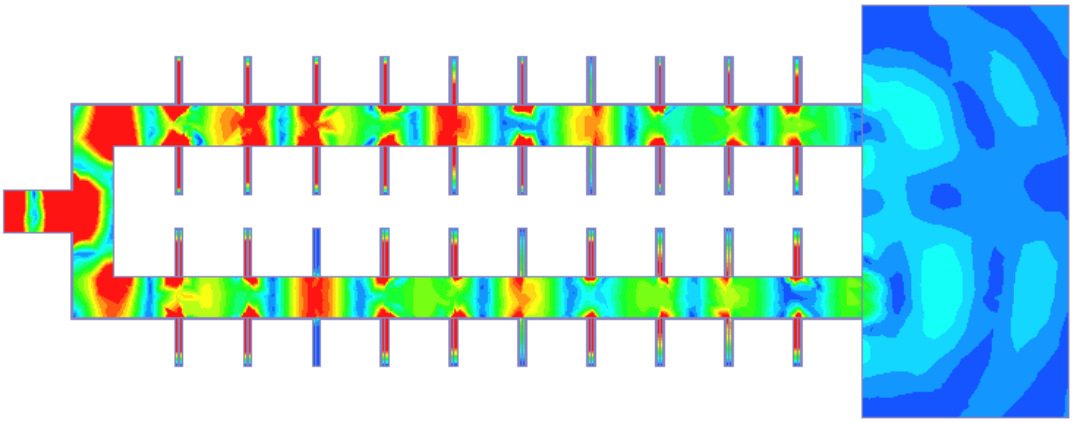

(e)

Figure 34 (a) Angular radiation power density and (b) diversion angle of the output maxima as a function of input voltage. The peak position of the radiation changes from 70° to 110° with a voltage input of 0-3 V. (c)-(e) *E*-field distribution at the voltage of V = 0 V, 1.5 V and 3 V, respectively

In the ideal case of the ADC design employing beam steering mechanisms, the main peak of the radiation pattern needs to be coupled independently into separate detectors in order to directly read out the digitized bits of the analog input. From the description in **4.1**, we know that at least $N_p = 2^n$ phase shifters are needed in this case in order to realize an n-bit ADC. In our design, however, only two SSPP branches are used to form the MZI structure. Therefore, for any attempt to have more than 1-bit digitized output, the radiation peak can only be partially coupled to separate detectors. The outcome as a result of the partial coupling is shown in Figure 35(a), where 8 linear detectors are used in an attempt to obtain a 3-bit output. It is observed that only one period of the sign change can be obtained for all three bits in this case, which indicates an actual ADC resolution of only one bit.

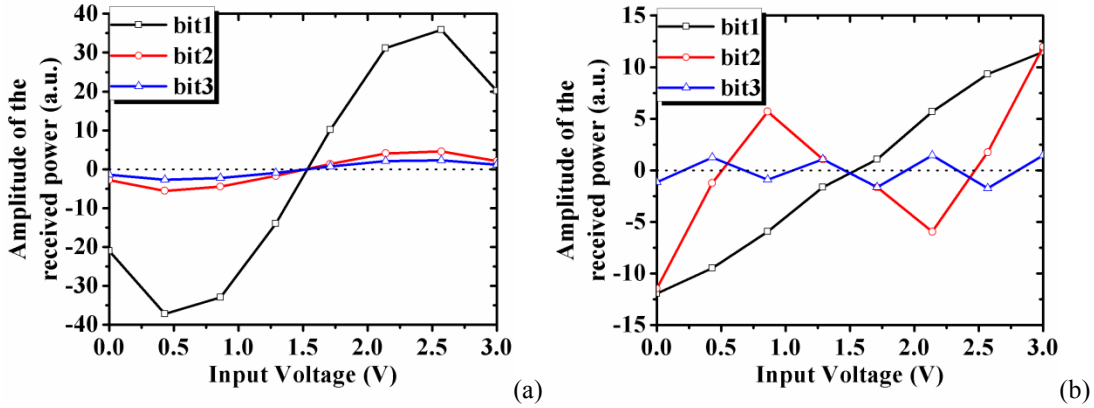

Figure 35 3-bit readout from the ADC with 0-3V voltage input with (a) linear and (b) nonlinear detector arrays

To tackle this problem, we need to employ detectors operating in saturated conditions. With carefully designed gains and nonlinearities for the detector arrays, we can manage to have up to 2^n periods of sign change within 2π phase shift for the n^{th} bit output. In Table 6 we summarized an example of such design for an array of 8 detectors (#1-#8 from top to bottom as shown in Figure 33). The non-unity relative gain is used to emphasize the leading and trailing edges of the main radiation peak. The saturation power is determined in a way that a considerable width centered on the peak is deemed as equal by the detectors, and its value is given in the arbitrary unit so that it can be in reality proportionally adjusted to fit different THz source and detector specifications. Figure 35(b) shows the digitized readout from such detector array. A 3-bit output

can be obtained in this case with the analog input voltage changing from 0 V to 3 V. In the actual realization of the ADC, the detector arrays will have a finite width along the transverse dimension (*y*-axis) of the output beam. Due to the non-uniform power distribution along this direction, the gains and nonlinearities of the detector stages need to be adjusted accordingly.

TABLE 6 DESIGN OF DETECTOR ARRAYS IN A 3-BIT ADC IN TERMS OF GAIN AND SATURATION POWER

Detector #	Gain (relative)	Saturation power (a.u.)
1,8	2×	3
2,7	2×	5
3,6	2×	7
4,5	3×	9

4.7 THz ADC comprising DC-SSPP MZI architecture: Analytical model on beam deflection

As described in previous sections, the deflection of the field maxima is caused by the cumulative phase difference of the THz signal between the two arms. In turn, this phase difference is caused by the material dielectric property change inside the grooved DC-SSPP structure with voltage modulation. In Chapter I, a mathematical formulation (23) has been obtained to calculate the dispersion relation of the SSPP resonance mode. Although the original equation is only valid for structures consisted of a single material, it can be slightly modified as below to accommodate the modulation of material properties in the ADC operation:

$$1+\sum_{n=-\infty}^{\infty}\frac{k_{z,II}}{k_{z,I}^{(n)}}\frac{|T_n|^2}{\tan\left(k_{z,I}^{(n)}t\right)}\tan\left(k_{z,II}h\right)=0 \tag{49}$$

Where

$$v_{y,I}^2=k_{0,I}^2-k_{y,I}^2=\left(k_{x,I}^{(n)}\right)^2+\left(k_{z,I}^{(n)}\right)^2 \text{ in Region I}$$

$$k_{y,I}=\frac{m\pi}{W}\cdot n_I, m=1,2,\ldots \text{ in Region I}$$

$$v_{y,II}^2=k_{0,II}^2-k_{y,II}^2=k_{x,II}^2+k_{z,II}^2 \text{ in Region II}$$

$$k_{y,II}=\frac{m\pi}{W}\cdot n_{II}, m=1,2,\ldots \text{ in Region II}$$

$$k_{x,II}=\frac{l\pi}{a}\cdot n_{II}, l=0,1,2,\ldots \text{in Region II}$$

Please refer to Figure **1** for the definition of Region I and Region II. In our ADC beam deflector design, the Region I consists of intrinsic GaAs and the dielectric properties therein remains constant. In Region II, however, the material constitution can change with the modulated

spacing-charge layer thickness, as calculated by (**48**). Under the first order of approximation, the effective dielectric constant is assumed to be a linear, proportional combination of the doped and depleted GaAs properties. In this case, the applied voltage (in V), the depletion percentage (defined as depleted thickness/entire n-GaAs thickness), and the effective refractive index (real part only as the imaginary *n* is quite small and negligible) is summarized in the following table:

TABLE 7 EFFECTIVE REFRACTIVE INDEX CALCULATIONS WITH INPUT VOLTAGE VARIATIONS

Voltage (V)	0	0.43	0.86	1.29	1.71	2.14	2.57	3
Depletion Percentage	43.2%	54.1%	63.2%	71.1%	78.3%	84.8%	90.9%	96.6%
Effective Refractive Index	2.5344	2.5617	2.5843	2.6040	2.6218	2.6380	2.6531	2.6673

By inserting the effective refractive index in (**49**), we can obtain the dispersion relations of the DC-SSPP arm under various voltage input. An example is shown below in Figure **36**, where the dispersion relation of the THz mode in a single-arm SSPP structure with V = 0 V and V = 3 V are plotted.

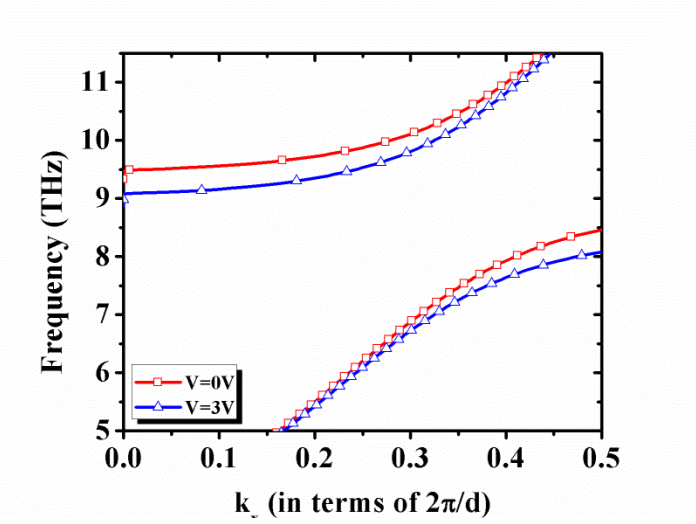

Figure 36 Dispersion relation of the ADC SSPP arm with input voltage of 0V (red) and 3V (blue)

In the case of a 3-bit ADC design, an 8-level voltage digitization is required. The *x*-axis wavevector at f = 10 THz, as predicted by the above-mentioned analytical model, is then calculated and summarized in the following table:

TABLE 8 WAVEVECTOR ALONG PROPAGATION WITH INPUT VOLTAGE VARIATIONS

Voltage (V)	0	0.43	0.86	1.29	1.71	2.14	2.57	3
Wavevector in *x*-axis (in $2\pi/d$)	0.2806	0.2936	0.3025	0.3092	0.3145	0.3189	0.3226	0.3258

These wavevectors, after the THz mode propagates through 10 periods of the SSPP waveguide, will accumulate to generate a significant amount of phase differences. In fact, the optical path difference (*O.P.D*) between two applied voltages of V_1 and V_2 can be calculated using the following equation:

$$O.P.D_{V1,V2} = \left(k_{x,V1} - k_{x,V2}\right) * 10d * \frac{\lambda_n}{2\pi} \tag{50}$$

In (**50**), λ_n stands for the signal wavelength in the medium. Following the *O.P.D* calculation, the deflection angle is predicted using the classic double-slit interferometer theory. It is summarized as follows:

$$\theta = asin\left(\frac{O.P.D}{D}\right) \tag{51}$$

Note *D* represents the distance between two arms of the MZI structure. To verify the validity of this modeling effort, the theoretically predicted deflection angle by (**51**) is given in the following figure side by side with the simulation result directly obtained using HFSS:

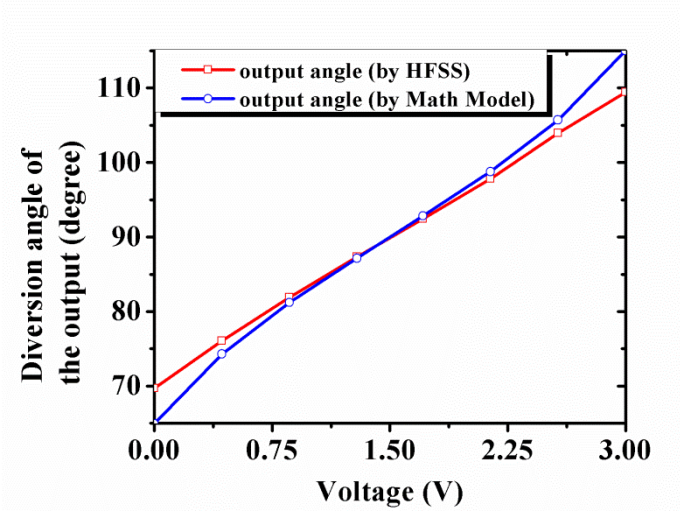

Figure 37 Comparison between mathematical model (blue) and HFSS (red) on the cumulative phase of signal at *f* = 10 THz as a function of input voltage

As observed from Figure **37**, the theoretical prediction is in general quite accurate. Discrepancy tends to be slightly bigger on the two extremes in the applied voltage. Due to the multitude of assumptions made in the mathematic model, the numerical result has a tendency of 'pushing-up' the dispersion curves to slightly higher frequency. This, in general, makes the phase difference higher when the propagating mode is above the SSPP resonance. Such phenomenon is discussed in detail in Chapter III, and one can refer to Figure **10** for more detailed error analysis.

The MZI structure in our ADC design generates far-field radiation field based on the phase difference between the two arms. The coherent interference of the MZI arms can be illustrated by the following figure:

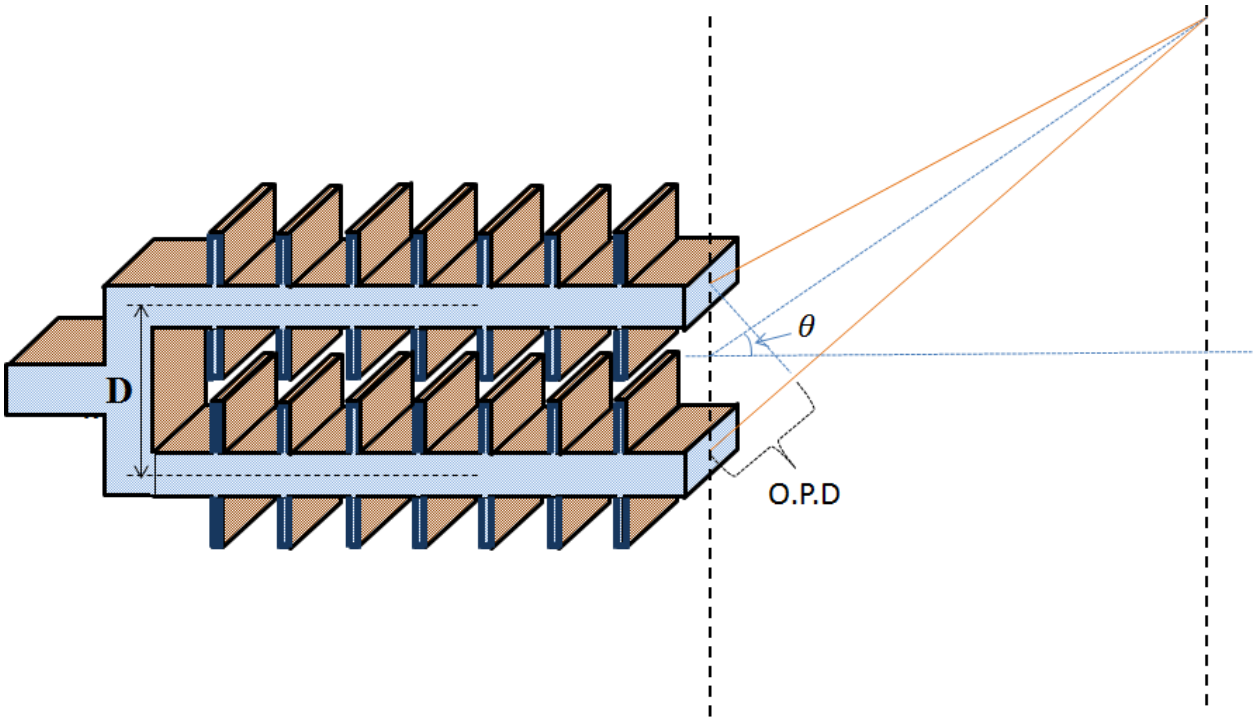

Figure 38 Illustration of the far-field radiation of the ADC design and the definition of O.P.D. and deflection angle

In Figure **38**, D represents the distance between the two arms. The optical path difference ($O.P.D$) at an arbitrary angle θ is therefore expressed as:

$$O.P.D_{\theta} = Dsin\theta + \Delta\varphi \tag{52}$$

In (**52**), $\Delta\varphi$ represents the voltage induced phase difference between the two arms. Particularly, when $V1$ and $V2$ are applied to the MZI simultaneously, such phase difference can be expressed as:

$$\Delta\varphi_{V1,V2} = \left(k_{x,V1} - k_{x,V2}\right) * 10d * \frac{\lambda_n}{2\pi} \tag{53}$$

The interference pattern in the far field can then be calculated using the following formula:

$$E_\theta = E_1 e^{i\Phi} + E_2 e^{i\left(\Phi + O.P.D_\theta * \frac{2\pi}{\lambda_n}\right)} \tag{54}$$

To the first order of approximation, we assume $E_1 = E_2 = E_0$. Therefore we have:

$$|E_\theta| = E_0 \left|2cos\left(O.P.D_\theta * \frac{\pi}{\lambda_n}\right) e^{i\Phi}\right| = 2E_0 \left|cos\left(O.P.D_\theta * \frac{\pi}{\lambda_n}\right)\right| \tag{55}$$

In other words

$$|E_\theta| = 2E_0 \left|cos\left[\frac{1}{2}\left(Dsin\theta\frac{2\pi}{\lambda_n} + \left(k_{x,V1} - k_{x,V2}\right) * 10d\right)\right]\right| \tag{56}$$

To include the diffraction effect, another factor has to be incorporated. The diffraction factor is calculated using the following formula:

$$F_{diffraction} = sinc\left(\frac{d_{eff}\pi}{\lambda_n} sin\theta\right) \tag{57}$$

Therefore the overall far-field radiation field can be expressed as:

$$|E_\theta| = 2E_0 \left|cos\left[\frac{1}{2}\left(Dsin\theta\frac{2\pi}{\lambda_n} + \left(k_{x,V1} - k_{x,V2}\right) * 10d\right)\right]\right| * sinc\left(\frac{d_{eff}\pi}{\lambda_n} sin\theta\right) \tag{58}$$

To verify this mathematical model, we calculate the radiation pattern of the MZI SSPP structure using the same dimensions as in our ADC design. The field plot is given in Figure **39**(a), where it is compared with the simulation result we obtained with HFSS software in Figure **39**(b). As observed, the theoretical prediction generates reasonably accurate results.

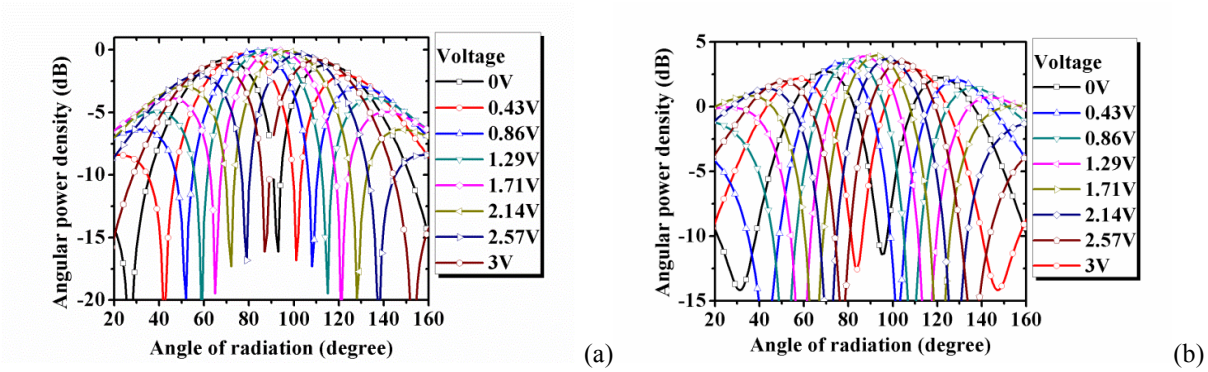

Figure 39 Comparison of the far-field radiation between (a) the mathematical model and (b) HFSS simulation

In the mathematical model, we assume that the outputs from two arms are having the same amplitude and transverse field distribution, with the only difference being their phase accumulation. In real cases, these assumptions will not be exactly true. On one hand, the field amplitude from the two arms will show minor differences as a result of the SSPP selectivity. On the other hand, the transverse field will also differ between two arms as a result of the complex nature of the SSPP mode. These two factors have contributed to the disparity between the two radiation plots in Figure **39**. In other words, the SSPP mode variation with different voltage input has made the interference pattern to deviate from the ideal theoretical prediction as presented in this section.

4.8 THz ADC comprising DC-SSPP MZI architecture: Linearity

From the previous section, the effective dielectric properties are assumed to be the linear, proportional combination of the doped and depleted GaAs contributions. In this case, the effective refractive index can be calculated as:

$$n_{eff} = \frac{D_{dep} n_i + (D_{tot} - D_{dep}) n_d}{D_{tot}} \tag{59}$$

In (**59**), n_i and n_d represent the refractive indices of the intrinsic and doped GaAs, respectively. D_{tot} is the total thickness of the doped GaAs layer without depletion voltage in the groove region. Now, let us define the following constant coefficients:

$$A = \frac{n_i - n_d}{D_{tot}} \sqrt{\frac{2\varepsilon_s \varepsilon_0}{eN}}$$

$$B = n_d$$

By express the depletion thickness with the input voltage using (**48**), the effective refractive index can then be expressed as:

$$n_{eff} = A\sqrt{V_{bi} + V} + B \tag{60}$$

The n_{eff} will give rise to different phase change in the two arms of the MZI when different voltages have been applied. In an ideal case, the phase difference between the MZI arms can be calculated as:

$$\Delta\Phi_{V1,V2} = \left(k_{x,V1} - k_{x,V2}\right) * 10d = \frac{2\pi}{\lambda_0}\left(n_{eff,V1} - n_{eff,V2}\right) * 10d \tag{61}$$

In real cases, since the dispersion relation of SSPP mode is determined by the effective refractive indices of combined Region I and Region II, the phase difference expression will be more complicated than (**61**). Using the first order of approximation, we can actually estimate the effective dielectric property even across the two regions by their linear combination. The resultant mathematical formulation, however, still remains to be similar. In fact, by examining the numerical result from the previous section, the linear relation between the effective index of the groove region and the resultant wavevector of the SSPP mode can be in general observed. Without loss of generality, in our calculation onwards, we will use (**61**) to establish the linear relation between the applied voltage and the ADC output.

By combining (**60**) and (**61**), we have the following formula:

$$\Delta\Phi_{V1,V2} = \frac{2\pi}{\lambda_0} A\left(\sqrt{V_{bi} + V_1} - \sqrt{V_{bi} + V_2}\right) * 10d \tag{62}$$

Typically, (**62**) indicates a square root relation between the applied voltage and the phase difference. This statement is particularly true when one of the voltages in fixed, where V_1 or V_2 remains a constant. In our case, however, the ADC is operating in the differential manner. The voltages applied to both arms are conjugate to each other, in other words:

$$V_1 + V_2 = V_{max} \tag{63}$$

In this case, (**62**) can be re-written as:

$$\Delta\Phi_{V1,V2} = \frac{2\pi}{\lambda_0} A\left(\sqrt{V_{bi} + V_1} - \sqrt{V_{bi} + V_{max} - V_1}\right) * 10d \tag{64}$$

$$= \frac{2\pi}{\lambda_0} A\sqrt{V_{max}}\left(\sqrt{\frac{V_{bi}+V_1}{V_{max}}} - \sqrt{\frac{V_{bi}+V_{max}-V_1}{V_{max}}}\right) * 10d$$

To simplify the mathematic formula, we define the following constant coefficient:

$$A' = \frac{2\pi}{\lambda_0} A\sqrt{V_{max}} * 10d \tag{65}$$

Using (**65**), we can re-write the equation in the following form, so that a Taylor expansion can be executed to further simplify the mathematical relation:

$$\begin{aligned}
\Delta\Phi_{V1,V2} &= A'\left(\sqrt{1+\frac{V_{bi}+V_1-V_{max}}{V_{max}}} - \sqrt{1+\frac{V_{bi}-V_1}{V_{max}}}\right) \\
&= A'\left[\left(1+\frac{1}{2}\frac{V_{bi}+V_1-V_{max}}{V_{max}} - \frac{1}{8}\left(\frac{V_{bi}+V_1-V_{max}}{V_{max}}\right)^2\right) - \left(1+\frac{1}{2}\frac{V_{bi}-V_1}{V_{max}} - \frac{1}{8}\left(\frac{V_{bi}-V_1}{V_{max}}\right)^2\right)\right] \\
&= A'\left[\frac{1}{2}\left(\frac{V_{bi}+V_1-V_{max}}{V_{max}} - \frac{V_{bi}-V_1}{V_{max}}\right) - \frac{1}{8}\left(\left(\frac{V_{bi}+V_1-V_{max}}{V_{max}}\right)^2 - \left(\frac{V_{bi}-V_1}{V_{max}}\right)^2\right)\right] \\
&= A'\left[\frac{1}{2}\left(\frac{2V_1}{V_{max}} - 1\right) - \frac{1}{8}\left(\left(\frac{V_{bi}+V_1}{V_{max}}\right)^2 - \left(\frac{V_{bi}-V_1}{V_{max}}\right)^2 - 2\frac{V_{bi}+V_1}{V_{max}} + 1\right)\right] \\
&= A'\left[\frac{1}{2}\left(\frac{2V_1}{V_{max}} - 1\right) - \frac{1}{8}\left(\frac{4V_{bi}V_1}{{V_{max}}^2} - 2\frac{V_{bi}+V_1}{V_{max}} + 1\right)\right] \\
&= A'\left[\left(\frac{5}{4V_{max}} - \frac{V_{bi}}{2{V_{max}}^2}\right)V_1 - \left(\frac{1}{2} - \frac{1}{4}\frac{V_{bi}}{V_{max}} + \frac{1}{8}\right)\right]
\end{aligned} \tag{66}$$

The Taylor expansion as shown above is valid since

$$\frac{V_{bi}+V_1-V_{max}}{V_{max}} < 1$$

$$\frac{V_{bi}-V_1}{V_{max}} < 1$$

To retain the accuracy of such expansion, only the $O(x^3)$ term and onwards are omitted, which is a reasonably good approximation. From the previous section, we also know that the deflection angle changes linearly with the phase difference:

$$\theta = asin\left(\frac{O.P.D}{D}\right) \approx \frac{O.P.D}{D} = \frac{\Delta\Phi_{V1,V2}}{D}\frac{\lambda_n}{2\pi} \tag{67}$$

Combining (**66**) and (**67**), one can clear observe the linear relation between the deflection angle of the ADC and the input modulation voltage. Such linearity is the direct outcome of the balanced arm of the MZI configuration and the differential voltage input design.

4.9 THz ADC comprising DC-SSPP MZI architecture: Effective Number of Bits (ENOB)

An ideal ADC converts an analog input into equal-spaced quantized output. As shown in Figure 40, the conversion relationship of an ideal ADC consists of step functions that are exactly 1 least-significant-bit (LSB) apart. The quantization noise, in this case, is represented by a sawtooth function, and the signal-to-noise ratio (SNR) for a sine wave analog input is given by the following formula:

$$\mathrm{SNR} = 1.76 + 6.02b \tag{68}$$

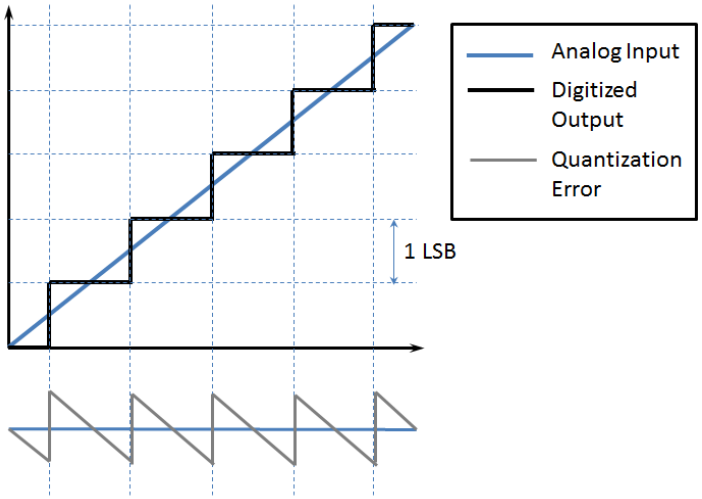

Figure 40 Analog-to-digital conversion relationship and quantization noise for ideal ADC

In (68), b stands for the bit resolution. In reality, ADC designs are never ideal. Typical non-ideality factors include unequal spacing as well as the nonlinearity and saturation of the digitization function. These factors give rise to excessive noise in the form of wave distortion and harmonic generation, which will deteriorate the bit resolution of the ADC from its designed specification. The effective number of bits (ENOB) is therefore defined as the actual number of bits that can be resolved after all nonidealities in the design are considered. The ENOB can be calculated using (68), with the SNR in the formula being replaced by the signal-to-noise-and-distortion ratio (SINAD). When compared with SNR, SINAD counts for the contribution of nonlinear frequency generations (harmonics) and is typically of a lowered value.

$$\text{ENOB} = \frac{\text{SINAD} - 1.76}{6.02} \tag{69}$$

In order to calculate the ENOB of the THz ADC design, more detailed simulation on the beam steering structure is carried out and the detector array readout with higher voltage resolution is given in Figure 41(a). The quantization conversion relationship and noise function are depicted in Figure 41(b) and (c), respectively, where their counterparts of ideal ADC designs are included as well for the purpose of comparison. It can be observed that the THz ADC is not ideal, which will give rise to a smaller ENOB than the 3-bit resolution it is designed for.

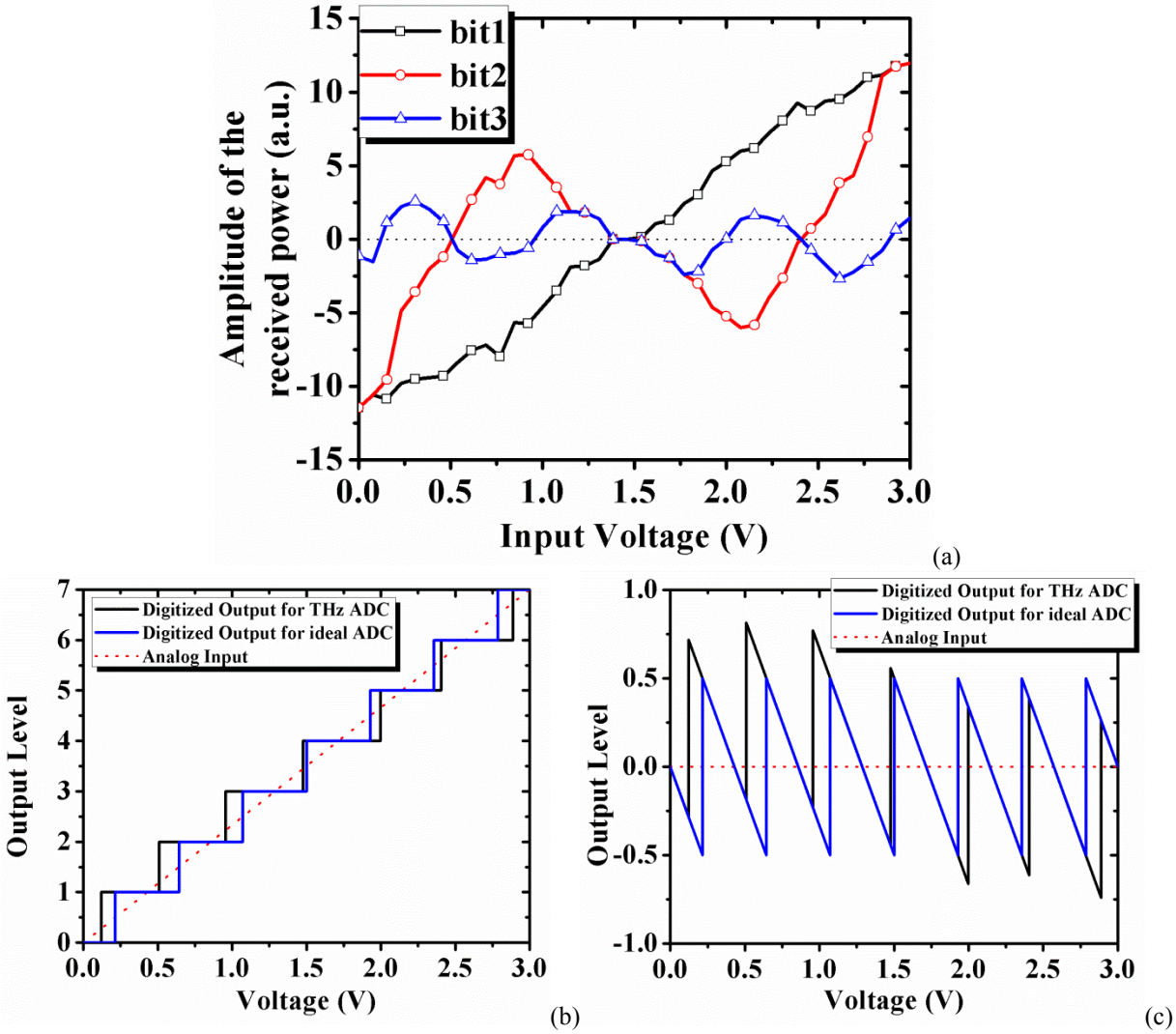

Figure 41 (a) Bit readout from the ADC with 0 – 3 V voltage input with nonlinear detector arrays. (b) Conversion relationship and (c) quantization error function of the DC-SSPP THz ADC in comparison with the ideal ADC

The SINAD of the THz ADC is calculated by taking the root-mean-square (RMS) value of the sine analog input and dividing it by the RMS value of the quantization noise function. The

ENOB is then calculated using (69) to be 2.82 bits. Compared with state-of-the-art electronic ADCs reported to-date, this ENOB deterioration from the nominal bit resolution is among the smallest we have seen. By optimizing the mirror symmetry, linearity and detector array designs, we can potentially make the THz ADC to perform closer to ideal. In other words, we can potentially achieve a closer fit of the THz ADC's conversion and noise functions to those of ideal ADCs, which will generate higher ENOB at the same time.

4.10 THz ADC comprising DC-SSPP MZI architecture: Bandwidth calculation

The effort to increase the operating bandwidth of electrical sampling ADC is challenged by the relatively large temporal jitter of the sampling signal [88]. Recent developments in optical ADC are vowed to solve this problem by using ultra-stable sampling pulses of mode-locked lasers, while the speed of operation of such design is still limited by the bandwidth of the E-O modulator stage. Despite the small jitter of the pulses, the repetition rate of the state-of-the-art mode-locked laser is mostly in the sub-GHz range. As a result, to date the bandwidth characterization of optical sampling ADCs is carried out by either using sinusoidal continuous wave analog input or by generating significantly aliased signals after digitization with serious under-sampling [105, 89].

In our THz ADC design, it is helpful to calculate the operating bandwidth of the beam deflector stage (analogy to the E-O modulator stage in optical ADC), which will give us a good idea of the speed performance of our design in comparison to its optical counterparts. In depletion mode, the Schottky contact formed by the electrode and doped *n*-GaAs layer contributes to a finite phase settling time of the modulator, which in turn will determine the operating bandwidth (BW) of the stage as described by the following formula [105]:

$$BW \leq \frac{1}{2ln2(b+1)T_{set}} \tag{70}$$

In (70), T_{set} stands for the phase settling time, and b is the bit depth of the ADC ($b = 3$ in our case). T_{set} is determined by the carrier transit time and the parasitic RC time constant of the Schottky contact, which will be calculated separately in the following paragraphs.

When the space-charge region is reasonably thin, and the electric field is not very strong, the carrier transit time of a Schottky contact can be calculated via strict math. When a distance

comparable to the mean free path of the carrier motion separates the two terminals, the electrons undergo ballistic transport, which is best described as the accelerated motion under the external bias voltage. The dc-transit time, in this case, can be obtained as [126]:

$$\tau_{trans} = \frac{\pi}{2}\sqrt{\frac{m^*\varepsilon_s\varepsilon_0}{Ne^2}} = \frac{\pi\sqrt{\varepsilon_s}}{2\omega_p} \tag{71}$$

In our case with $N = 1{\times}10^{17}cm^{-3}$, τ_{trans} is calculated by (71) to be 0.08 ps. It corresponds to an average carrier drift velocity in the order of $10^6 m/s$, which far exceeds the saturation drift velocity $v_{sat} = 8{\times}10^4 m/s$ for GaAs at this electric field intensity. This indicates that the electron motion in our case cannot be simplified as ideal ballistic transport. Instead, collision plays an important role in the carrier motion and can significantly slow it down. The realistic τ_{trans} is therefore estimated with the following equation, with d being the carrier displacement:

$$\tau_{trans} = \frac{d}{v_{sat}} \tag{72}$$

In the worst case, where $d = 0.13\mu m$ for a voltage change of 3 V, the time constant is calculated to be 1.63 ps. Although it is significantly larger than the ideal case, the small, picosecond scale of this term still shows the intrinsic advantage of devices working in the depletion mode, as the operation speed is not limited by the slow diffusion of minority carriers.

The RC time constant, on the other hand, is determined by the series resistance and the barrier capacitance of the Schottky contact. These characteristic impedance values are dependent on the geometric dimension of the contact and are further influenced by non-ideality factors such as skin effect, carrier inertia, and displacement current. In a realistic situation, one can define the dielectric relaxation frequency ω_d and the scattering frequency ω_s to count for the effect of the above-mentioned non-idealities [127]:

$$\omega_d = \frac{\sigma}{\varepsilon_s\varepsilon_0} \tag{73}$$

$$\omega_s = \frac{e}{m^*\mu} \tag{74}$$

In (73) and (74), σ is the conductivity, and μ represents the carrier mobility of the semiconductor. Assuming the Schottky contact and the semiconductor substrate are of circular

shapes of radii r and r' respectively, the bulk spread impedance and skin effect impedance are then defined as (μ_0 being the permeability of vacuum) [127]:

$$Z_s = \frac{1}{4\sigma r}\left[\frac{1}{1+j\omega/\omega_s} + j\omega/\omega_d\right]^{-1} \tag{75}$$

$$Z' = \frac{ln(r'/r)}{2\pi}\sqrt{\frac{j\omega\mu_0}{\sigma}}\left[\sqrt{\frac{1}{1+j\omega/\omega_s} + j\omega/\omega_d}\right]^{-1} \tag{76}$$

The barrier capacitance is calculated by:

$$C = \frac{\pi r^2 \varepsilon_s \varepsilon_0}{D_{dep}} = \pi r^2 \sqrt{\frac{eN\varepsilon_s\varepsilon_0}{2(V_{bi}+V)}} \tag{77}$$

The RC time constant can then be obtained by solving the following equations:

$$Re(Z_s) + Re(Z') - \frac{1}{\omega C} = 0 \tag{78}$$

$$\tau_{RC} = 2\pi/\omega \tag{79}$$

In our structure, the surface area of the substrate on the groove region is $A = 14.2\mu m \times 3.3\mu m$. To the first order of approximation, we choose r' = 3.86 μm in our calculation to represent a substrate of the same area. The RC time constant is plotted against the radius r in Figure 42.

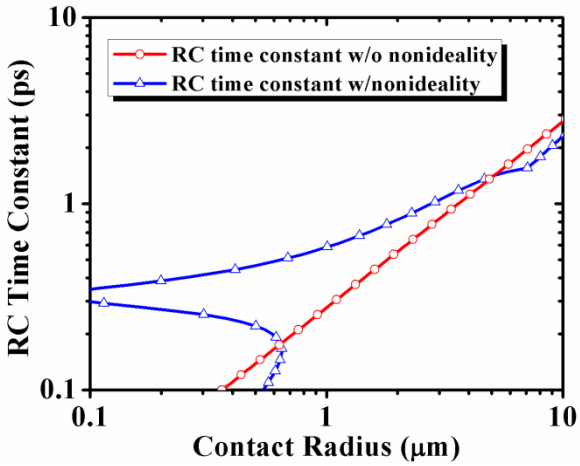

Figure 42 The RC time constant calculated both with and without the non-ideality factors (skin effect, carrier inertia and displacement current) as a function of the Schottky contact radius.

In Figure 42, the RC time constant increases proportionally with the Schottky contact radius when skin effect, carrier inertia, and displacement current are not considered in the calculation.

In real-world scenarios, however, those non-ideality factors can have a significant influence on the characteristic impedance of the contact, and RC time constant is seen to deteriorate greatly from the ideal case when it is close to the plasmonic resonance frequency of GaAs. In our case, τ_{RC} is reasonably far from such resonance with the Schottky contact having the same area as the substrate and is calculated to be 1.2 ps.

Taking both τ_{trans} and τ_{RC} back into (70), the maximum operating speed of our ADC is estimated to be 63.7 GS/s. It is noted that both the carrier transit time and the RC time constant can be further reduced by incorporating higher initial doping concentration of the *n*-GaAs region, which will feature smaller device dimensions as well as a thinner space-charge region.

One must note that in the BW calculation of this section, only the surface area of a single groove is used in (**78**), with the assumption that each groove is driven individually. This is a feasible design option by separating the driving circuit among grooves but is certainly not ideal. A more compact ADC design enabling a common drive scheme of all grooves will be discussed in detail in the last section of this chapter.

4.11 THz ADC comprising DC-SSPP MZI architecture: Time-domain simulation

In order to better illustrate the time-domain behavior of the SSPP ADC design, a GNU GPL-based open source software named MIT Electromagnetic Equation Propagation (MEEP) is used for the modeling and temporal domain simulation. Compared with Ansoft HFSS, which is a powerful FEA simulation engine, the FDTD nature of MEEP has made it the ideal tool to conduct transient analyses of the SSPP ADC structure. The temporal domain output from MEEP with arbitrary, yet well-defined input signals can directly generate field distribution map of the structure progressing in time. It can also partially simulate the voltage sweep of the ADC to mimic the radiation output of the structure in operation, which is the element missing from the HFSS simulations.

In MEEP, the modeling for both the SSPP ADC structure and the material dispersion is script-based and fully parameterized. A qualitative illustration of the architecture under simulation, as generated by MEEP, is given in Figure **43**:

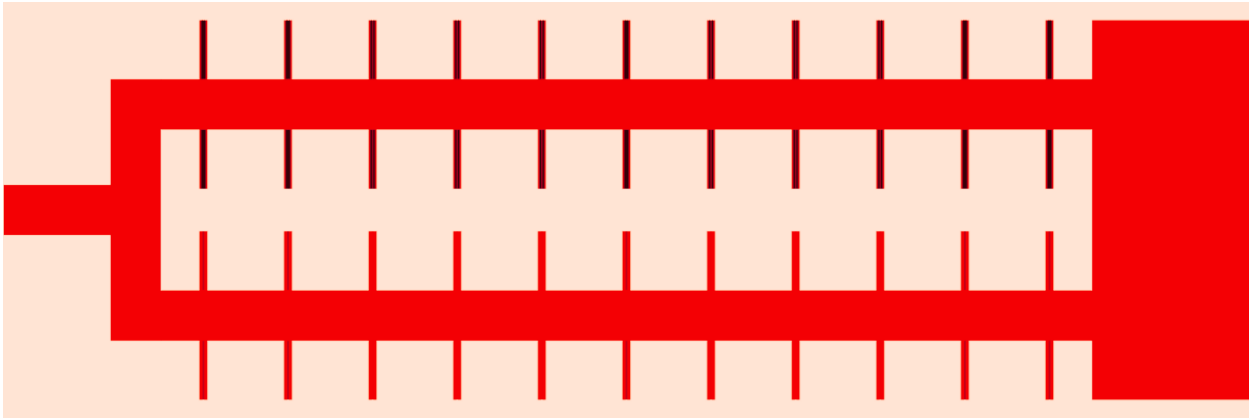

Figure 43 DC-SSPP ADC structure in the MEEP simulation, generated by MEEP script

In Figure **43**, the light pink color represents the metal, the red color is the intrinsic GaAs, and the black color represents the doped n-GaAs. The voltage input, in this case, is $V_1 = 0$ V in the upper arm and $V_2 = 3$ V in the lower arm, making the depletion layer thickness the thinnest in the upper arm and the greatest in the lower arm, respectively.

This model is versatile enough to simulate the temporal behavior of the doubly corrugated SSPP structure in both single-arm and MZI configurations. Under the single-arm assumption, the simulation can generate the dispersion relation, albeit with poor convergence near the SSPP resonance. An example is shown in Figure **44** with the comparison between the modulation voltage of 0 V and 3 V. As can be observed, MEEP can only generate a handful of data with good convergence due to the mesh instability of the software. Nonetheless, if we focus on the flat region of the dispersion relation (highlighted by the green circle), a small yet discernable difference in the dispersion relation is observed. This result corresponds well with the $f = 10$ THz carrier frequency selection in the ADC design, where it equals 0.033 in the normalized scale (x-axis).

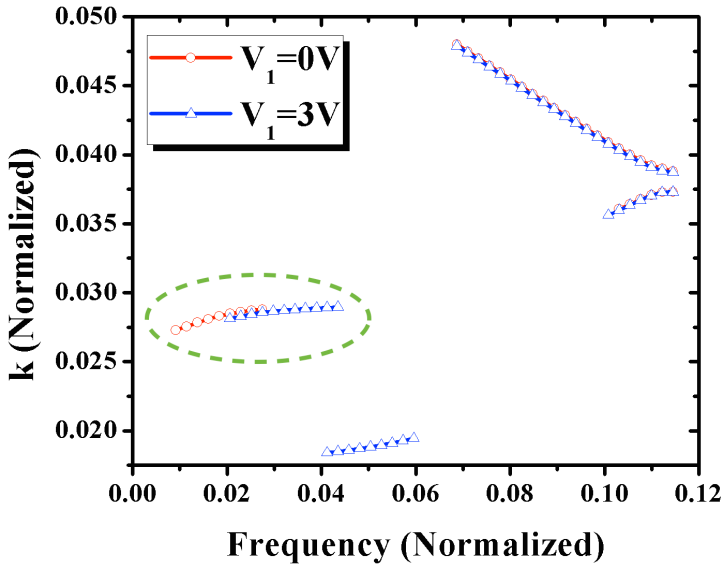

Figure 44 Dispersion relation of the single-arm DC-SSPP structure from the ADC design as simulated by MEEP, with the input of V = 0 V (red) and V = 3 V (blue)

When the MEEP script model is applied to the ADC architecture with the MZI configuration, the temporal domain nature of the FDTD makes the simulation of real-time field distribution possible. This transient analysis capability of MEEP has made the SSPP ADC operating mechanism a straightforward item that can be readily illustrated.

An example is given in Figure **45**. In this figure, a comparison of the *E-M* field distribution with a variation of the structural ADC dimensions is demonstrated. From the prior sections, the beam steering angle of the SSPP ADC is known to depend on both the dimensions of the structure and the carrier signal frequency. The frequency is typically chosen to coincide with both the SSPP resonance of the structure and the maximum change of the dielectric constant of the GaAs material. With the carrier signal frequency of f = 10THz, Figure **45** (a) shows the field distribution with d = 4.75 μm, which is the original ADC design dimension. In this case, an obvious beam steering effect is observed in accordance with the FEA simulation by HFSS. Figure **45** (b), on the other hand, shows the field distribution with d = 4.9 μm. The beam steering is almost non-existent due to the carrier frequency being away from the SSPP resonance.

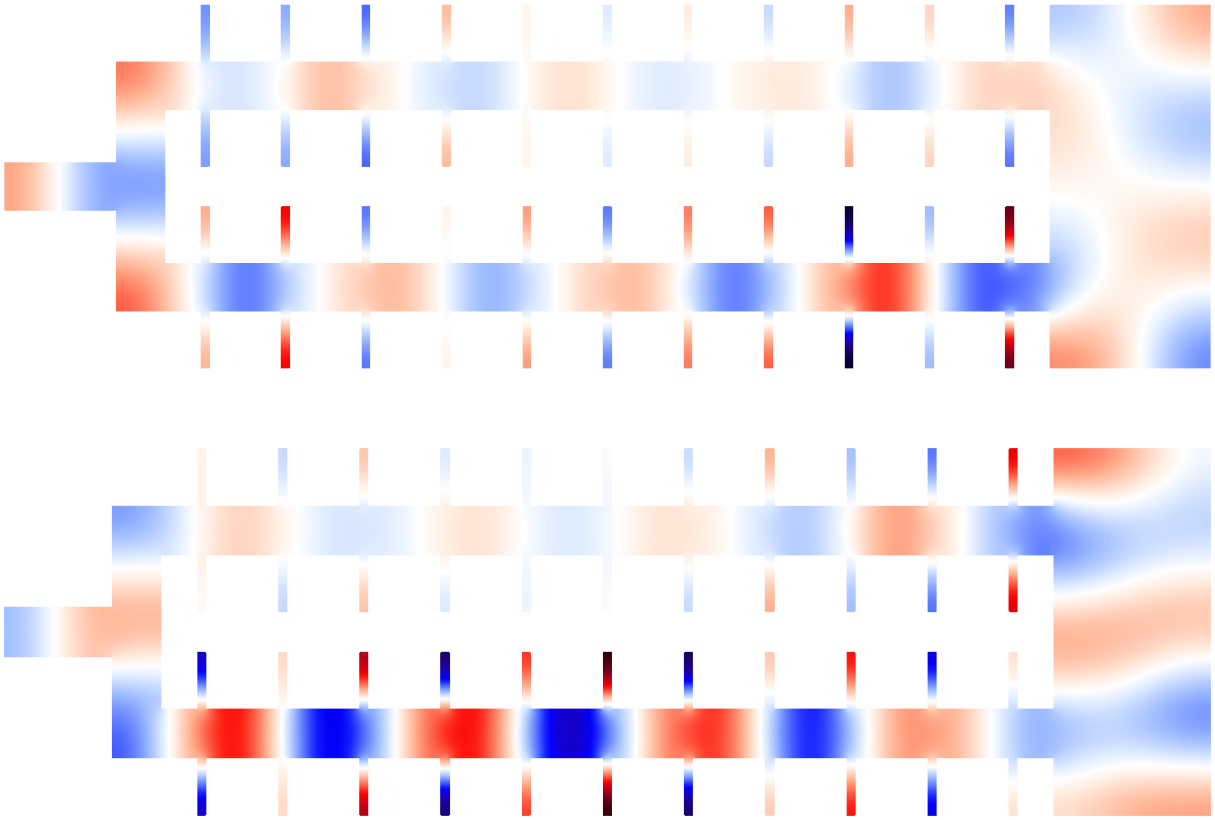

Figure 45 Comparison of the *E-M* field distribution between two ADC dimensions: (a) d = 4.75 μm; (b) d = 4.9 μm. Carrier signal frequency is selected to be f = 10 THz in accordance to the original ADC design

Under the optimized dimension d = 4.75 μm, the beam steering effect is shown in Figure **46** with the ADC voltage at V_1 = 0 V, 1.5 V, and 3 V respectively. To take advantage of the FDTD simulation, the wave input is selected to be a Gaussian pulse with the center frequency of f= 10 THz and a bandwidth of 1.5 THz, mimicking a realistic narrow-band carrier wave signal. It is clearly observed that the beam can be steered from one side to the opposite with the voltage sweeping the entire range of 0 – 3 V. The radiation is not deflected with V_1 = 1.5 V input, as the two MZI arms are balanced with the same voltage being applied. Unfortunately, there is no existing scripting solution and library support to enable MEEP simulation of time-variant signal input of arbitrary profile, nor is the time-varying structure definition supported in the current version of the software. Nonetheless, with this result, the time-variant FDTD simulation by MEEP can be considered as a visualized reference to the previous analytical sections.

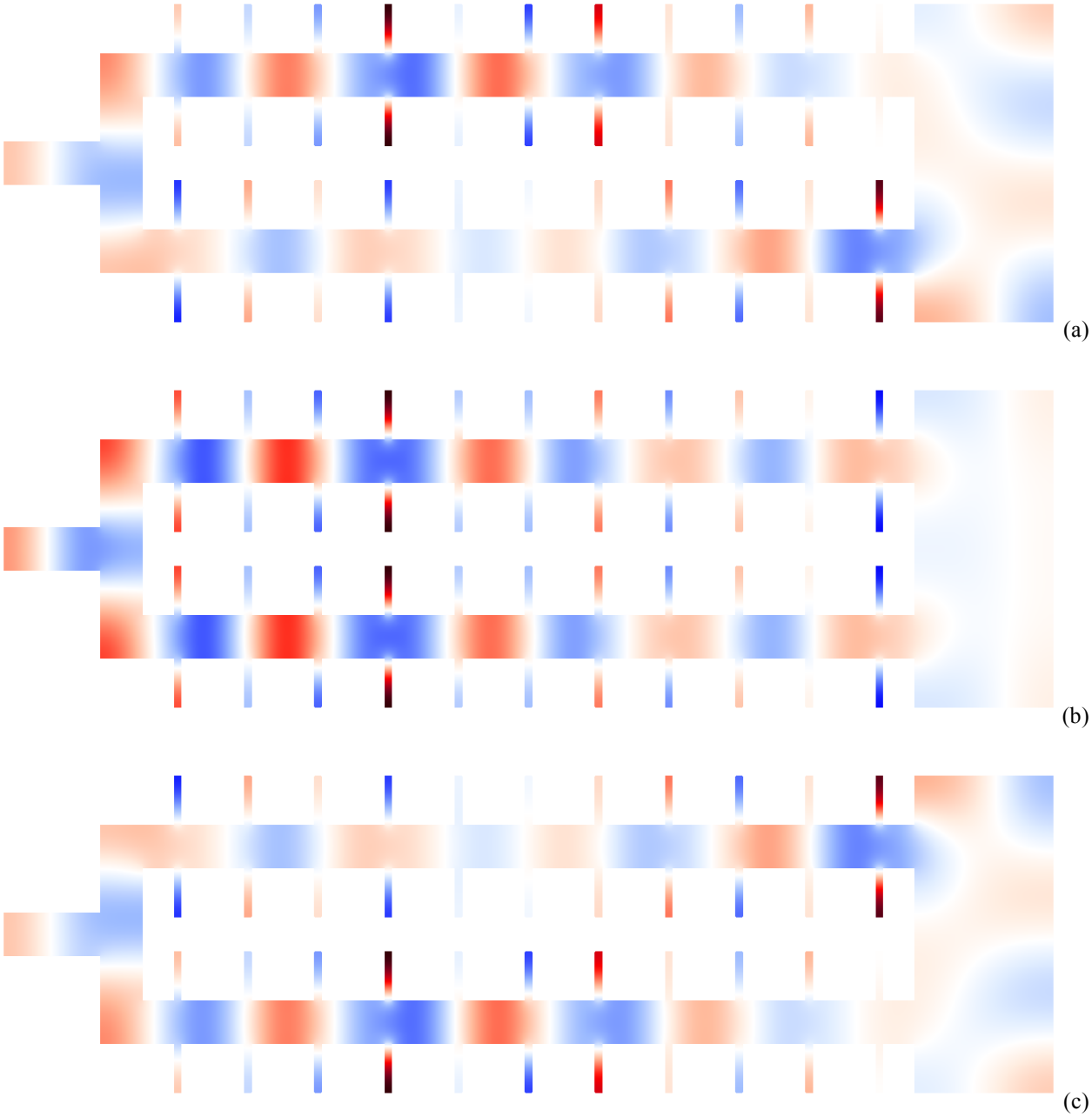

Figure 46 The *E-M* field distributions at (a) V_1 = 0 V; (b) V_1 = 1.5 V; and (c) V_1 = 3 V, with the original ADC structure dimensions and a narrow band input signal (center frequency f = 10THz, bandwidth 1.5 THz)

4.12 THz ADC comprising DC-SSPP MZI architecture: Waveguide-Cavity-Waveguide (WCW) resonance structure and localized phase modulation

In previous sections, the operation BW of the SSPP ADC is calculated by (**78**) with the assumption of each groove being driven individually. The need for the separated driven scheme is necessitated by the fact that the entire sidewall of each groove has to be applied with voltages.

In order to improve this design and enable universal driving of the structure, a smaller volume of the n-GaAs depletion region is required per-groove.

For this purpose, a modification to the design has been made with extra resonance introduced by the Waveguide-Cavity-Waveguide (WCW) structure. The WCW resonance structure has been discussed in detail in Chapter III, where it is used to enhance the sensitivity of the SSPP bio-sensor to the DNA morphology changes. Similarly, in the context of ADC, with the additional periodic blocks added to each arm of the MZI stage, we can successfully achieve larger deflection angle with the same voltage modulation mechanism. More importantly, we can take advantage of the enhanced responsivity of the modified structure to reduce the dimensions of the electrode, which will, in turn, help the speed of the entire device.

The modified MZI stage is sketched in Figure **47**:

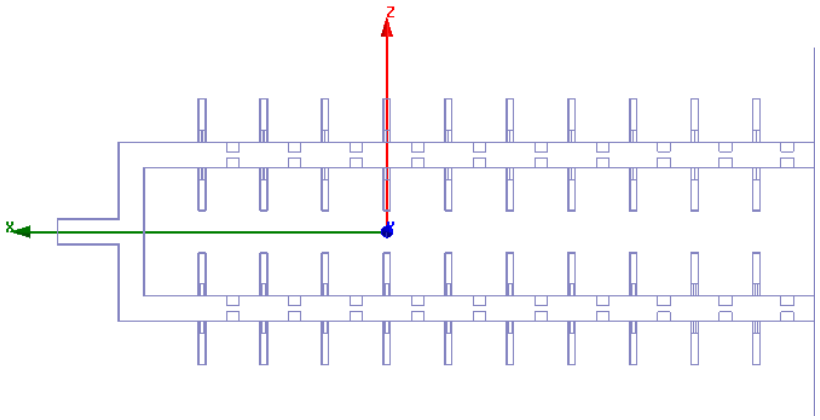

Figure 47 Illustration of the modified SSPP beam steering stage of the ADC design with WCW resonance structure

In the WCW architecture introduced in Chapter III, a single extra resonant cavity is formed by the addition of blocks only at a localized region. This will result in sharper peaks in transmission, as well as efficient modulation of such peaks in the frequency domain (Figure **18**). However, in ADC applications, a stable transmission magnitude in both arms of the MZI is required at all times. This requirement calls for the periodicity of the SSPP structure to be retained. As a result, the WCW additions are positioned repeatedly in the entire SSPP waveguide. The periodicity of such addition creates the extra resonance only in the signal phase of the THz carrier wave, which enables its phase modulation with much-enhanced efficiency.

For optimization of the structure design, HFSS simulations are performed with varying dimensions of the periodic blocks. With the WCW structure, it becomes unnecessary that the control electrode covers the entire groove area. Instead, it becomes only a fraction of the groove sidewall. One example output from this WCW modified ADC design is shown in Figure **48**. In this design, we can get the same 3-bit digitized output with the electrode size shrunk to 1/10 as before:

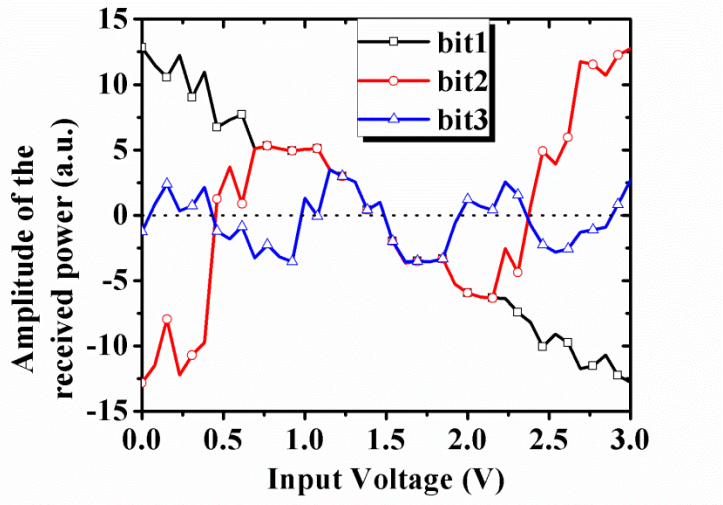

Figure 48 Bit readout from the WCW-enhanced ADC with 0 – 3 V voltage input with nonlinear detector arrays.

With the WCW-enhanced ADC design, we calculate the operating BW by assuming all electrodes are driven at the same time. Under this condition, by using the same theories in section **4.10** and applying the new electrode dimensions to (**78**), the RC time constant is calculated to be 2.2 ps. The RC time constant curve is included in Figure **49**:

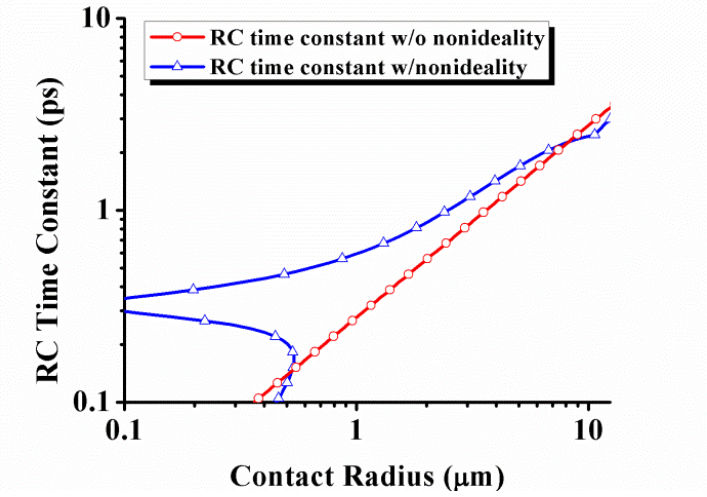

Figure 49 The RC time constant calculated both with and without the non-ideality factors (skin effect, carrier inertia and displacement current) as a function of the Schottky contact radius.

This time constant, when combined with the carrier transit time, results in an ADC operation speed of 47.1 GHz with the WCW-enhanced design.

In order to calculate the ENOB of the WCW-enhanced THz ADC design, the detector array readout with higher voltage resolution is given in Figure **50**. The quantization conversion relationship and noise function are depicted in (a) and (b), respectively, where their counterparts of ideal ADC designs are included as well for the purpose of comparison. It can be observed that the WCW ADC is still not ideal, which will give rise to a smaller ENOB than the 3-bit resolution it is designed for. Following the same routine as described in section **4.9**, the ENOB is calculated to be 2.67 bits. Compared with the original design, this ENOB deterioration from the nominal bit resolution is reasonably small. Similarly, by optimizing the mirror symmetry, linearity, and detector array designs, we can potentially make the WCW ADC to perform closer to ideal.

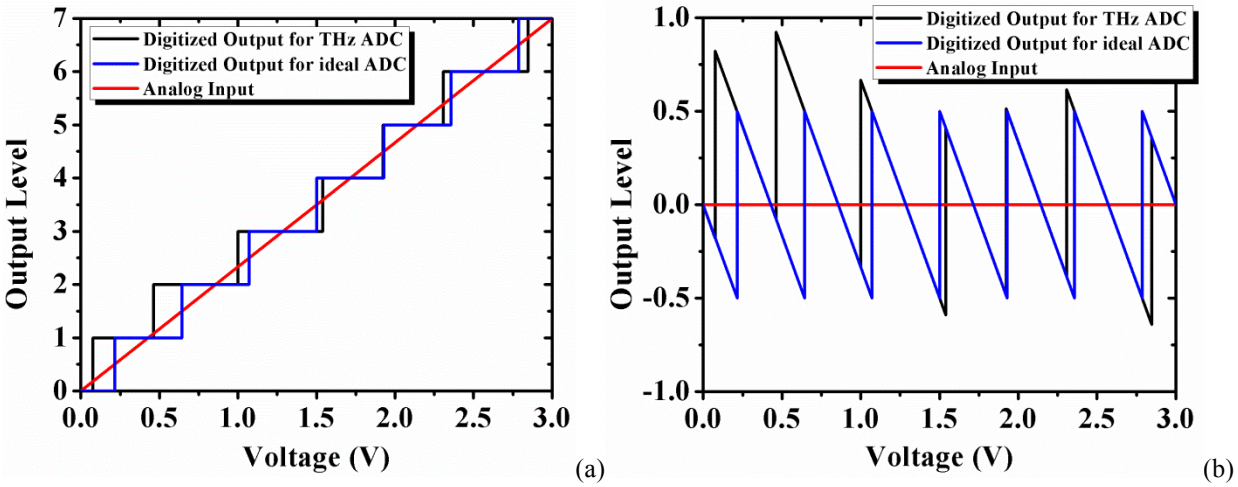

Figure 50 (a) Conversion relationship and (b) quantization error function of the DC-SSPP THz ADC in comparison with the ideal ADC

CHAPTER V THz Sources and Detectors: Technology and Compatibility Review with DC-SSPP Applications

5.1 Background

In Chapter IV, the high-speed ADC operation with THz carrier signal has been demonstrated with both theoretical analysis and rigorous full-field simulations. The device characteristics, including output linearity, operation bandwidth, effective bit depth and the full-scale field distribution, have been thoroughly demonstrated. The micro-scale ADC structure is designed to utilize THz signals to achieve speed and bandwidth performance superior to its electronic counterparts. Nevertheless, the difficulty in the generation and detection of THz signals remains a major challenge yet to be fully elaborated. Therefore, it is worth reviewing the state-of-the-art THz source and detector options in order to understand their applicability to the DC-SSPP architecture and device designs.

Unlike optical waves, the photon energy of THz radiation is on the order of ~meV. This minuscule energy per THz photon poses severe constraints on the design of sources and detectors at these frequencies. Currently, only free-electron lasers are proven to be capable of generating powerful and broadly tunable THz radiations [128]. However, the high cost and cumbersomeness of such sources indicate their applications to be usually confined to the explorative research areas such as condensed matter characterizations, ultrafast magnetization dynamics and charged particle manipulations, where high radiation energy is needed [129, 130, 131, 132, 133].

With the potential application of THz in imaging, chemical molecular sensing, and biomedical diagnosis, development of alternative THz generation and detection mechanisms began to attract significant attention since the 1990's. These studies have been focusing on designing THz emitters/receivers with broad tunability, output stability, and compactness, which are essential for small-scale applications that are more demanding on versatile output than absolute power and intensity. Unlike their predecessors, these devices take advantage of the interaction of laser

photons with the carrier and/or photon dynamics of the solid-state gain media. The relative high quantum efficiency, compatibility with the existing material and fabrication techniques as well as the ease of operation have made them the most successful THz solution to this date.

Among all demonstrated paths, nonlinear optical wave-mixing and semiconductor photoconductive effects are the two primary mechanisms that have been intensively investigated. While the first approach has severe limitations to be utilized for the application reported in previous chapters, it is still worth reviewing the progress therein. The second approach, on the other hand, is a monolithic solution taking advantage of the THz-solid state interaction and is one of the potential solutions compatible with the dimension of our application. In addition to these prevalent options, in recent years there are many other novel approaches in THz generation and detection being demonstrated. Among them are devices based on resonant tunneling diode (RTD), which demonstrated reasonable responsivity and even positive gain in THz regime, thanks to its unique negative differential conductance property. Exciting development due to the emergence of novel materials (such as graphene) are also reported and has opened other doors for integrated THz detection in micro- and even nano-scale. The great progress on this front over the past 2-3 years, which reported THz detection up to ~ 30 THz, are also reviewed here.

5.2 THz generation/detection by wave-mixing

Photonic generation of THz wave is based on both 2^{nd} order and 3^{rd} order nonlinearities, including but not limited to optical rectification (OR), optical parametric oscillation (OPO), second harmonic generation (SHG) and even four-wave mixing (FWM) processes. In this case, the THz emission follows the classic theory of nonlinear wave mixing and wavelength conversion. The frequency of the THz radiation is typically determined by the phase matching condition in the nonlinear optical crystals, and is usually tunable in the same manner as the pump wavelength or incident angle is adjusted.

Thanks to the variety of the photonic coherent sources that operate in the continuous wave and pulsed mode of various time scales, they are widely adopted as the driving sources for the THz generation and detection with the advantages of compactness and high efficiency. A typical Ti:Sapphire laser, for example, can output laser pulses at 800 nm wavelength with up to TW of

power in the time scale of *fs* [134]. This stable and strong pump signal has made the nonlinear wave-mixing in organic and inorganic crystals a practical path.

Due to the pulsed nature of the pump laser, the THz generation was first reported with the pulsed output. The THz radiation generated in this case is typically broadband, as the pump and idle signals are quasi-phase matched across the entire spectrum of the THz output. $LiNbO_3$, for example, has been exploited in multiple designs as the nonlinear optical crystal, and THz signal is generated by the 2nd order nonlinear effect with up to 1 MV/cm field intensity [135, 134, 136, 137]. Due to its small $\chi^{(2)}$ factor and relatively large absorption in the THz regime, the spectrum of $LiNbO_3$-based THz emitter is typically restricted to the sub-THz to THz range. Broader THz spectrum, especially beyond 5 THz, must be generated with less lossy materials with higher nonlinearity. In fact, with organic materials such as DAST, OH1 and DSTMS, broadband THz generation and detection has been reported with the spectrum extending up to 10 THz [135, 129, 134, 137].

Tunable, narrowband THz generation via nonlinear wave-mixing has also been intensively studied with inorganic crystals such as GaSe, GaP, and organic materials such as OH1 [135, 138, 139, 140]. Due to the narrowband requirement, the pump sources in these scenarios are typically Q-switched lasers such as Nd:YAG, Yb:YAG or Nd:YLF. As a prominent example, a 9.4 THz emitter design has been reported recently with dual-wavelength Q-switched laser pumping in OH1 [140]. Moreover, continuous wave THz emission with frequencies tunable between 1 and 4.5 THz has also been recently demonstrated with periodically poled lithium niobate (PPLN) pumped by a single-frequency Yb:YAG laser [141]. In the latter example, the bandwidth of the THz radiation is as low as 10 MHz. Compared with the broadband THz source, the THz spectrum reported herein is extremely narrow; It is even deemed negligible when compared with our transient simulation input in the previous section, where a bandwidth of 1.5 THz is assumed to achieve the satisfactory ADC beam steering effect.

It is worth noting that, although both broadband (pulsed) and narrow band (CW) THz generation have been intensively reported with various organic and inorganic materials, the bulkiness of the laser stimulating source, the phase matching optical system and the heterodyne detection mechanism together make this solution a remote choice for our ADC application. To solve the THz source and detector, integrated monolithic components are needed.

5.3 THz generation/detection by semiconductor photoconductive effect

Another major category of THz emitter and detector is based on photoconductive semiconductor gate architecture. In a photoconductive emitter, the impinging optical laser pulse, acting as a pump, will create electron-hole pairs in the semiconductor material. The subsequent relaxation of the electric current generated across a biased gate structure will generate a THz response. This mechanism is based on coherent photon-carrier interaction and is much more likely to realize resonant emission and detection of THz radiations (*i.e.* the direct energy transfer from photon oscillation to free carrier oscillation). This can be realized through the excitation of plasmon polariton mode that can exist in many electronic device designs.

At the beginning of the '90s with the pioneering theoretical work of Dyakonov and Shur, the possibility of generating THz emissions through the instability of plasmon waves in the field-effect transistor (FET) structure is proposed [8]. The inverse effect is predicted by the same authors, where the incident THz radiation can generate a 2-D plasmonic oscillation of the electron gas within the channel of an FET under certain conditions, and the resonant detection of such radiation can be realized [9]. The FET as seen by the incident THz wave can be described by the equivalent circuit model as shown in Figure 51. In order to realize resonant detection, the frequency of the incoming radiation and the electron momentum relaxation time needs to satisfy $\omega\tau < 1$. Under this condition, the inductance in Figure 51 plays a primordial role and plasmonic oscillation can be generated and transmitted through the channel the same way waves travel in an RLC transmission line. In this case, the FET can have selective absorption spectrum in THz, and the absorption peak is determined by the plasmonic mode resonance that can be supported in the channel region. Experimentally resonant detections have been demonstrated using GaAs HEMT for sub-THz signals, although they still suffer from low sensitivity and low signal-to-noise ratio (SNR) in room-temperature operation [142, 143].

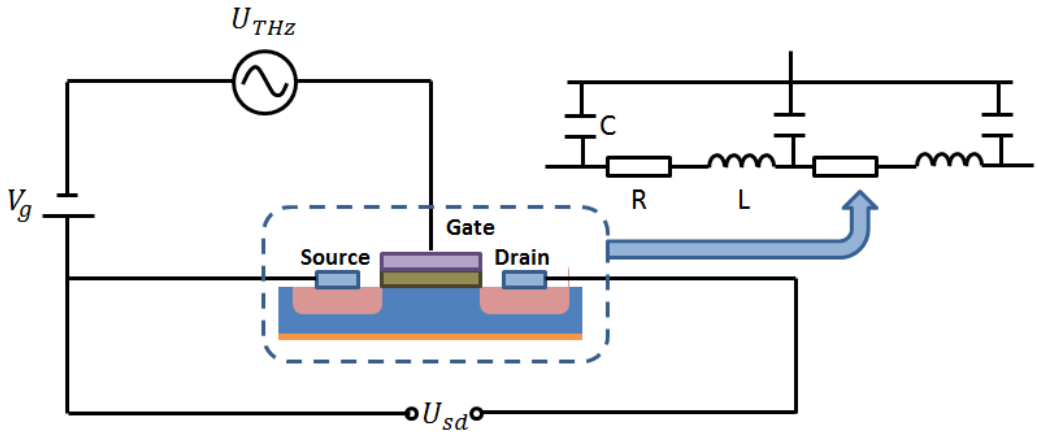

Figure 51 Equivalent circuit model of field-effect transistor (FET)

In the case where $\omega\tau < 1$, however, the incoming radiation is too fast for the channel free carriers to oscillate coherently, and plasmons cannot be generated. In the equivalent circuit model, this overdamping effect can be represented by the short-circuiting of the inductance element and therefore, the degeneration of the model to a simple RC configuration. From the physics point of view, the THz oscillation in this case modulates the density of the free carriers and their drifting velocity at the same time. This modulation gives rise to a broadband rectification of the signal, resulting in a DC source-to-drain voltage. The amplitude of this voltage is proportional to the intensity of the incoming THz wave, in the form of:

$$\Delta u_{sd} = \frac{U_{THz}^2}{4}\frac{1}{\sigma(U_0)}\frac{d\sigma(V_G)}{dV_G}\bigg|_{V_G=U_0} \tag{80}$$

In the above equation, $u_{sd}$is the DC source-to-drain voltage, U_{THz} is the amplitude of the oscillating gate voltage generated by the THz radiation, $\sigma(V_G)$ is the conductivity of the free carriers as a function of gate bias, and U_0 is the DC bias value in use. This phenomenon has encouraged numerous effort of using MOSFET and HEMT to detect broadband THz radiations. Due to the less stringent requirement on the free carrier mobility, non-resonant detection of sub-THz as well as THz radiations have been realized in room-temperature using both Si and III-V semiconductor-based, and even graphene field-effect transistors [144, 145, 146, 147]. Reasonable sensitivity and noise-equivalent power (NEP) are reported in those works.

The detection of the THz radiation requires effective coupling of the incoming signal to the gate electrode, as well as the asymmetric design of the source and drain contacts. The coupling

mechanisms that have been reported range from bonding wires to patched electrodes and logarithmic periodic antennas [148, 149, 150, 151, 152]. The asymmetry can be provided by the difference in source and drain contact material, electrode geometry, as well as voltage bias applied across the FET nano-structure.

Given the THz emission and detection is enabled by the modulation of FET channel conductivity, the THz signal needs to be coupled through the gate contact. The top gate capacitance coupling efficiency, as a result, will limit the performance of such devices. For this reason, although reasonably high sensitivity has been demonstrated by multiple designs, up to this date there is rarely any report on the photoconductive detection of signals above 1 THz frequency. In addition, the need for gating structures on nano-scale also complicates the architecture of those devices considerably. This not only complexes the manufacturing process by the need of advanced nanolithography steps but also tends to introduce parasitic effects that are harmful to the device sensitivity.

5.4 THz generation/detection by resonant tunneling diode

A resonant tunneling diode (RTD) is a two-port device consisting of alternating thin semiconductor materials layered in the form of a 1-dimensional super-lattice. First proposed 40 years ago by pioneers such as Tsu and Esaki, the RTD features unique I-V characteristics due to the tunneling-based carrier transportation through one or multiple quantum wells (QW) in its structure [153]. With constant research attention, the potential of RTD in the regime of high-speed integrated electronics is gradually revealed [154]. Thanks to the rapid progress in semiconductor science and nano-fabrication technique, the operational bandwidth of the RTD device has been demonstrated to grow steadily, quickly approaching, and in many cases, successfully entering the THz regime [155, 156, 157].

The fundamental operation of an RTD is primarily governed by its QW layers. With the thicknesses of the semiconductor super-lattice comparable to the carrier wavelength in these devices, quantum phenomena including discrete carrier energy level and resonant tunneling are bound to take place. When biased, charged carriers can propagate through the RTD structure via quantum tunneling effect, creating a finite current across the channel. The magnitude of this

current is dependent on the tunneling efficiency, which in turn is determined by the QW energy level in comparison with the carrier voltage bias.

The carrier transportation mechanism in an RTD is most easily explained when there is only a single QW present in the structure [154]. In this simplistic case, the resonant tunneling only takes place at the interfaces between the 3D region (e.g. emitter/collector) and the effectively 2D QW region to generate current. In this process, the energy levels of both regions are expressed by the following formulas:

$$E_{3D} = E_C + \frac{\hbar^2 k_x^2}{2m^*} + \frac{\hbar^2 k_{||}^2}{2m^*} \tag{81}$$

$$E_{2D} = E_n + \frac{\hbar^2 k_{||}^2}{2m^*} \tag{82}$$

In (81) and (82), E_{3D} represents the bottom of the carrier conduction band in the 3D region and is dependent on the bias voltage. E_{2D}, on the other hand, represents the quantized energy level within the 2D QW region. The boundary conditions are established such that both energy and transverse momentum are conserved across different regions. With these conditions, tunneling event is only possible for carriers with longitudinal momentum as dictated by the following formula:

$$k_0^2 = 2m^*(E_n - E_c)/\hbar^2 \tag{83}$$

According to Fermi-Dirac distribution, the maximum carrier density that satisfies the above condition is achieved when $k_0 = 0$. This requirement calls for $E_n = E_c$, dictating the bias voltage where maximum current is obtained. Once the bias voltage further increases, the required longitudinal momentum for tunneling carriers would become imaginary, causing a drastic drop in the tunneling efficiency. This phenomenon is reflected by the sharp decrease of current response, creating the unique I-V characteristics commonly known as the negative differential conductance (NDC) effect. In fact, this phenomenon is retained when multiple QW exists in the RTD structure. A more comprehensive mathematical interpretation of the carrier behavior in this case was presented in Tsu and Esaki's original work based on Schrodinger's equation and transfer matrix method, where the peculiar non-monotonic I-V characteristics were also predicted [153].

RTDs are operating specifically in the NDC region to sustain oscillations and achieve responsivity at high frequencies. As the carrier transport through RTD barriers is taking place via fast capture/escape processes to/from the resonant states in the QW region, the operation speed limit of this structure is in general dictated by the carrier tunneling lifetime and coupling circuit parasitics. In the past few years, multiple research works have adopted careful choice of materials and utterly thin barrier layers to reduce the carrier relaxation time constant in RTD [158, 159, 160, 161, 162]. Equivalent circuit models are also established and verified with the aim of achieving optimized balance between the coupling efficiency and the effective circuit reactance [156, 163]. As a result, many examples of RTD emitter/detector with reasonable responsivity near or beyond 1 THz are successfully demonstrated.

The NDC of the RTD is in theory a gain mechanism. This unequaled property can be utilized when RTD is integrated with other THz generation and detection structures to achieve superior performance. For example, the limitation of the photoconductive detectors, as described in (2), generally comes from the gate leakage current [164, 165]. This parasitic effect is a result of the positive gate conductance and is responsible for the attenuation of the plasma wave within the photoconductive channel. The negative conductance of the RTD, in this case, could be utilized to balance out the plasma damping effect, and when tuned properly, to provide effective gains for better device responsivity [166, 167]. A great example of this application was presented by Berardi et al, where the gate structure of a traditional photoconductive THz detector based on high electron mobility transistor (HEMT) is replaced by the RTD stack [168]. The interplay between the gate NDC and the plasma excitation within the HEMT channel has enabled a positive power gain. A follow-up work from the same research group has even predicted the integration of the THz coupling mechanism with the RTD stack-up, where the effective coupling is achieved via the grating-gate structure [169]. The NDC-induced gain along with the elimination of the traditional coupling antenna has predicted considerable gain up to 2THz.

In general, RTD is a powerful structure in the THz frequency range, and constant research works are still ongoing to increase the operation bandwidth of this category of emitter/detector. With the carrier relaxation time in the QW layers playing the primordial role, the current speed limit of RTD primarily comes from the layer thickness and band-gap material selections. In the near future, whether or not RTD devices can be applied to the frequency range of ~ 10 THz is yet

to be demonstrated. Nonetheless, this category of devices still represents a promising solution to the generation and detection of THz signals, especially with the possibility of achieving positive gains. In addition, the enormous research effort in next-gen fast electronics involving RTD also makes the THz component in this category a natural option when it comes to system integration.

5.5 THz detection by ballistic carrier transmission and geometric antenna

Graphene has the unique advantage of having the valence and conductance band in contact at the Dirac point, providing gapless band structure. This property has made graphene an ideal choice to detecting longer wavelength radiations potentially from Far-IR to THz [170]. In addition, graphene has demonstrated high electron mobility and long carrier mean-free path, especially when it is encapsulated with proper substrate lattices [171, 172]. These properties provide an opportunity to realize THz detection via direct coupling and geometry-induced signal rectification.

Tailoring the shape of the semiconductor channels has been reported on rectification and self-switching devices in sub-THz and THz devices by a handful of research groups in the past decade [173, 174, 175, 176]. In these reports, the channels were designed with a biased geometry, such as a triangle or a trapezoidal shape. The carrier transportation within the channel was shown to have an intrinsically favorable direction, which is defined by the statistical difference in the blocked, reflected and channeled carrier quantities (see Figure 52). This, in turn, will result in a rectification of the signal, similar to the signal rectification in a diode.

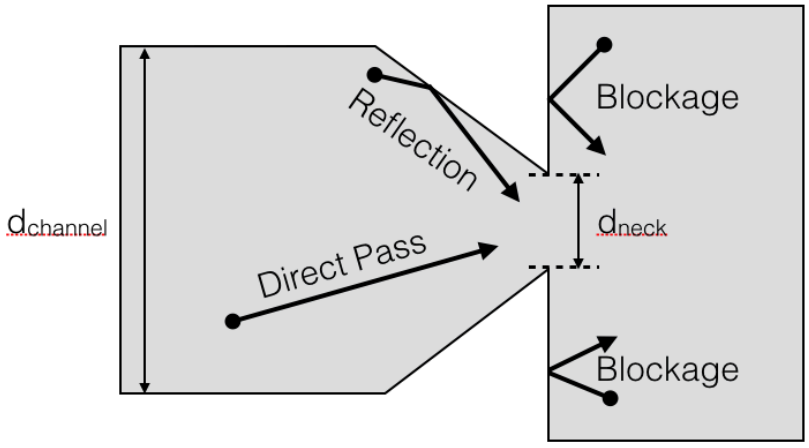

Figure 52 Illustration of a geometrically asymmetric channel and ballistic carrier transportation

The efficiency of the signal rectification effect depends on the nature of carrier transportation, where frequent carrier collision is clearly undesirable. It is also greatly affected by the incident signal coupling efficiency, which is determined by the dielectric property of the combined semiconductor and antenna design. These are the main reasons for the unsatisfactory performance at early days of these devices, which are made of conventional semiconductor materials. The true breakthrough, graciously, came with the graphene material where ballistic transport of the carriers can be attained at a reasonably large scale (several hundred nm to 1 μm) at room temperature. The ballistic carrier movement can greatly enhance the extinction ratio of the geometric-asymmetric device, providing an excellent rectifying effect. The conductivity of graphene, on the other hand, consists of both intraband and interband components [177]. In the range of 1 - 30 THz, the interband conductivity dominates, which is described by the equation below:

$$\sigma_{inter} = -i\left(\frac{e^2}{4\pi\hbar}\right) ln\left(\frac{2|\mu_c| - \hbar(\omega - i2\Gamma)}{2|\mu_c| + \hbar(\omega - i2\Gamma)}\right) \tag{84}$$

In (84), the real conductivity component is much smaller than its imaginary counterpart, making graphene in this frequency range a highly reactive (predominately inductive) surface. This is ideal to reduce the coupling loss due to side lobes and reflection. In addition, as the conductivity is a function of the bias voltage, it opens the door to achieve impedance matching to a broadband of signals via bias modulation, which makes this device highly versatile. For these reasons, grapheme-based geometric rectifiers have attracted enormous research attention. The exciting development therein has been reported by several studies in the last few years for it to become a promising THz detector solution [178, 179, 180].

In the report by Dragoman et al, for example, a THz detector has been simulated and manufactured based on the asymmetric channel design [178]. Gold antennae were deposited on top of a graphene monolayer to provide THz signal coupling. Simulation has demonstrated the versatility of this antenna design, where various geometries with dimensions in the scale of tens of μm can be applied to effectively couple THz radiation at 10 THz. Its coupling effectiveness has been demonstrated by the radiation pattern, which showed a complete elimination of side lobes and high front-to-back ratio. With varying bias voltage, the device showed a rectifying effect as predicted. This effect will be saturated when the gate voltage is too high, which comes

from the non-ballistic movement of the carriers when its concentration and energy increases. In this report, the THz rectification detector design has achieved reasonably high responsivity with 10 THz signals. It is comparable to that of the Schottky diodes detectors, which is only applicable so far to 1 THz frequency. A more detailed theoretical analysis of this THz detector design is reported by the same author, which extended the concept to other possibilities such as quantum confined architectures [179].

Another example by Zhu et al also reported a similar concept, which they gave the design the nomenclature of "geometric diode" [180]. This design features a trapezoidal graphene sheet defined to be nm-scale. Both Monte-Carlo simulation and actual measurement has demonstrated the efficacy of this THz detector design, which achieved a detectivity and noise level almost equivalent to other THz detectors, including the graphene photoconductive detector described in the previous section (albeit at a different frequency). The most significant breakthrough in this report is that this is the first time that a detection of radiations up to 28 THz (CO_2 laser @ 10.6 μm) is reported with direct photon coupling into a nanometer structure. This result has made the detecting spectral range of such receiver to become by far the most extensive when compared with conventional Far-IR and THz detectors.

Given the μm-scale dimensions of the THz ADC architecture and the operating wavelength at near or beyond 10 THz, the graphene THz detector with geometry-induced rectification is so far the most promising solution. Certainly, there are yet manufacturing details that still need to be carefully developed. However, the great properties of this design, such as high detectability, high achievable frame rate, room temperature operation and integrated packaging, has proved this design to be an exciting opportunity to be implemented to the THz ADC micro-structure we presented in this chapter.

5.6 Summary

THz generation and detection are still in their infancy. Mostly based on III-V semiconductors, the devices based on direct photon emission/absorption rely on photocurrent from the inter-subband transition of electrons [135, 181, 182, 183]. As a result of the insignificant photon energy of THz radiation, the difficulty in distinguishing it from thermally generated current usually dictates cryogenic cooling. This has so far been the major drawback of this category of

THz emitter and detectors. Traditional thermal-based THz detectors (such as Golay cells, pyroelectric elements, and hot electron bolometers), on the other hand, can operate at room temperature. However, those detectors are in general quite slow, and can only be used in applications where a low frame rate is sufficient [184].

In this section, several THz generation and detection mechanisms are reviewed, and their applicability to the THz ADC architecture is discussed. Wave-mixing method is the most prevalently used in THz community nowadays, with wide application in THz Time Domain Spectroscopy (THz-TDS). However, its bulkiness has made it a remote option for the architecture we reported herein. The FET-based photoconductive THz emitter/detector is a micro-scale proven solution for years. Its performance can be enhanced with material options such as graphene, but the limitation so far comes from the gate coupling requirement, which is still detrimental to the extension of such device towards higher frequencies. Facing these challenges, the geometric diode concept is so far the most promising solution with its device size, operating frequency, and versatility all in line with what our application calls for.

It is worth noting that this chapter is dedicated to the review and discussion of THz sources and detectors, as they are equally indispensable for the complete SSPP ADC design. There is vast progress being made on the THz emitter/detector and they may not be fully covered by this review here. Please also be understanding that the detailed modeling, design, and characterization of THz generation and detection is beyond the scope of this thesis work and should be discussed elsewhere.

CHAPTER VI Future Work: DC-SSPP Applications in THz Boolean Operation with 2-Dimensional Directed-Logic Networks

6.1 Background

As reviewed in Chapter V, the dilemma between the positive phenomenology of THz radiations and the difficulty in their generation and detection is being continuously mitigated by the advent of novel emitter and detector designs. These works have triggered fast progress in the research field of THz electromagnetics and components, which has long been deemed as missing links between their microwave and optics counterparts. With discoveries of new materials and implementation of novel device nanostructures, recent works have already demonstrated designs of high electron mobility transistors (HEMT) with near THz operation speed [185, 186, 187]. Resonant plasmonic detection of THz radiation has also been proposed and verified by numerous groups, where the photon stream can excite carrier oscillation at the same frequency [142, 188, 143]. With these significant progresses, we foresee a future of the Beyond-Moore's Law era of the integrated electronic circuit, where higher operation speed of the VLSI can be realized with the integration of THz components into the state-of-the-art CMOS technologies.

In fact, we designed THz ADC as one important building block of the THz circuitries, as already described in detail in Chapter IV. In that design, The SSPP structure acts as an effective interface through which the electronic input can be used as control signals, while the information is carried by the THz frequency. The DC-SSPP structure enables THz signal propagation in slow-wave modes. These designer modes indicate the possibility of controlling the wave transmission via external stimuli. Similar ideas can be employed in the design of other THz circuitry components. Most prominently, THz Boolean logic component designs are studied in this chapter and realized as the fundamental constituent of the future THz digital circuits.

6.2 Directed Logic: Overview and comparison

In electronic circuits, Boolean logic is realized by cascading a network of bistable elements known as the logic gates. Electronic Boolean gates typically feature one or more logic inputs and their outputs are determined by the specific Boolean operations. Such outputs are propagated to the following logic stages where they act as inputs again. Complex Boolean functions are realized by serially connecting these gates in a predetermined manner.

Despite its predominant usage, the gate logic has begun to face significant challenges with the growing demand for lower power and higher speed circuit designs. Contemporary electronic Boolean gates comprise primarily semiconductor transistors. The logic circuit, as a result, consists of clusters of transistors connected in a sequential manner. Although the final logic output is the only output of significance, the serial cascading of the Boolean gates requires all intermediate results to be calculated, cached and propagated, producing power consumption and latency associated with each individual step. Therefore, the overall power penalty and delay of the Boolean circuit grows in a cumulative manner with the scale of the circuit design.

Concurrently, photonic logic has attracted growing attentions as a result of the signal's large bandwidth and high propagation speed (close to or comparable with the speed of light), which can potentially bring about faster logic operations. Through the years, photonic logic has been reported by numerous works, where optical waves are used to carry the Boolean information in replacement of the electronic signals. The Boolean state is coded using the amplitude, phase or wavelength of the optical signals, and its control is realized by both linear and nonlinear photonic effects [189, 190, 191, 192, 193, 194]. Despite the variety of realizations, these technologies still relied on the gate logic concept as stated above. The need for serial connections to realize complex logic remains an obstacle to overcome before real breakthrough in the operation speed of large-scale digital circuit can be achieved.

In light of this problem, a complete new strategy of realizing complex logic functions needs to be employed. This new mechanism needs to take advantage of the attributes of the photonic signal, which include the broad bandwidth, fast propagation and the capability to achieve state change instantaneously without expenditure of energy. At the same time, it needs to retain the compatibility to the electronics, avoiding common issues in the all-optical systems such as dimension mismatch, inflexibility, susceptibility to mechanical and environmental variations, and the presence of bulky optical elements (i.e., mirrors, beam splitters, lenses, etc.). J. Hardy

and J. Shamir has first proposed and conceptually analyzed the idea of directed logic in their pioneering work to address these issues [195]. In directed logic, photonic signals carry the logic information, and electronic signals act as the control, hence are the Boolean inputs. Unlike the gate logic, the entire Boolean operation is not realized by cascading the inputs and outputs one stage after another. Instead, the only signal that propagates between elements of the network is the information-carrying photonic signal. A block diagram of the directed logic network is shown in Figure 53. A comparison between the directed logic and the gate logic in realizing an XOR operation is shown in the figure to better illustrate the difference between the two approaches.

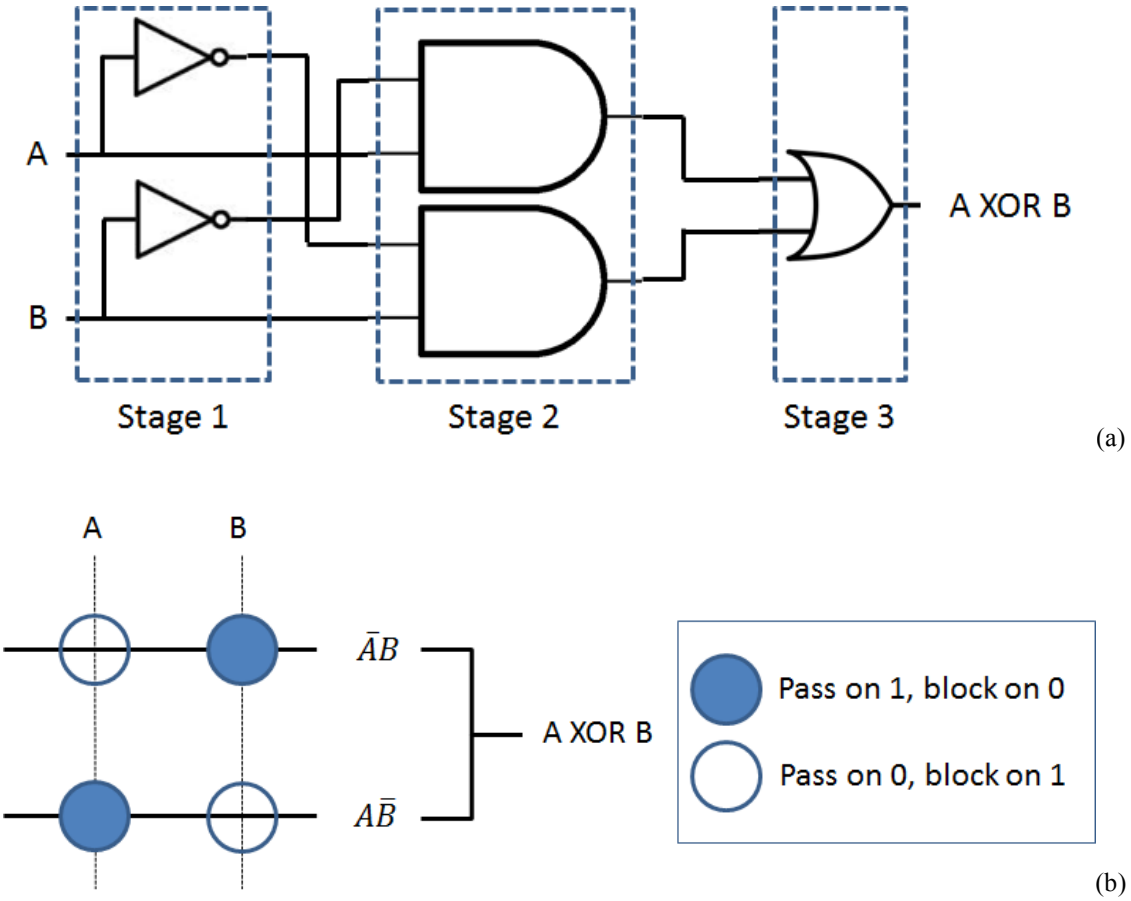

Figure 53 Realization of the XOR logic using (a) gate logic and (b) directed logic. In gate logic, the output are calculated in multiple stages, while in directed logic all inputs are applied simultaneously

The advantage of directed logic in realizing high-speed photonic Boolean operation is obvious. Regardless of the nature of the circuit, the time needed for the logic operation consists of the time for the logic-bearing signal to traverse the entire Boolean network, and the time for the

individual logic gate to switch its output state upon the input change. Therefore, the latency of the entire circuit is the combination of the above-mentioned delays, known as the 'path delay' and the 'state delay', respectively [195]. In gate logic, as a result of the serial connections of the Boolean gates, the gate of the later stage cannot generate meaningful result unless the outputs from all of its previous stages have stabilized. This phenomenon dictates both the 'path delay' and the 'state delay' to be cumulative. To reduce the delay, not only the gate size and the individual gate switching speed need to be optimized, but efforts also need to be made to reduce the sheer number of gates to the minimum. The latter is rather difficult, if not impossible, as the Boolean logic in modern circuit designs is extremely complicated.

The situation is quite different in directed logic. In this approach, the Boolean inputs need not to be propagated through the circuit. Instead, they are applied simultaneously, generating state change at the same time. The 'state delay' is not cumulative any more, and faster operation can be realized even with slower switching speed of individual Boolean elements. This speed advantage is further assisted by the fact that photons carry the Boolean state in directed logic, and they travel at considerably higher speed than electrons in conventional wires. The 'path delay' can therefore be reduced significantly as well, even considering the relatively large dimensions of the photonic switches. This obvious advantage indicates the potential of realizing high-speed operation of logic circuits that are independent of their scales.

As a result, research activities flourished following the work by J. Hardy and J. Shamir. Numerous realizations of the directed logic have been reported, where the Boolean information has been coded in different ways including amplitude, phase and polarization of the photonic signal [196, 197, 198, 199, 200, 201]. Due to the common issues faced by optical-assisted circuits as mentioned in Chapter IV, we foresee the implementation of the directed logic in THz frequencies as the next reasonable step to take in designing high-speed digital circuits. Unlike optical frequencies, the THz signals are most effectively transmitted and modulated using sub-wavelength surface-mode architectures. The DC-SSPP waveguide can be readily applied to the construction of THz directed logic elements, when proper modification to the geometry of the structure is made.

6.3 DC-SSPP THz directed logic: Theoretical analysis

The key elements in the directed logic design will perform one of the following functions:

1. *Pass-block* function: let pass the THz signal when the Boolean input is 0; block the signal when the input is 1
2. *Block-pass* function: block the THz signal when the Boolean input is 0; let pass the signal when the input is 1
3. *Pass-pass* function: let pass the THz signal regardless of the Boolean input

A complete Boolean directed logic fabric is realized when these three elements are connected in a 2-dimensional network. One example of this 2-D network is already shown in Figure 53, where the combination of *pass-block* and *block-pass* elements can act as an XOR gate. In fact, the rule of sum-of-product (SOP) guarantees the generation of arbitrary Boolean functions by using this type of logic network.

In order to realize the *pass-block*, *block-pass*, and *pass-pass* functions, we design the structure based on the DC-SSPP waveguide, with the modification of a narrowed waist in the center. As discussed in detail in Chapter I, the DC-SSPP waveguide features discrete band structure, where the bandgap between the transmission windows prevents the propagation of the THz signal. Using the theory of effective media, such inhibition of transmission can be represented by the imaginary phase velocity of the wave, as calculated from the effective permittivity and permeability of the structure:

$$v = \frac{c}{\sqrt{\varepsilon_{eff}\mu_{eff}}} \tag{85}$$

A narrowed-down section of the waveguide, on the other hand, creates an elevated cut-off frequency. Below the cut-off frequency, the THz signal is also prevented from the transmission, resulting in another imaginary phase velocity which can be represented by (85) as well. These two stop bands for THz transmission are shown in Figure 54, along with the curves of the effective permittivity and permeability of two different structures. The unmodified DC-SSPP waveguide (left-hand side in Figure 54) has dimensions of d = 100 μm, a/d = 0.1, h/d = 0.8, t/d = 0.3, and W/d = 3, and the non-corrugated waveguide is modified with a narrowed waist with W'/d = 1.5 (right-hand side in Figure 54). In both structures, bandgaps exist in the transmission spectrum and their associations with the imaginary wave velocities (opposite signs of the ε_{eff} and μ_{eff}) are clearly observed.

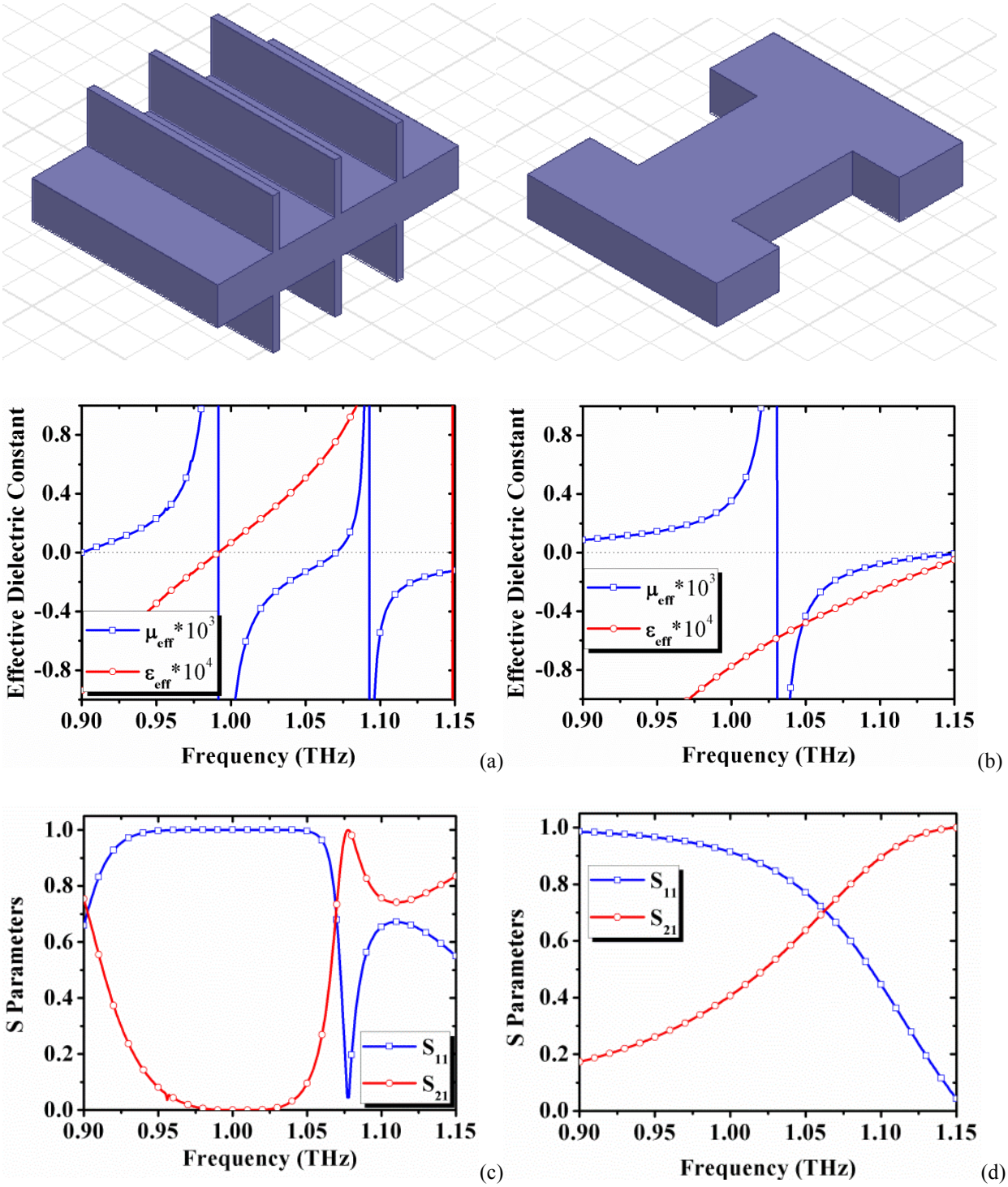

Figure 54 Effective permittivity and permeability, andS-parameters for: (a) and (c) the unmodified DC-SSPP structure, and (b) and (d) the non-corrugated waveguide with narrowed waist

From Figure 54, one may notice that the bandgap regions of the two structures overlap in the frequency range from f = 0.9 THz to f = 1.03 THz. At these frequencies, THz signals cannot

propagate through either structure, as the DC-SSPP structure is at resonance and the narrowed smooth waveguide is below its cut-off frequency. However, if we merge the two structures into one, the combination of the two stop bands can create a zone where the phase velocity of the THz signal becomes real again. In other words, by inserting a carefully designed narrow 'waist' into the conventional DC-SSPP waveguide such that the new cut-off frequency coincides with the first SSPP stop band, a new pass band will be created in the otherwise bandgap region of the unmodified DC-SSPP waveguide. Such phenomenon is shown in Figure 55. The addition of the narrow waist results in modifications to the effective dielectric properties, notably the effective permittivity. An extra transmission band is observed as a result, featuring a sharp peak which is quite desirable in applying this structure in frequency-selective applications.

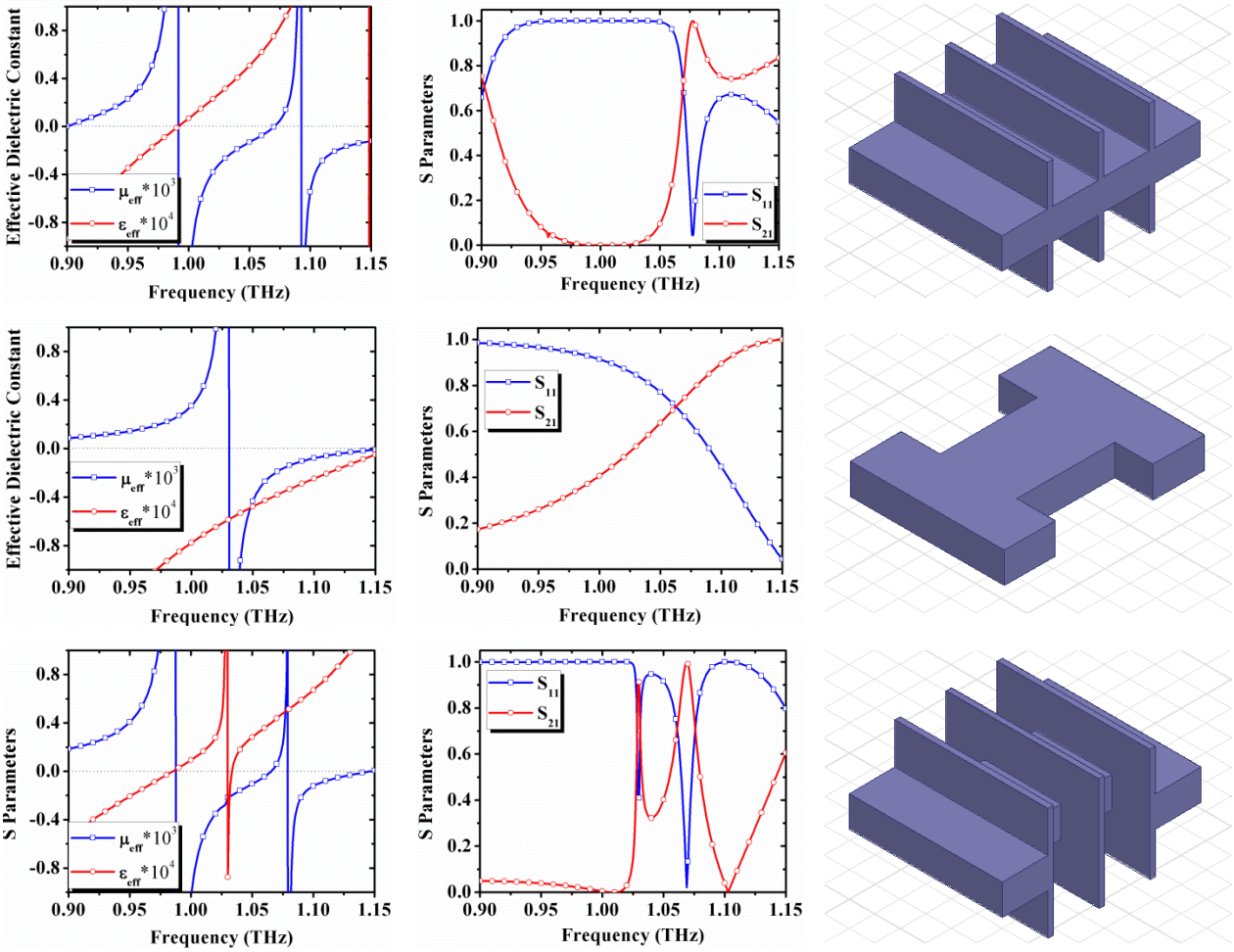

Figure 55 From top to down: effective dielectric properties andS-parameters of the unmodified DC-SSPP structure, the non-corrugated waveguide with narrowed waist, and the DC-SSPP structure with narrowed waist

The modified transmission band in the narrow waist DC-SSPP design can be effectively modulated by changing the material properties. The transmission curves with different refractive index applied to the center groove are illustrated in Figure 56, along with the *E*-field distributions in the structure at both the peak frequencies. The original transmission peak of the DC-SSPP is effectively shifted by the changing dielectric properties. For this transmission window, the field concentrates in the center groove, resulting in enhanced interaction with the material therein. It is essentially the same phenomenon which we observed and used to our advantage to build various components in previous chapters. The newly created narrow transmission peak, on the other hand, is not affected by the center groove modulation. It is explained by the zero field concentration in the center groove region, which indicates the independence of this mode to the material property change therein.

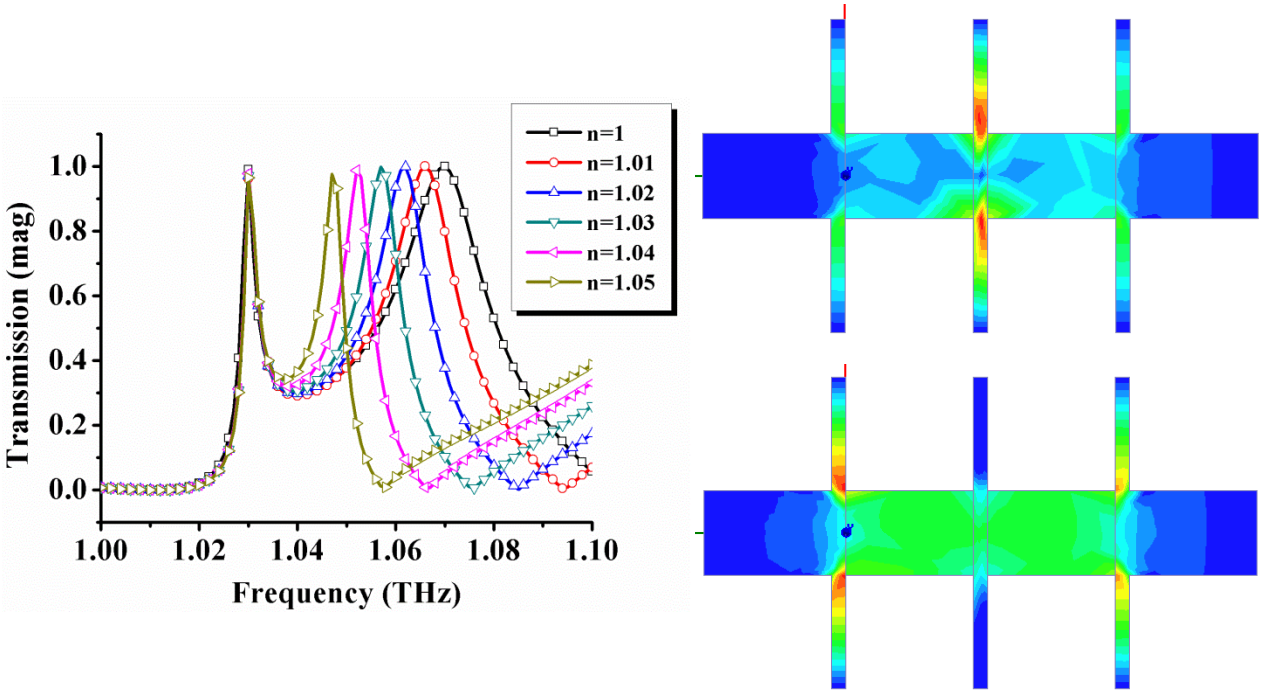

Figure 56 Transmission curves of the DC-SSPP structure with narrowed waist with different materials in the center groove. The *E*-field distribution for the two transmission peaks in given on the right, with the top one corresponding to the conventional SSPP transmission window and the bottom one representing the newly created peak

In the context of Boolean directed logic elements, this transmission spectrum is quite desirable. While the original DC-SSPP peak can be used in realizing the *pass-block* and *block-pass* elements, the fixed peak generated by the narrow waist is the perfect feature needed for building the *pass-pass* element. In Figure 56, the refractive index change is applied to the entire center

groove of the structure to induce the change in the transmission spectrum. In reality, the control of refractive index in the directed logic element can be achieved in multiple ways. We design the THz Boolean logic elements based on this concept via different modulation mechanism and will discuss them in detail in the sections to follow.

6.4 DC-SSPP THz directed logic elements in bio-computing

So far, bio-sensing has mostly been developed with the specificity of bio-molecular substances and reactions, and are largely restricted to small scale (so-called "point-sensing"). New techniques are fast emerging to realize parallel bio-sensing with ever-increasing efficiency and throughput, expanding the practicality of this technology in one dimension. In the other dimension, however, sequential pipelining of the acquired bio-molecular information remains an enormous challenge. Largely relying on the continuous "propagation" of certain bio-information through a network of logic nodes, the science of bio-informatics and bio-computing have just begun to gather attentions in the recent years. Despite numerous reports and experiment demonstrations, the progress in these domains to-date still relies heavily on the chemical reaction to perform logic operations and the electrochemical transducers for data interpretation.

On this front, numerous authors have given several examples in their excellent review paper, where enzymatic reactions were shown to form the backbone of various bio-molecular logic gates [202, 203]. For instance, a system comprised of glucose oxidase and catalase is reported to mimic a single-stage Boolean operation. In such system, glucose and H_2O_2 served as the logic input variables. Gluconic acid is formed as a product of the bio-catalytic oxidation of glucose and is detected in an optical manner. As the gluconic acid is only produced in the presence of both input reactants, an effective AND operation is realized. Another example also used oxidation of organic compounds as the controlled chemical reaction, while such reaction is detected by sensing the pH of the resulting acidic product. This system is composed of ethyl butyrate and glucose, while two catalysts of esterase and glucose oxidase act as inputs. Each enzyme would react separately with its own substrate upon addition, and the products of the reactions are both acidic (ethyl butyrate will be oxidized to butyric acid and glucose to gluconic acid). As a result, the output resembles that of the Boolean OR operation.

Numerous efforts have been subsequently reported to expand bio-molecular logic gate to realize more complex Boolean operations. For example, a multi-gate processing enzyme logic

system is reported in the same review paper by complicated reaction sequence involving three catalysts (alcohol dehydrogenase, glucose dehydrogenase, and glucose oxidase) and four input chemical reactants (NADH, acetaldehyde, glucose, and O_2). The concatenation of chemical reactions dictates the resemblance of this system to one unique Boolean logic chain as illustrated by Figure **57**. However, regardless of the logic function to be realized, these cascading efforts still rely on mechanisms that are reactant-specific. As a result, it is admittedly difficult, if not impossible, to realize scalable information-processing networks by using the bio-computing schemes as reported above.

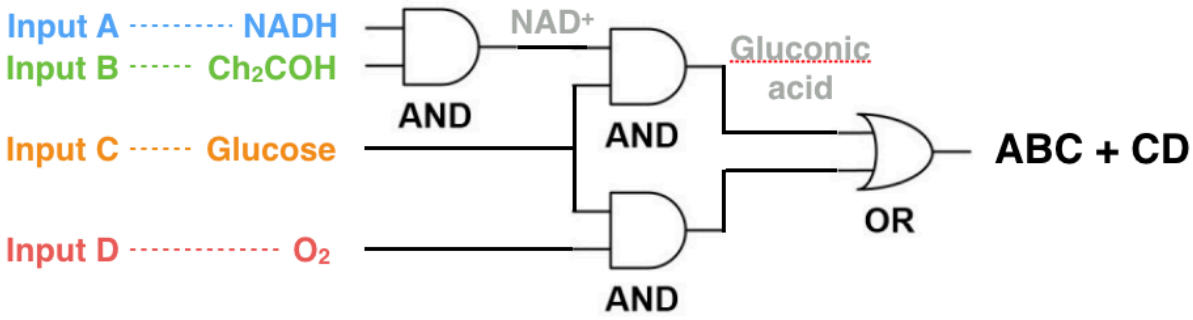

Figure 57 Example of Boolean operation enabled by concatenated reactant-specific bio-chemical reaction

Facing this fundamental difficulty, we foresee to utilize THz signal as the information-carrying medium and to implement the DC-SSPP directed logic element as the fundamental building block for an effective, cascadable bio-computing architecture. In this solution, chosen biological assays, serving as the Boolean inputs, can be applied simultaneously to the logic network. Subsequently, instead of interpreting reactant-specific bio-chemical signals as the logic output, universal THz signal can be cascaded through multiple stages in order to realize arbitrary Boolean functions. As an example, DNA molecules are known to change their dielectric constant with the change in the binding state. Therefore, the highly concentrated, slow-wave THz mode of the DC-SSPP architectures guarantees the effective change of its transmission band gap structure in a similar way as Figure **56** has predicted.

To the first order of approximation, the denatured and the hybridized DNA molecules have the refractive index of $n_1 = 1.05$ and $n_2 = 1.15$, respectively. The directed logic element structure is sketched in Figure 58. It has the dimensions of d = 100 μm, a/d = 0.1, h/d = 0.8, t/d = 0.3, and

W/d = 3, and is modified with a narrowed waist with W'/d = 1.5. As the SSPP modes are concentrated in the grooves, we can use localized deposition of control materials to achieve satisfactory modulation to the transmission spectrum. The DNA molecules are therefore restricted to a thin layer on the walls of the groove region that only covers a limited area. The active area has dimensions of 50μm×80μm and a thickness of only 4μm, as highlighted in Figure 58(a). In practice, to facilitate the DNA sample loading, a two-module design with separate sample deposition and flip-chip integration can be applied, in a similar manner as illustrated in Figure **14**. The practicality of the DNA sample deposition via chemical bonding is also described in Chapter III and will not be repeated here.

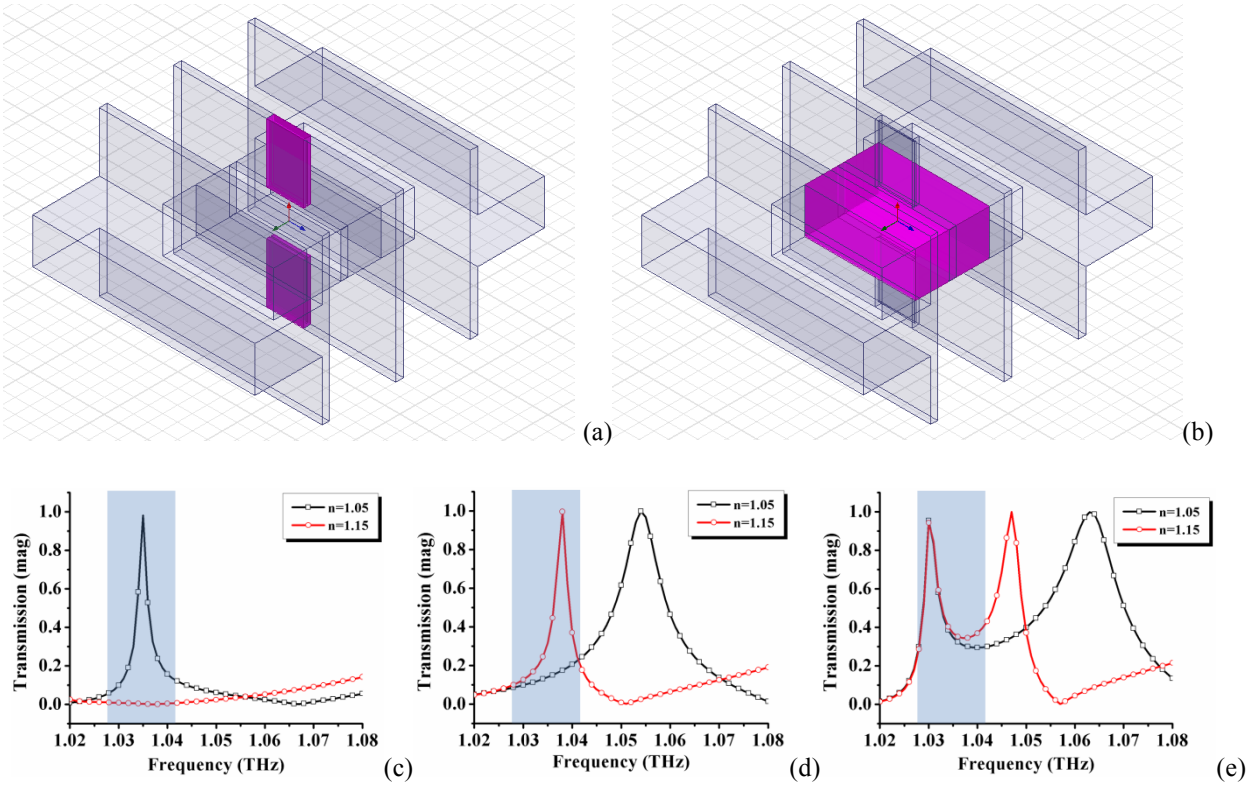

Figure 58 Sketch of the narrow waist DC-SSPP structure (a) with the active area with DNA molecules highlighted and (b) with the reconfiguration section highlighted. The transmission spectra from (c) to (e) is showing the *pass-block* function, the *block-pass* function, and the *pass-pass* function, respectively

By changing the size of the DC-SSPP structure, the location of the transmission peaks can be shifted in proportion. As a result, slight adjustments to the dimensions of the design can be introduced to realize the three directed logic functions while using a unique probe THz signal. Another approach, on the other hand, is to include an extra control section in the element design.

This section is referred as the reconfiguration control and is used to actively switch among the three directed logic functions while a universal geometric design of the DC-SSPP element is used. In Figure 58(b), a 100 μm-long section of the center waveguide is highlighted as an example of the reconfiguration control section. In the same figure, the switching characteristics of the *pass-block*, *block-pass,* and *pass-pass* elements are demonstrated by changing the material properties in this section. Such change can be induced thermally, electrically, optically, or even by using the same bio-molecular assays that are used for the Boolean switching functions. It is worth noting that reconfiguration is only required when the directed logic circuit needs to adjust its overall Boolean arithmetic. Therefore, this mechanism can be carried out at a much slower speed compared with the Boolean operations themselves, making the use of slow but reliable means such as liquid crystal acceptable.

With the DC-SSPP directed logic network concept, it is straightforward to reflect the same Boolean operation as in the example given in Figure **57**. The node setup is qualitatively illustrated in Figure **59**. Instead of reaction specific chemicals serving as the logic input, in our setup, four DNA molecules are used to control the pass/block of each logic nodes to realize the designated Boolean operation. The DNA samples could be chosen wisely to fit specific bio-computing objectives, in a variety of scenarios including but not limited to pathogenic gene detection, genetic mutation study, and gene sequencing in general.

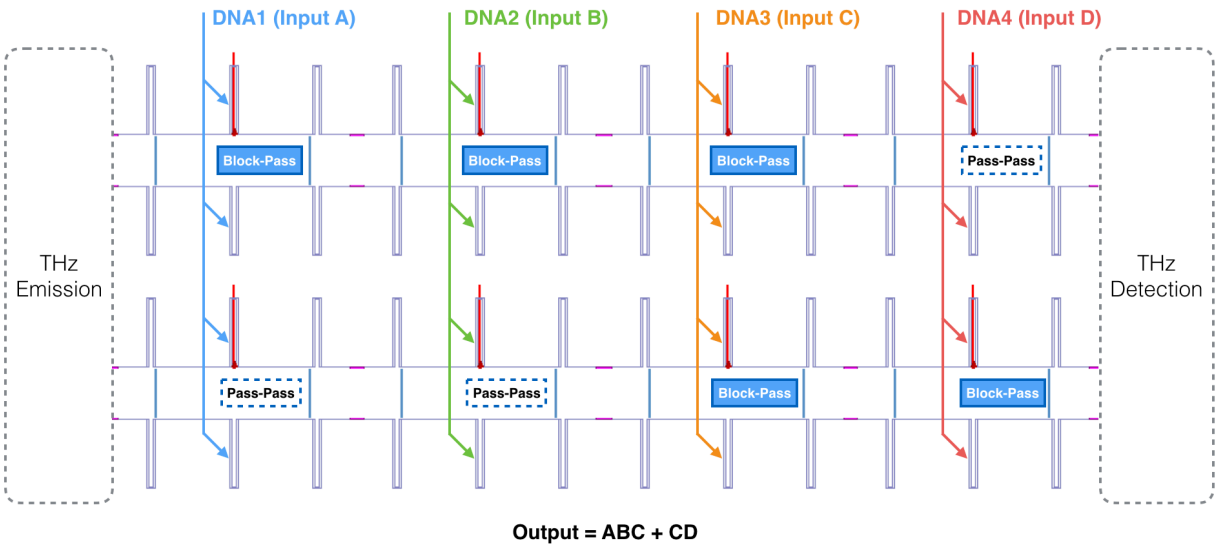

Figure 59 Example of Boolean operation enabled by DC-SSPP directed logic network

It is worth noting that although the above preliminary study used DNA molecules with different binding status to demonstrate the effectiveness of the DC-SSPP directed logic nodes, the applicable biological assay is certainly not restricted to only DNA hybridization/denaturation. In practice, bio-molecules with known dielectric constant change due to shifts in their states have been identified to include RNAs, chlorophyll proteins, heme proteins such as cytochrome c and myoglobin, and even entire bacterial cells and spores [23, 68, 69, 70, 71, 72, 73, 74, 75, 76]. We predict the applicability of these various bio-molecules and substances to the DC-SSPP directed logic network design when the same principle of THz modulation is applied.

6.5 DC-SSPP THz directed logic elements in THz circuitry: Enhancement mode

As revealed in Chapter IV, the modulation to the material dielectric properties can be effectively induced by changing the free carrier concentration in doped semiconductors. Similarly, both enhancement mode (injecting free carriers) and depletion mode (extracting free carriers) can be employed to change the refractive index of the chosen material. We use n-doped GaAs as the control material to construct the DC-SSPP directed logic elements for THz circuitry applications.

The first example of the element operating in enhancement mode is shown in Figure 60. It has dimensions of d = 7.4 μm, a/d = 0.1, h/d = 0.8, t/d = 0.3, and W/d = 3, and is modified with a narrowed waist with W'/d = 1.5. Similarly, as in **6.4**, the GaAs is restricted to a small area within the wall region of the structure. The size of the active area is 3.7μm×6μm, and the thickness of the GaAs is only 74 nm, as shown in Figure 60(a). An elevated operating frequency over 9 THz gives rise to the smaller dimensions of the structure design in this case. This frequency is chosen such that GaAs is reasonably transparent to the signal without having the excessive material loss.

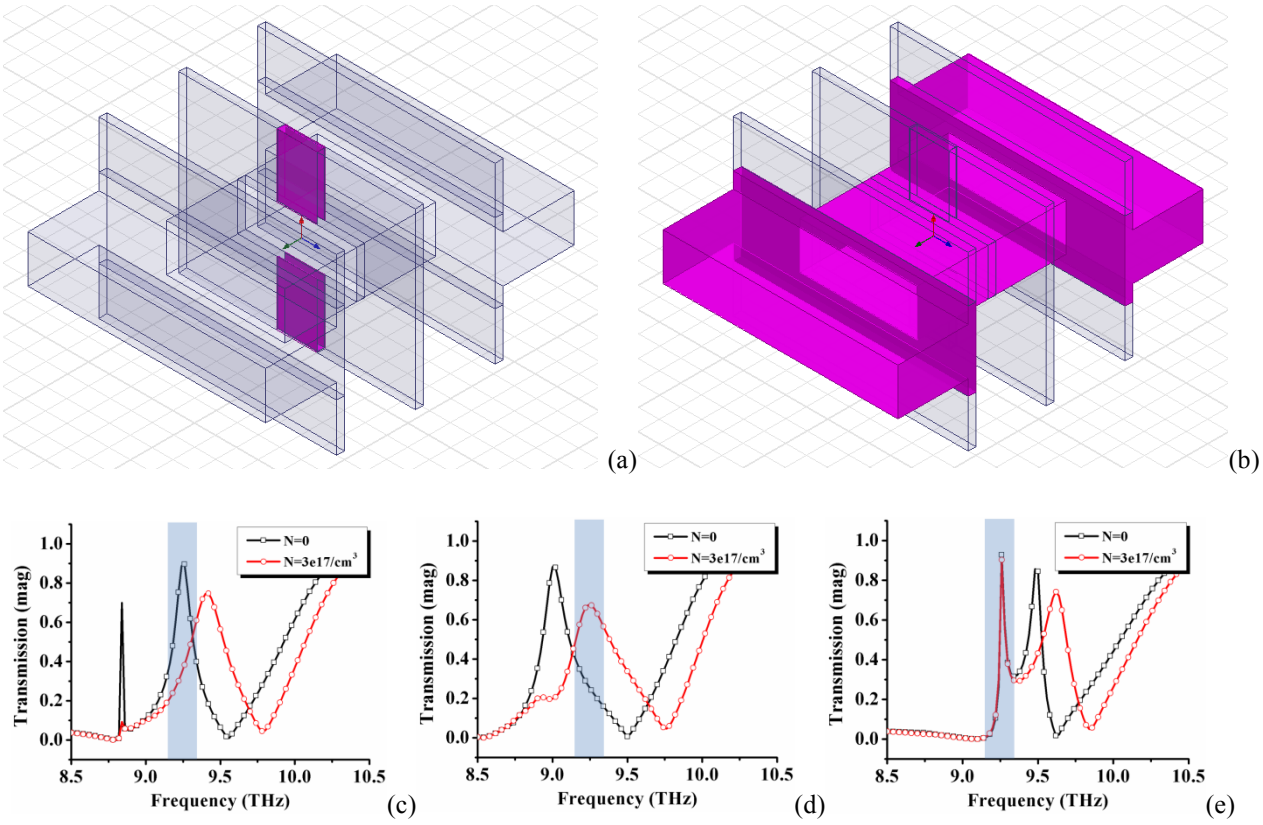

Figure 60 Sketch of the narrow waist DC-SSPP structure comprising doped semiconductor in enhancement mode (a) with the active area highlighted and (b) with the reconfiguration section highlighted. The transmission spectra from (c) to (e) is showing the *pass-block* function, the *block-pass* function, and the *pass-pass* function, respectively

In operation, the logic level 0 and 1 are represented by the free carrier concentration of $N = 0$ and $= 3\times10^{17}cm^{-3}$ in the GaAs control region, respectively. A reconfiguration section is designed to switch the functionality of the element if desired and is highlighted in Figure 60(b). The reconfiguration control in this example is realized by modulating the refractive index among three predetermined values of $n_1 = 1.501$, $n_2 = 1.590$ and $n_3 = 1.680$, potentially achievable by using nematic liquid crystals [204]. The spectral output under these reconfiguration controls are shown in Figure 60(c)-(e), where a unique THz probe signal is used and all three directed logic functions are demonstrated.

For the convenience of the readers, the modified Drude model that describes the dielectric constant of heteropolar semiconductors is included here again as below:

$$\varepsilon(\omega) = \varepsilon_\infty + \frac{\omega_{TO}^2(\varepsilon_s - \varepsilon_\infty)}{\omega_{TO}^2 - \omega^2 - i\omega\gamma} - \frac{\omega_p^2}{\omega(\omega + i\Gamma)} \tag{86}$$

$$\omega_p = \sqrt{\frac{Ne^2}{\varepsilon_0 m^*}} \tag{87}$$

A dielectric constant is a complex number consisting of both the real and the imaginary part. As a result, non-zero absorption loss, however small, must exist for the semiconductor materials. In our design, the dielectric constant of GaAs is calculated at f = 9.25 THz to be $\varepsilon = 4.43 + j0.22$ $(n = 2.1 + j0.052)$ and $\varepsilon = -0.045 + j0.47$ $(n = 0.46 + j0.51)$ for the free carrier density of $N = 0$ and $N = 3{\times}10^{17} cm^{-3}$, respectively. The considerable change in the real refractive index causes the shift of the transmission window as shown in Figure 60. The non-zero material loss, on the other hand, gives rise to the transmission maxima slightly lower than unity.

As mentioned in **6.4**, the reconfiguration control can be realized in multiple ways. In Figure **61**, the second example of the directed logic element design is sketched, where the enhancement mode is used to control both the Boolean logic and the reconfiguration. In this example, the entire structure is made of GaAs. It has the dimensions of d = 1.18μm, a/d = 0.1, h/d = 1.6, t/d = 0.2, W/d = 6, and a narrowed waist with W'/d = 3.2. The Boolean logic is controlled by a localized layer of doped GaAs, which occupies an area of 3.8μm×1.9μm and has the thickness of 23.6 nm. The logic level 0 and 1 are still represented by the free carrier density of $N = 0$ and $N = 3{\times}10^{17} cm^{-3}$ in this region.

A 700-nm middle section of the waveguide is selected as the reconfiguration control, as shown in Figure **61**(b). The free carrier concentration in this section is chosen to vary among the three values of $N = 0$, $N = 4.5{\times}10^{17} cm^{-3}$, and $N = 9{\times}10^{17} cm^{-3}$. Enabled by such Boolean and reconfiguration control, directed logic functions are successfully demonstrated in Figure **61**(c)-(e).

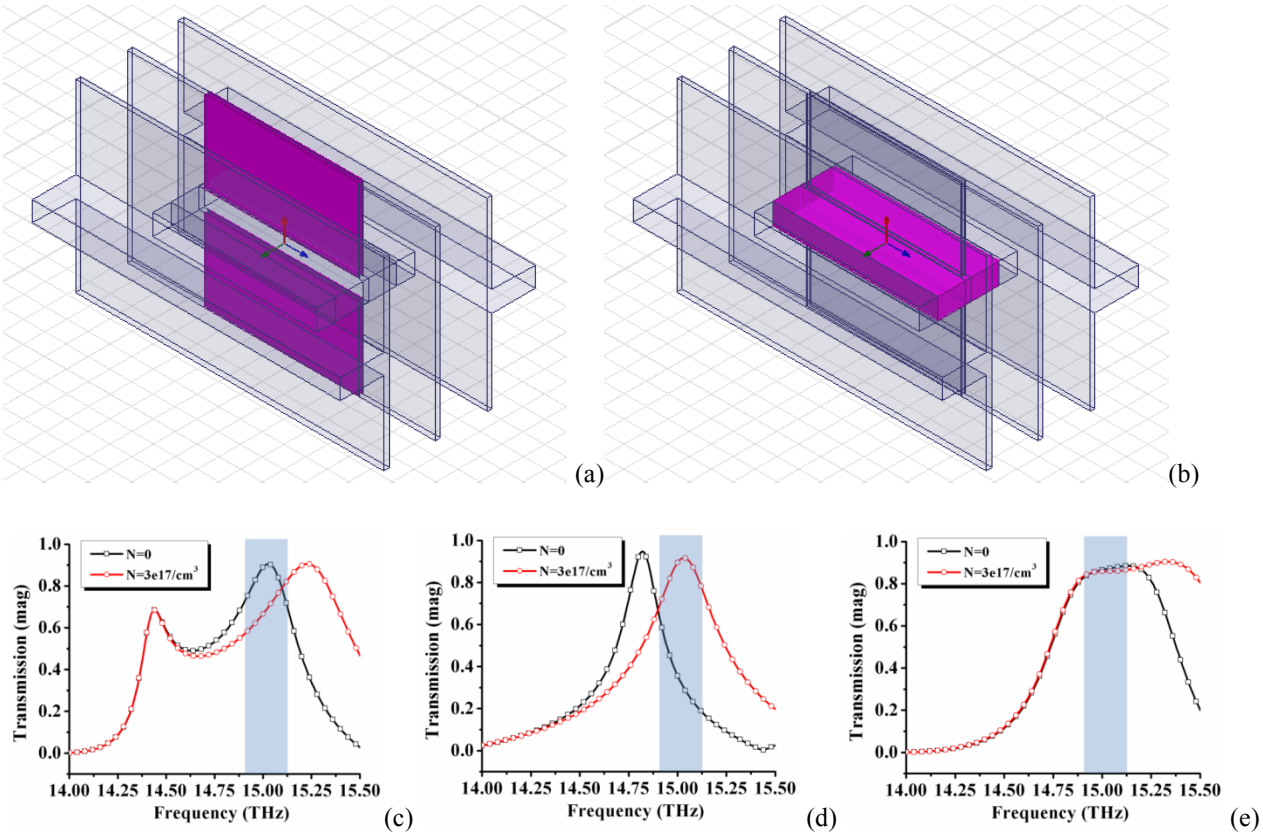

Figure 61 Sketch of the narrow waist DC-SSPP structure comprising doped semiconductor in the enhancement mode (a) with the active area highlighted and (b) with the reconfiguration section highlighted. The transmission spectra from (c) to (e) is showing the *pass-block* function, the *block-pass* function, and the *pass-pass* function, respectively

As the structure is entirely formed by GaAs, the operating frequency is selected to be $f = 15$ THz so that the material loss could be minimized. At this frequency, the dielectric constant of GaAs is calculated to be $\varepsilon = 10.1 + j0.006$ ($n = 3.18 + j0.001$) and $\varepsilon = 8.35 + j0.066$ ($n = 2.89 + j0.011$) for the free carrier density of $N = 0$ and $N = 3\times10^{17} cm^{-3}$, respectively.

6.6 DC-SSPP THz directed logic elements in THz circuitry: Depletion mode

The Boolean directed logic elements can also be realized with GaAs control in the depletion mode. In this mode, a Schottky contact is formed between the semiconductor material and the metallic electrode. The thickness of the region depleted of free carriers, also known as the space-charge region, will vary as a function of the biased voltage across the contact. The effective refractive index is modulated accordingly, changing the phase of the propagating THz signals.

An example structure under this working principle is shown in Figure 62. It has dimensions of d = 1.28 μm, a/d = 1/4, h/d = 1.5, t/d = 1/4, W/d = 9, and a narrowed waist with W'/d = 3. The element is still constructed entirely with GaAs. The active area for the Boolean logic input has the size of 3.8μm×1.9μm and is highlighted in Figure 62(a).

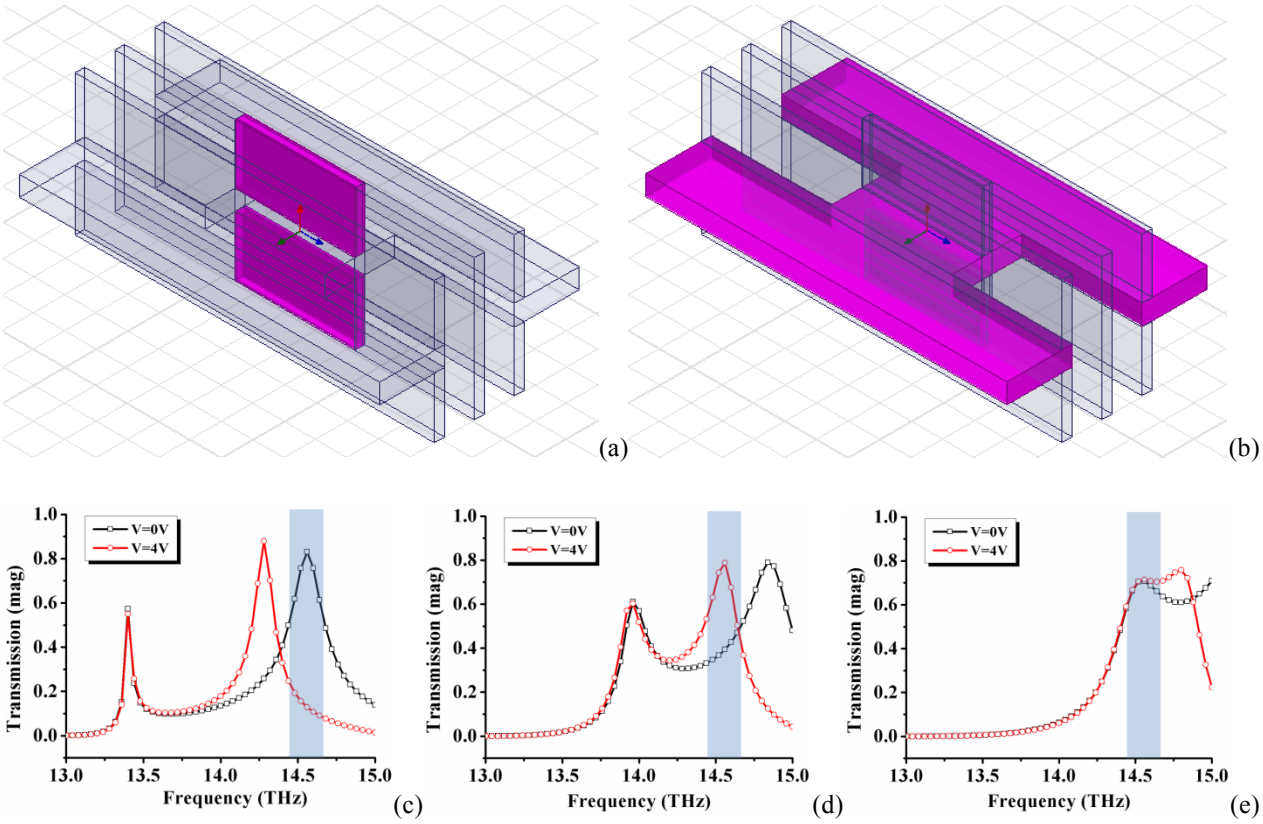

Figure 62 Sketch of the narrow waist DC-SSPP structure comprising doped semiconductor in the depletion mode (a) with the active area highlighted and (b) with the reconfiguration section highlighted. The transmission spectra from (c) to (e) is showing the *pass-block* function, the *block-pass* function, and the *pass-pass* function, respectively

The carrier depletion is induced by applying voltages across the Schottky contact formed by the metal-GaAs interface, and the thickness of the space-charge region is calculated by the following formula:

$$D_{dep} = \sqrt{\frac{2\varepsilon_s\varepsilon_0(V_{bi}+V)}{eN}} \tag{88}$$

The effective refractive index as seen by the propagating THz signal is controlled by the changing depth of the depletion region. On the other hand, the reconfiguration, as illustrated in Figure 62(b), is controlled by free carrier injection. The three directed logic functions are shown

in Figure 62(c)-(e), with the control voltage swing of 0 - 4 V and reconfiguration carrier concentration of $N = 0$, $N = 2\times10^{17}cm^{-3}$, and $N = 4\times10^{17}cm^{-3}$. The operating frequency is chosen to be 14.5 THz in order to minimize the material loss.

References

[1] C. H. Doan, S. Emami, D. A. Sobel, A. M. Niknejad, and R. W. Broderson, "Design considerations for 60 GHz CMOS radios," *IEEE Communications Magazine,* Vol 42, No 12, pp. 132-140, 2004.

[2] U. K. Mishra, Y.-F. Wu, B. P. Keller, S. Keller, and S. P. Denbaars, "GaN microwave electronics," *IEEE Transactions on Microwave Theory and Techniques,* Vol 46, No 6, pp. 756-761, 1997.

[3] Q. Chen, J. W. Yang, M. Blasingame, C. Faber, A. T. Ping, and I. Adesida, "Microwave electronics device applications of AlGaN/GaN heterostructures," *Materials Science and Engineering B: Solid-State Materials for Advanced Technology,* Vol 59, No 1-3, pp. 395-400, 1999.

[4] M. Born, and E. Wolf, Principles of Optics, Cambridge University Press, 1999.

[5] J. W. Goodman, F. J. Leonberger, S.-Y. Kung, and R. A. Athale, "Optical interconnections for VLSI systems," *Proceedings of the IEEE,* Vol 72, No 7, pp. 850-866, 1984.

[6] D. A. B. Miller, "Rationale and challenges for optical interconnects to electronic chips," *Proceedings of the IEEE,* Vol 88, No 6, pp. 728-749, 2000.

[7] A. V. Krishnamoorthy, and D. A. B. Miller, "Scaling optoelectronic–VLSI circuits into the 21st century," *IEEE Journal of Selected Topics in Quantum Electronics,* Vol 2, No 1, pp. 55-76, 1996.

[8] M. Dyakonov, and M. Shur, "Shallow water analogy for a ballistic field effect transistor: New mechanism of plasma wave generation by dc current," *Physical Review Letters,* Vol 71, No 15, pp. 2465-2468, 1993.

[9] M. Dyakonov, and M. Shur, "Detection, mixing, and frequency multiplication of terahertz radiation by two-dimensional electronic fluid," *IEEE Transactions on Electron Devices,* Vol 43, No 3, pp. 380-387, 1996.

[10] C. R. Williams, S. R. Andrews, S. A. Maier, A. I. Fernández-Domínguez, L. Martín-Moreno, and F. J. García-Vidal, "Highly confined guiding of terahertz surface plasmon polaritons on structured metal surfaces," *Nature Photonics,* Vol 3, p. 175, 2008.

[11] A. Degiron, and T. W. Ebbesen, "The role of localized surface plasmon modes in the enhanced transmission of periodic subwavelength apertures," *Journal of Optics A: Pure and Applied Optics,* Vol 7, pp. S90-S96, 2005.

[12] J. Gomez Rivas, C. Schotsch, P. Haring Bolivar, and H. Kurz, "Enhanced transmission of THz radiation through subwavelength holes," *Physical Review B,* Vol 68, p. 201306, 2003.

[13] D. M. Mittleman, R. H. Jacobsen, and M. C. Nuss, "T-ray imaging," *IEEE Journal of Selected Topics in Quantum Electronics,* Vol 2, pp. 679-692, 1996.

[14] D. Grischkowsky, S. Keiding, M. van Exter, and Ch. Fattinger, "Far-infrared time-domain spectroscopy with terahertz beams of dielectrics and semiconductors," *Journal of the Optical Society of America B,* Vol 7, No 10, pp. 2006-2015, 1990.

[15] J. T. Kindt, and C. A. Schmuttenmaer, "Far-infrared dielectric properties of polar liquids probed by femtosecond terahertz pulse spectroscopy," *The Journal of Physical Chemistry,* Vol 100, pp. 10373-10379, 1996.

[16] P. H. Siegel, "Terahertz technology," *IEEE Transactions on Microwave Theory and Techniques,* Vol 50, pp. 910-928, 2002.

[17] A. Lisauskas, U. Pfeiffer, E. Ojefors, and P. H. Bolivar, "Rational design of high-responsivity detectors of terahertz radiation based on distributed self-mixing in silicon field-effect transistors," *Journal of Applied Physics,* Vol 105, p. 114511, 2009.

[18] L. Vicarelli, M. S. Vitiello, D. Coquillat, A. Lombardo, A. C. Ferrari, W. Knap, M. Polini, V. Pellegrini, and A. Tredicucci, "Graphene field-effect transistors as room-temperature terahertz detectors," *Nature Materials,* Vol 11, pp. 865-871, 2012.

[19] J. Barber, D. E. Hooks, D. J. Funk, R. D. Averitt, A. J. Taylor, and D. Babikov, "Temperature-Dependent Far-Infrared Spectra of Single Crystals of High Explosives Using Terahertz Time-Domain Spectroscopy," *The Journal of Physical Chemistry,* Vol 109, No 15, pp. 3501-3505, 2005.

[20] J. Chen, Y. Chen, H. Zhao, G. J. Bastiaans, and X.-C. Zhang, "Absorption coefficients of selected explosives and related compounds in the range of 0.1-2.8 THz," *Optics Express,* Vol 15, No 19, pp. 12060-12067, 2007.

[21] M. Brucherseifer, M. Nagel, P. Haring Bolivar, H. Kurz, A. Bosserhoff, and R. Büttner, "Label-free probing of the binding state of DNA by time-domain terahertz sensing," *Applied Physics Letters,* Vol 77, No 24, pp. 4049-4051, 2000.

[22] B. M. Fischer, M. Walther and P. U. Jepsen, "Far-infrared vibrational modes of DNA components studied by terahertz time-domain spectroscopy," *Physics in Medicine and Biology,* Vol 47, No 21, pp. 3807-3814, 2002.

[23] S. P. Mickan, A. Menikh, H. Liu, C. A. Mannella, R. MacColl, D. Abbott, J. Munch, and X.-C. Zhang, "Label-free bioaffinity detection using Terahertz technology," *Physics in Medicine and Biology,* Vol 47, No 21, pp. 3789-3795, 2002.

[24] A. G. Markelz, "Terahertz Dielectric Sensitivity to Biomolecular Structure and Function," *IEEE Journal of Selected Topics in Quantum Electronics,* Vol 14, No 1, pp. 180-190, 2008.

[25] R. Mendis, and D. Grischkowsky, "Plastic ribbon THz waveguides," *Journal of Applied Physics,* Vol 88, pp. 4449-4451, 2000.

[26] G. Gallot, S. P. Jamison, R. W. McGowan, and D. Grischkowsky, "Terahertz Waveguides," *Journal of the Optical Society of America B,* Vol 17, pp. 851-863, 2000.

[27] S. P. Jamison, R. W. McGowan, and D. Grischkowsky, "Single-mode waveguide propagation and reshaping of sub-ps terahertz pulses in sapphire fiber," *Applied Physics Letters,* Vol 76, pp. 1987-1989, 2000.

[28] K. Wang, and D. M. Mittleman , "Metal wires for terahertz wave guiding," *Nature,* Vol 432, pp. 376-379, 2004.

[29] J. B. Pendry, L. Martin-Moreno, and F. J. Garcia-Vidal , "Mimicking Surface Plasmons with Structured Surfaces," *Science,* Vol 305, pp. 847-848, August 2004.

[30] S. A. Maier, S. R. Andrews, L.Martín-Moreno, and F. J. García-Vidal, "Terahertz Surface Plasmon-Polariton Propagation and Focusing on Periodically Corrugated Metal Wires," *Physical Review Letters,* Vol 97, p. 176805, 2006.

[31] Q. Gan, Z. Fu, Y. J. Ding, and F. J. Bartoli, "Ultrawide-Bandwidth Slow-Light System Based on THz Plasmonic Graded Metallic Grating Structures," *Physical Review Letters,* Vol 100, p. 256803, 2008.

[32] A. I. Fernandez-Dominguez, E. Moreno, L. Martin-Moreno, and F. J. Garcia-Vidal, "Guiding terahertz waves along subwavelength channels," *Physical Review B,* Vol 79, p.

233104, 2009.

[33] F. J. Garcia-Vidal, L. Martin-Moreno, T. W. Ebbesen, and L. Kuipers, "Light passing through subwavelength apertures," *Reviews of Modern Physics,* Vol 82, pp. 729-787, 2010.

[34] H. J. Lezec, A. Degiron, E. Devaux, R. A. Linke, L. Martin-Moreno, F. J. Garcia-Vidal, and T. W. Ebbesen, "Beaming Light from a Subwavelength Aperture," *Science,* Vol 297, pp. 820-822, 2002.

[35] E. Moreno, F. J. Garcia-Vidal, and L. Martin-Moreno, "Enhanced transmission and beaming of light via photonic crystal surface modes," *Physical Review B,* Vol 69, p. 121402, 2004.

[36] S.-H. Kim, T.-T. Kim, S.-S. Oh, J.-E. Kim, H.-Y. Park, and C.-S. Kee, "Experimental demonstration of self-collimation of spoof surface plasmons," *Physical Review B,* Vol 83, p. 165109, 2011.

[37] S. I. Bozhevolnyi, J. Erland, K. Leosson, P. M. W. Skovgaard, and J. M. Hvam, "Waveguiding in Surface Plasmon Polariton Band Gap Structures," *Physical Review Letters,* Vol 86, pp. 3008-3011, 2001.

[38] J. Esteban, and J. M. Rebollar, "Characterization of Corrugated Waveguides by Modal Analysis," *IEEE Transactions on Microwave Theory and Techniques,* Vol 39, No 6, pp. 937-943, 1991.

[39] Y.-L. Kok, "Boundary-value solution to electromagnetic scattering by a rectangular groove in a ground plane," *Journal of the Optical Society of America A,* Vol 9, No 2, pp. 302-311, 1992.

[40] Y.-L. Kok, "General solution to the multiple-metallic-grooves scattering problem the fast-polarization case," *Applied Optics,* Vol 32, No 14, pp. 2573-2581, 1993.

[41] R. E. Collin, Foundations for Microwave Engineering, 2nd Edition, Wiley-IEEE Press.

[42] B. D. McVey, M. A. Basten, J. H. Booske, J. Joe, and J. E. Scharer , "Analysis of rectangular waveguide-gratings for amplifier applications," *IEEE Transactions on Microwave Theory and Techniques,* Vol 42, pp. 995-1003, 1994.

[43] J. Joe, J. Scharer, J. Booske, and B. McVey, "Wave dispersion and growth analysis of low-voltage grating Cerenkov amplifiers," *Physics of Plasmas,* Vol 1, No 1, pp. 176-188, 1994.

[44] A. A. Maragos, Z. C. Ioannidis, and I. G. Tigelis, "Dispersion Characteristics of a

Rectangular Waveguide Grating," *IEEE Transactions on Plasma Science,* Vol 31, No 5, pp. 1075-1082, 2003.

[45] M. Mineo, C. Paoloni, A. Di Carlo, A. M. Fiorello, and M. Dispenza, "Corrugated waveguide slow-wave structure for THz travelling wave tube," *Proceedings of the 39th European Microwave Conference,* pp. 842-845, 2009.

[46] M. Mineo, and C. Paoloni, "Corrugated Rectangular Waveguide Tunable Backward Wave Oscillator for Terahertz Applications," *IEEE Transactions on Electron Devices,* Vol 57, No 6, pp. 1481-1484, 2010.

[47] D. Martin-Cano, M. L. Nesterov, A. I. Fernandez-Dominguez, F. J. Garcia-Vidal, L. Martin-Moreno, and E. Moreno, "Domino plasmons for subwavelength terahertz circuitry," *Optics Express,* Vol 18, No 2, pp. 754-764, 2010.

[48] *Matlab,* Mathworks Inc., Natick, MA.

[49] *CST,* Computer Simulation Technology AG, Framingham, MA.

[50] R. Safavi-Naini, and R. H. MacPhie, "On Solving Waveguide Junction Scattering Problems by the Conservation of Complex Power Technique," *IEEE Transactions on Microwave Theory and Techniques,* Vol 29, pp. 337-343, 1981.

[51] L. Li, "Formulation and comparison of two recursive matrix algorithms for modeling layered diffraction gratings," *Journal of the Optical Society of America A,* Vol 13, pp. 1024-1035, 1996.

[52] Z.-Y. Li, and L.-L. Lin, "Photonic band structures solved by a plane-wave-based transfer-matrix method," *Physical Review E,* Vol 67, p. 046607, 2003.

[53] S. K. Sharmaa, N. Sehgalb, and A. Kumar, "Biomolecules for development of biosensors and their applications," *Current Applied Physics,* Vol 3, No 2-3, pp. 307-316, 2003.

[54] P. D'Orazio, "Biosensors in clinical chemistry," *Clinica Chimica Acta,* Vol 334, No 1-2, pp. 41-69, 2003.

[55] R. B. Thompson, and E. R. Jones, "Enzyme-based fiber optic zinc biosensor," *Analytical Chemistry,* Vol 65, pp. 730-734, 1993.

[56] M. Chee, R. Yang, E. Hubbell, A. Berno, X. C. Huang, D. Stern, J. Winkler, D. J. Lockhart, M. S. Morris, and S. P. A. Fodor, "Accessing Genetic Information with High-Density DNA Arrays," *Science,* Vol 274, No 5287, pp. 610-614, 1996.

[57] X. D. Song, and B. I. Swanson, "Direct, Ultrasensitive, and Selective Optical Detection of Protein Toxins Using Multivalent Interactions," *Analytical Chemistry,* Vol 71, No 11, pp. 2097-2107, 1999.

[58] H. Ozaki, and L. W. McLaughlin, "The estimation of distances between specific backbonelabeled sites in DNA using fluorescence resonance energy transfer," *Nucleic Acids Research,* Vol 20, No 19, pp. 5205-5214, 1992.

[59] Z. Zhu, J. Chao, H. Yu, and A. S. Waggoner, "Directly labeled DNA probes using fluorescent nucleotides with different length linkers," *Nucleic Acids Research,* Vol 22, No 16, pp. 3418-3422, 1994.

[60] Z. Zhu, and A. S. Waggoner, "Molecular mechanism controlling the incorporation of fluorescent nucleotides into DNA by PCR," *Cytometry,* Vol 28, No 3, pp. 206-211, 1997.

[61] M. L. Larramendy, W. El-Rifai, S. Knuutila, "Comparison of fluorescein isothiocyanate- and Texas red-conjugated nucleotides for direct labeling in comparative genomic hybridization," *Cytometry,* Vol 31, No 3, pp. 174-179, 1998.

[62] J. M. Eyster, and E. W. Prohofsky, "Soft modes and structure of DNA doubly helix," *Physical Review Letters,* Vol 38, pp. 371-373, 1977.

[63] B. F. Putnam, L. L. Van Zandt, E. W. Prohofsky, and W. N. Mei, "Resonant and localized breathing modes in terminal regions of the DNA double helix," *Biophysical Journal,* Vol 35, No 2, pp. 271-287, 1981.

[64] L. L. Van Zandt, and V. K. Saxena, "Millimeter-microwave spectrum of DNA Six predictions for spectroscopy," *Physical Review A,* Vol 39, pp. 2672-2674, 1989.

[65] W. Zhuang, Y. Feng, and E. W. Prohofsky, "Self-consistent calculation of localized DNA vibrational properties at a double-helix–single-strand junction with anharmonic potential," *Physical Review A,* Vol 41, pp. 7033-7042, 1990.

[66] B. Brooks, and M. Karplus, "Normal modes for specific motions of macromolecules: application to the hinge-bending mode of lysozyme," *Proceedings of the National Academy of Sciences USA,* Vol 82, No 15, pp. 4995-4999, 1985.

[67] D. Lin, A. Matsumoto, and N. Go, "Normal mode analysis of a double-stranded DNA dodecamer d(CGCGAATTCGCG)," *The Journal of Chemical Physics,* Vol 107, pp. 3684-3690, 1997.

[68] A. G. Markelz, A. Roitberg, and E. J. Heilweil, "Pulsed terahertz spectroscopy of DNA,

bovine serum albumin and collagen between 0.1 and 2.0 THz," *Chemical Physics Letters,* Vol 320, No 1-2, pp. 42-48, 2000.

[69] M. Walther, B. Fischer, M. Schall, H. Helm, and P.U. Jepsen, "Far-infrared vibrational spectra of all-trans, 9-cis and 13-cis retinal measured by THz time-domain spectroscopy," *Chemical Physics Letters,* Vol 332, No 3-4, pp. 389-395, 2000.

[70] T. Hasebe, Y.Yamada, and H. Tabata, "Label-free THz sensing of living body-related molecular binding using a metallic mesh," *Biochemical and Biophysical Research Communications,* Vol 414, No 1, pp. 192-198, 2011.

[71] H. Yoshida, Y. Ogawa, Y. Kawai, S. Hayashi, A. Hayashi, C. Otani, E. Kato, F. Miyamaru, and K. Kawase, "Terahertz sensing method for protein detection using a thin metallic mesh," *Applied Physics Letters,* Vol 91, p. 253901, 2007.

[72] R. J. Falconer, and A. G. Markelz, "Terahertz Spectroscopic Analysis of Peptides and Proteins," *Journal of Infrared, Millimeter and Terahertz Waves,* Vol 33, No 10, pp. 973-988, 2012.

[73] K. Yamamoto, K. Tominaga, H. Sasakawa, A. Tamura, H. Murakami,H. Ohtake, and N. Sarukura, "Far-infrared absorption measurements of polypeptides and cytochrome c by THz radiation," *Bulletin of the Chemical Society of Japan,* Vol 75, p. 1083–1092, 2002.

[74] H. Chen, Y.-G. Qu, W.-X. Peng, T.-Y. Kuang, L.-B. Li, and L. Wang, "Investigation of chlorophyll protein 43 and 47 denaturation by terahertz time domain spectroscopy," *Chinese Physics Letters,* Vol 24, p. 2131–2134, 2007.

[75] T. Globus, T. Dorofeeva, I. Sizov, B. Gelmont, M. Lvovska, T. Khromova, O. Chertihin, and Y. Koryakina, "Sub-THz Vibrational Spectroscopy of Bacterial Cells and Molecular Components," *American Journal of Biomedical Engineering,* Vol 2, No 4, pp. 143-154, 2012.

[76] T. Globus, A. M. Moyer, B. Gelmont, T. Khromova, M. I. Lvovska, I. Sizov, and J. Ferrance, "Highly Resolved Sub-Terahertz Vibrational Spectroscopy of Biological Macromolecules and Cells," *IEEE Sensors Journal,* Vol 13, No 1, pp. 72-79, 2013.

[77] R. Drmanac, S. Drmanac, Z. Strezoska, T. Paunesku, I. Labat, M. Zeremski, J. Snoddy, W. K. Funkhouser, B. Koop, and L. Hood, "DNA-sequence determination by hybridization—a strategy for efficient large-scale sequencing," *Science,* Vol 260, No 5114, pp. 1649-1652, 1993.

[78] M. Nagel, P. Haring Bolivar, M. Brucherseifer, H. Kurz, A. Bosserhoff, and R. Buettner, "Integrated THz technology for label-free genetic diagnostics," *Applied Physics Letters,* Vol 80, No 1, pp. 154-156, 2002.

[79] M. Nagel, F. Richter, P. Haring-Bolívar, and H. Kurz, "A functionalized THz sensor for marker-free DNA analysis," *Physics in Medicine and Biology,* Vol 48, pp. 3625-3636, 2003.

[80] P. H. Bolivar, M. Nagel, F. Richter, M. Brucherseifer, H. Kurz, A. Bosserhoff, and R. Buettner, "Label–free THz sensing of genetic sequences: towards 'THz biochips'," *Philosophical Transactions of the Royal Society of London A,* Vol 15, No 362, pp. 323-335, 2004.

[81] *Ansoft HFSS,* Ansys Inc., Pittsburg, PA.

[82] M. Nagel, M. Foerst, and H. Kurz, "THz biosensing devices: fundamentals and technology," *Journal of Physics: Condensed Matter,* Vol 18, No 18, pp. 610-618, 2006.

[83] K. Song, and P. Mazumder, "Dynamic Terahertz Spoof Surface Plasmon–Polariton Switch Based on Resonance and Absorption," *IEEE Transactions on Electron Devices,* Vol 58, No 7, pp. 2172-2176, July 2011.

[84] S. L. Dexheimer, Terahertz Spectroscopy: Principles and Applications, CRC Press, 2007.

[85] Z. D. Taylor, R. S. Singh, D. B. Bennett, P. Tewari, C. P. Kealey, N. Bajwa, M. O. Culjat, A. Stojadinovic, J.-P. Hubschman, E. R. Brown, and W. S. Grundfest, "THz Medical Imaging: in vivo Hydration Sensing," *IEEE Transactions on Terahertz Science and Technology,* Vol 1, No 1, pp. 1-20, 2011.

[86] T. Globus, I. Sizov, and B. Gelmont, "Teraherz vibrational spectroscopy of E. coli and molecular constituents: Computational modeling and experiment," *Advances in Bioscience and Biotechnology,* Vol 4, pp. 493-503, 2013.

[87] J. Xu, K. W. Plaxco, S. J. Allen, J. E. Bjarnason, and E. R. Brown, "0.15–3.72 THz absorption of aqueous salts and saline solutions," *Applied Physics Letters,* Vol 90, p. 031908, 2007.

[88] R. H. Walden, "Analog-to-digital converter survey and analysis," *IEEE Journal on Selected Areas in Communications,* Vol 17, No 4, pp. 539-550, 1999.

[89] A. Khilo, S. J. Spector, M. E. Grein, A. H. Nejadmalayeri, C. W. Holzwarth, M. Y. Sander, M. S. Dahlem, M. Y. Peng, M. W. Geis, N. A. DiLello, J. U. Yoon, A. Motamedi, J. S.

Orcutt, J. P. Wang, C. M. Sorace-Agaskar, and et al., "Photonic ADC: overcoming the bottleneck of electronic jitter," *Optics Express,* Vol 20, No 4, pp. 4454-4469, 2012.

[90] P. W. Juodawlkis, J. C. Twichell, G. E. Betts, J. J. Hargreaves, R. D. Younger, J. L. Wasserman, F. J. O'Donnell, K. G. Ray, and R. C. Williamson, "Optically sampled analog-to-digital converters," *IEEE Transactions on Microwave Theory and Techniques,* Vol 49, No 10, pp. 1840-1853, 2001.

[91] F. Coppinger, A. S. Bhushan, and B. Jalali, "Photonic time stretch and its application to analog-to-digital conversion," *IEEE Transactions on Microwave Theory and Techniques,* Vol 47, No 7, pp. 1309-1314, 1999.

[92] A. S. Bhushan, P. V. Kelkar, B. Jalali, O. Boyraz, and M. Islam, "130-GSa/s photonic analog-to-digital converter with time stretch preprocessor," *IEEE Photonics Technology Letters,* Vol 14, No 5, pp. 684-686, 2002.

[93] T. R. Clark, Jr., and M. L. Dennis, "Toward a 100-Gsample/s photonic A-D converter," *IEEE Photonics Technology Letters,* Vol 13, No 3, pp. 236-238, 2001.

[94] L. Y. Nathawad, R. Urata, B. A. Wooley, and D. A. B. Miller, "A 20 GHz bandwidth, 4 b photoconductive-sampling time-interleaved CMOS ADC," *Digest of Technical Papers, IEEE International Solid-State Circuits Conference,* Vol 1, 2003.

[95] M. Johansson, B. Löfving, S. Hård, L. Thylén, M. Mokhtari, U. Westergren, and C. Pala, "Study of an ultrafast analog-to-digital conversion scheme based on diffractive optics," *Applied Optics,* Vol 39, No 17, pp. 2881-2887, 2000.

[96] C. Pala, L. Thylen, M. Mokhtari, and U. Westergren, "A high-speed electro-optical analog-to-digital converter principle," *IEEE International Symposium on Circuits and Systems,* Vol 1, pp. 432-435, 2001.

[97] H. Zmuda, E. N. Toughlian, G. Li, and P. LiKamWa, "A photonic wideband analog-to-digital converter," *IEEE Proceedings Aerospace Conference,* Vol 3, pp. 1461-1472, 2001.

[98] M. J. Hayduk, R. J. Bussjager, and M. A. Getbehead, "Photonic analog-to-digital conversion techniques using semiconductor saturable absorbers," *Proceedings of SPIE,* Vol 4042, pp. 54-60, 2000.

[99] H. Sakata, "Photonic analog-to-digital conversion by use of nonlinear Fabry–Perot resonators," *Applied Optics,* Vol 40, No 2, pp. 240-248, 2001.

[100] S. Oda, A. Maruta, and K. Kitayama, "All-optical quantization scheme based on fiber

nonlinearity," *IEEE Photonics Technology Letters,* Vol 16, No 2, pp. 587-589, 2004.

[101] S. Oda, and A. Maruta, "A novel quantization scheme by slicing supercontinuum spectrum for all-optical analog-to-digital conversion," *IEEE Photonics Technology Letters,* Vol 17, No 2, pp. 465-467, 2005.

[102] H. Taylor, "An optical analog-to-digital converter design and analysis," *IEEE Journal of Quantum Electronics,* Vol 15, No 4, pp. 210-216, 1979.

[103] J. Stigwall, and S. Galt, "Interferometric analog-to-digital conversion," *IEEE Photonics Technology Letters,* Vol 17, No 2, pp. 468-470, 2005.

[104] J. Stigwall, and S. Galt, "Demonstration and Analysis of a 40-Gigasample/s Interferometric Analog-to-Digital Converter," *IEEE Journal of Lightwave Technology,* Vol 24, No 3, pp. 1247-1256, 2006.

[105] M. Jarrahi, R. F. W. Pease, D. A. B. Miller, and T. H. Lee, "Optical Spatial Quantization for Higher Performance Analog-to-Digital Conversion," *IEEE Transactions on Microwave Theory and Techniques,* Vol 56, No 9, pp. 2143-2150, 2009.

[106] Ch. Fattinger, and D. Grischkowsky, "Terahertz beams," *Applied Physics Letters,* Vol 54, No 6, pp. 490-492, 1989.

[107] D. Krökel, D. Grischkowsky, and M. B. Ketchen, "Subpicosecond electrical pulse generation using photoconductive switches with long carrier lifetimes," *Applied Physics Letters,* Vol 54, No 11, pp. 1046-1047, 1989.

[108] M. van Exter, Ch. Fattinger, and D. Grischkowsky, "High-brightness terahertz beams characterized with an ultrafast detector," *Applied Physics Letters,* Vol 55, No 4, pp. 337-339, 1989.

[109] C. Jansen, S. Wietzke, O. Peters, M. Scheller, N. Vieweg, M. Salhi, N. Krumbholz, C. Jördens, T. Hochrein, and M.Koch, "Terahertz imaging: applications and perspectives," *Applied Optics,* Vol 49, No 19, pp. E48-57, 2010.

[110] P. U. Jepson, D. G. Cooke, and M. Koch, "Terahertz spectroscopy and imaging – Modern techniques and applications," *Laser & Photonics Reviews,* Vol 5, No 1, pp. 124-166, 2011.

[111] P. C. M. Planken, M. C. Nuss, I. Brener, and K. W. Goossen, "Terahertz Emission in Single Quantum Wells after Coherent Optical Excitation of Light Hole and Heavy Hole Excitons," *Physical Review Letters,* Vol 69, No 26, pp. 3800-3803, 1992.

[112] X. G. Peralta, S. J. Allen, M. C. Wanke, N. E. Narff, J. A. Simmons, M. P. Lilly, J. L. Reno, P. J. Burke, and J. P. Eisenstein, "Terahertz photoconductivity and plasmon modes in double-quantum-well field-effect transistors," *Applied Physics Letters,* Vol 81, No 9, pp. 1627-1629, 2002.

[113] H. C. Liu, C. Y. Song, A. J. SpringThorpe, and J. C. Cao, "Terahertz quantum-well photodetector," *Applied Physics Letters,* Vol 84, No 20, pp. 4068-4070, 2004.

[114] B. Williams, S. Kumar, Q. Hu, and J. Reno, "Operation of terahertz quantum-cascade lasers at 164 K in pulsed mode and at 117 K in continuous-wave mode," *Optics Express,* Vol 13, No 9, pp. 3331-3339, 2005.

[115] B. S. Williams, "Terahertz quantum-cascade lasers," *Nature Photonics,* Vol 1, No 9, pp. 517-525, 2007.

[116] H.-T. Chen, W. J. Padilla, J. M. O. Zide, A. C. Gossard, A. J. Taylor, and R. D. Averitt, "Active terahertz metamaterial devices," *Nature,* Vol 44, pp. 597-600, 2006.

[117] H.-T. Chen, W. J. Padilla, M. J. Cich, A. K. Azad, R. D. Averitt, and A. J. Taylor, "A metamaterial solid-state terahertz phase modulator," *Nature Photonics,* Vol 3, pp. 148-151, 2009.

[118] T. A. Ibrahim, W. Cao, Y. Kim, J. Li, J. Goldhar, P.-T. Ho, and C. H. Lee, "Lightwave Switching in Semiconductor Microring Devices by Free Carrier Injection," *Journal of Lightwave Technology,* Vol 21, No 12, pp. 2997-3003, 2003.

[119] Q. Xu, B. Schmidt, S. Pradhan, and M. Lipson, "Micrometre-scale silicon electro-optic modulator," *Nature,* Vol 435, pp. 325-327, 2005.

[120] Q. Xu, S. Manipatruni, B. Schmidt, J. Shakya, and M. Lipson, "12.5 Gbit/s carrier-injection-based silicon micro-ring silicon modulators," *Optics Express,* Vol 15, No 2, pp. 430-436, 2007.

[121] A. M. Gutierrez, A. Brimont, G. Rasigade, M. Ziebell, D. Marris-Morini, J.-M. Fédéli, L. Vivien, J. Marti, and P. Sanchis, "Ring-Assisted Mach–Zehnder Interferometer Silicon Modulator for Enhanced Performance," *Journal of Lightwave Technology,* Vol 30, No 1, pp. 9-14, 2012.

[122] S. Adachi, Optical Properties of Crystalline and Amorphous Semiconductors: Materials and Fundamental Principles, Kluwer Academic Publishers, 1999.

[123] S. Adachi, Optical Properties of Crystalline and Amorphous Semiconductors: Numerical

Data and Graphical Information, Kluwer Academic Publishers, 1999.

[124] M. Shur, Introduction to electronic devices, New York: John Wiley & Suns, 1996.

[125] J. R. Waldrop, "Schottky-barrier height of ideal metal contacts to GaAs," *Applied Physics Letter,* Vol 44, pp. 1002-1004, 1984.

[126] A. van der Ziel, "Infrared detection and mixing in heavily doped Schottky-barrier diodes," *Journal of Applied Physics,* Vol 47, No 5, pp. 2059-2068, 1976.

[127] K. S. Champlin, and G. Eisenstein, "Cutoff Frequency of Subrnillimeter Schottky-Barrier Diodes," *IEEE Transactions on Microwave Theory and Techniques,* Vol 26, No 1, pp. 31-34, 1978.

[128] Patrick G. O'Shea, and Henry P. Freund, "Free-electron lasers: status and applications," *Science,* Vol 292, No 5523, pp. 1853-1858, 2001.

[129] C. Vicario, B. Monoszlai, C. Ruchert, and C. P. Hauri, "High-Field Laser-Based Terahertz Source for Swiss-FEL," *PAC*, 2013.

[130] Masayoshi Tonouchi, "Cutting-edge terahertz technology," *Nature Photonics,* Vol 1, No 2, pp. 97-105, 2007.

[131] T. Kubacka, J. A. Johnson, M. C. Hoffmann, C. Vicario, S. De Jong, P. Beaud, S. Grübel et al., ""Large-amplitude spin dynamics driven by a THz pulse in resonance with an electromagnon," *Science,* Vol 343, No 6177, pp. 1333-1336, 2014.

[132] Ulrike Frühling, Marek Wieland, Michael Gensch, Thomas Gebert, Bernd Schütte, Maria Krikunova, Roland Kalms et al., "Single-shot terahertz-field-driven X-ray streak camera," *Nature Photonics,* Vol 3, No 9, pp. 523-528, 2009.

[133] M. C. Hoffmann, and J. J. Turner, "Ultrafast X-ray experiments using terahertz excitation," *Synchrotron Radiation News,* Vol 25, No 2, pp. 17-24, 2012.

[134] C. Vicario, C. Ruchert, and C. P. Hauri, "High field broadband THz generation in organic materials," *Journal of Modern Optics,* Vol 62, No 18, pp. 1480-1485, 2015.

[135] Wei Shi, Yujie J. Ding, Nils Fernelius, and Konstantin Vodopyanov, "Efficient, tunable, and coherent 0.18–5.27-THz source based on GaSe crystal," *Optics Letters,* Vol 27, No 16, pp. 1454-1456, 2002.

[136] H. Hirori, A. Doi, F. Blanchard, and K. Tanaka., "Single-cycle terahertz pulses with

amplitudes exceeding 1 MV/cm generated by optical rectification in LiNbO3," *Applied Physics Letters,* Vol 98, No 9, p. 091106, 2011.

[137] Mostafa Shalaby, Carlo Vicario, Karunanithi Thirupugalmani, Srinivasan Brahadeeswaran, and Christoph P. Hauri, "Intense THz source based on BNA organic crystal pumped at Ti: sapphire wavelength," *Optics Letters,* Vol 41, No 8, pp. 1777-1780, 2016.

[138] Wei Shi, and Yujie J. Ding, "A monochromatic and high-power terahertz source tunable in the ranges of 2.7–38.4 and 58.2–3540 μm for variety of potential applications," *Applied physics letters,* Vol 84, No 10, pp. 1635-1637, 2004.

[139] Yi Jiang, Da Li, Yujie J. Ding, and Ioulia B. Zotova, "Terahertz generation based on parametric conversion: from saturation of conversion efficiency to back conversion," *Optics Letters,* Vol 36, No 9, pp. 1608-1610, 2011.

[140] A. Majkić, M. Zgonik, A. Petelin, M. Jazbinšek, B. Ruiz, C. Medrano, and P. Günter., "Terahertz source at 9.4 THz based on a dual-wavelength infrared laser and quasi-phase matching in organic crystals OH1," *Applied Physics Letters,* Vol 105, No 14, p. 141115, 2014.

[141] J. Kiessling, I. Breunig, P. G. Schunemann, K. Buse, and K. L. Vodopyanov., "High power and spectral purity continuous-wave photonic THz source tunable from 1 to 4.5 THz for nonlinear molecular spectroscopy," *New Journal of Physics,* Vol 15, No 10, p. 105014, 2013.

[142] F. Teppe, W. Knap, D. Veksler, M. S. Shur, A. P. Dmitriev, V. Yu. Kachorovskii, and S. Rumyantsev, "Room-temperature plasma waves resonant detection of sub-terahertz radiation by nanometer field-effect transistor," *Applied Physics Letters,* Vol 87, p. 052107, 2005.

[143] W. Knap, M. Dyakonov, D. Coquillat, F. Teppe, N. Dyakonova, J. Lusakowski, K. Karpierz, M. Sakowicz, G. Valusis, D. Seliuta, I. Kasalynas, A. El Fatimy, Y. M. Meziani, and T. Otsuji, "Field Effect Transistors for Terahertz Detection: Physics and First Imaging Applications," *Journal of Infrared, Millimeter and Terahertz Waves,* Vol 30, pp. 1319-1337, 2009.

[144] W. Stillman, F. Guarin, V. Yu. Kachorovskii, N. Pala, S. Rumyantsev, M.S. Shur and D. Veksler, "Nanometer Scale Complementary Silicon MOSFETs as Detectors of Terahertz and Sub-terahertz Radiation," *6th IEEE Sensors Conference,* Vol %1，共 %2 Vol1-3, pp. 934-937, 2007.

[145] Wojciech Knap, Mikhail Dyakonov, Dominique Coquillat, Frederic Teppe, Nina Dyakonova, Jerzy Lusakowski, Krzysztof Karpierz, Maciej Sakowicz, Gintaras Valusis, Dalius Seliuta, Irmantas Kasalynas, Abdelouahad El Fatimy, Y. M. Meziani, Taiichi Otsuji, "Field Effect Transistors for Terahertz Detection: Physics and First Imaging Applications," *J. Infrared Milli. Terahz. Waves,* Vol 30, pp. 1319-1337, 2009.

[146] A. Lisauskas, W. von Spiegel, S. Boubanga-Tombet, A. El Fatimy, D. Coquillat, F. Teppe, N. Dyakonova, W. Knap and H.G. Roskos, "Terahertz imaging with GaAs field-effect transistors," *Electronics Letters,* Vol 44, No 6, pp. 408-409, 2008.

[147] L. Vicarelli, M. S. Vitiello, D. Coquillat, A. Lombardo, A. C. Ferrari, W. Knap, M. Polini, V. Pellegrini & A. Tredicucci, "Graphene field-effect transistors as room-temperature terahertz detectors," *Nature Materials,* Vol 11, pp. 865-871, 2012.

[148] R. Tauk, F. Teppe, S. Boubanga, D. Coquillat, W. Knap, Y. M. Meziani, C. Gallon, F. Boeuf, T. Skotnicki, C. Fenouillet-Beranger, D. K. Maude, S. Rumyantsev, and M. S. Shur, "Plasma wave detection of terahertz radiation by silicon field effects transistors_Responsivity and noise equivalent power," *Applied Physics Letters,* Vol 89, No 25, p. 253511, 2006.

[149] Alvydas Lisauskas, Ullrich Pfeiffer, Erik Öjefors, Peter Haring Bolìvar, Diana Glaab, and Hartmut G. Roskos, "Rational design of high-responsivity detectors of terahertz radiation based on distributed self-mixing in silicon field-effect transistors," *Journal of Applied Physics,* Vol 105, No 11, p. 114511, 2009.

[150] Miriam S. Vitiello, Dominique Coquillat, Leonardo Viti, Daniele Ercolani, Frederic Teppe, Alessandro Pitanti, Fabio Beltram, Lucia Sorba, Wojciech Knap, and Alessandro Tredicucci, "Room-Temperature Terahertz Detectors Based on Semiconductor Nanowire Field-Effect Transistors," *Nano Letters,* Vol 12, No 1, pp. 96-101, 2012.

[151] S. Nadar, H. Videlier, D. Coquillat, F. Teppe, M. Sakowicz, N. Dyakonova, W. Knap, D. Seliuta, I. Kašalynas, and G. Valušis, "Room temperature imaging at 1.63 and 2.54 THz with field effect transistor detectors," *Journal of Applied Physics,* Vol 108, No 5, p. 054508, 2010.

[152] C. Drexler, N. Dyakonova, P. Olbrich, J. Karch, M. Schafberger, K. Karpierz, Yu. Mityagin, M. B. Lifshits, F. Teppe, O. Klimenko, Y. M. Meziani, W. Knap, and S. D. Ganichev, "Helicity sensitive terahertz radiation detection by field effect transistors," *Journal of Applied Physics,* Vol 111, No 12, p. 124504, 2012.

[153] R. Tsu and L. Esaki, "Tunneling in a finite superlattice," *Applied Physics Letters,* Vol 22,

No 11, pp. 562-564, 1973.

[154] Jian Ping Sun, George I. Haddad, Pinaki Mazumder, and Joel N. Schulman, "Resonant Tunneling Diodes: Models and Properties," *Proceedings of the IEEE,* Vol 86, No 4, pp. 641-660, 1998.

[155] Michael Feiginov, Cezary Sydlo, Oleg Cojocari, and Peter Meissner, "Resonant-tunnelling-diode oscillators operating at frequencies above 1.1 THz," *Applied Physics Letters,* Vol 99, No 23, p. 233506, 2011.

[156] T. Maekawa, H. Kanaya, S. Suzuki, and M. Asada, "Frequency increase in terahertz oscillation of resonant tunnelling diode up to 1.55 THz by reduced slot-antenna length," *Electronics Letters,* Vol 50, No 17, p. 1214, 2014.

[157] Michael N. Feiginov, H. Kanaya, S. Suzuki, and M. Asada, "Operation of resonant-tunneling diodes with strong back injection from the collector at frequencies up to 1.46 THz," *Applied Physics Letters,* Vol 104, No 24, p. 243509, 2014.

[158] M. N. Feiginov, "Does the quasibound-state lifetime restrict the high-frequency operation of resonant-tunnelling diodes?," *Nanotechnology,* Vol 11, No 4, p. 359, 2000.

[159] Michael N. Feiginov, and Dibakar Roy Chowdhury, "Operation of resonant-tunneling diodes beyond resonant-state-lifetime limit," *Applied Physics Letters,* Vol 91, No 20, p. 203501, 2007.

[160] S. Suzuki, M. Asada, A. Teranishi, H. Sugiyama, and H. Yokoyama, "Fundamental oscillation of resonnat tunneling diodes above 1 THz at room temperature," *Applied Physics Letters,* Vol 97, No 24, p. 242102, 2010.

[161] Y. Koyama, R. Sekiguchi, and T. Ouchi, "Oscillation up to 1.40 THz from resonant-tunneling-diode-based oscillators with integrated patch antennas," *Applied Physics Express,* Vol 6, p. 064102, 2013.

[162] H. Kanaya, R. Sogabe, T. Maekawa, S. Suzuki, and M. Asada, "Fundamental oscillation up to 1.42 THz in resonant tunneling diodes by optimized collector spacer thickness," *Journal of Infrared, Millimeter and Terahertz Waves,* Vol 35, pp. 425-431, 2014.

[163] Sebastian Diebold, Shunsuke Nakai, Kousuke Nishio, Jaeyoung Kim, Kazuisao Tsuruda, Toshikazu Mukai, Masayuki Fujita, and Tadao Nagatsuma, "Modeling and Simulation of Terahertz Resonant Tunneling Diode-Based Circuits," *IEEE Transactions on Terahertz Science and Technology,* Vol 6, No 5, pp. 716-723, 2016.

[164] W. Knap, V. Kachorovskii, Y. Deng, S. Rumyantsev, J-Q. Lü, R. Gaska, M. S. Shur et al, "Nonresonant detection of terahertz radiation in field effect transistors," *Journal of Applied Physics,* Vol 91, No 11, pp. 9346-9353, 2002.

[165] Berardi Sensale-Rodriguez, Lei Liu, Ronghua Wang, Tom Zimmermann, Patrick Fay, Debdeep Jena, and Huili Xing, "FET THz detectors operating in the quantum capacitance limited region," *International Journal of High Speed Electronics and Systems,* Vol 20, No 3, pp. 597-609, 2011.

[166] V. Ryzhii, I. Khmyrova, and M. Shur, "Resonant detection and frequency multiplication of terahertz radiation utilizing plasma waves in resonant-tunneling transistors," *Journal of Applied Physics,* Vol 88, No 5, pp. 2868-2871, 2000.

[167] Victor Ryzhii, and Michael Shur, "Plasma instability and nonlinear terahertz oscillations in resonant-tunneling structures," *Japanese Journal of Applied Physics,* Vol 40, pp. 546-550, 2001.

[168] Berardi Sensale-Rodriguez, Lei Liu, Patrick Fay, Debdeep Jena, and Huili Grace Xing, "Power amplification at THz via plasma wave excitation in RTD-gated HEMTs," *IEEE Transactions on Terahertz Science and Technology,* Vol 3, No 2, pp. 200-206, 2013.

[169] Hugo O. Condori Quispe, Jimy J. Encomendero-Risco, Huili Grace Xing, and Berardi Sensale-Rodriguez, "Terahertz amplification in RTD-gated HEMTs with a grating-gate wave coupling topology," *Applied Physics Letter,* Vol 109, No 6, p. 063111, 2016.

[170] A. B. Kuzmenko, Erik Van Heumen, Fabrizio Carbone, and Dirk Van Der Marel, "Universal optical conductance of graphite," *Physical review letters,* Vol 100, No 11, p. 117401, 2008.

[171] Alexander S. Mayorov, Roman V. Gorbachev, Sergey V. Morozov, Liam Britnell, Rashid Jalil, Leonid A. Ponomarenko, Peter Blake et al, "Micrometer-scale ballistic transport in encapsulated graphene at room temperature," *Nano letters,* Vol 11, No 6, pp. 2396-2399, 2011.

[172] Jian-Hao Chen, Chaun Jang, Shudong Xiao, Masa Ishigami, and Michael S. Fuhrer, "Intrinsic and extrinsic performance limits of graphene devices on SiO2," *Nature nanotechnology,* Vol 4, No 206-209, p. 3, 2008.

[173] A. M. Song, M. Missous, Pär Omling, A. R. Peaker, Lars Samuelson, and Werner Seifert, "Unidirectional electron flow in a nanometer-scale semiconductor channel: A self-switching device," *Applied physics letters,* Vol 83, No 9, pp. 1881-1883, 2003.

[174] Claudio Balocco, Shahrir R. Kasjoo, Xiaofeng F. Lu, Linqing Q. Zhang, Yasaman Alimi, Stephan Winnerl, and Aimin M. Song, "Room-temperature operation of a unipolar nanodiode at terahertz frequencies," *Applied physics letters,* Vol 98, No 22, p. 223501, 2011.

[175] Kwangsik Choi, Geunmin Ryu, Filiz Yesilkoy, Athanasios Chryssis, Neil Goldsman, Mario Dagenais, and Martin Peckerar, "Geometry enhanced asymmetric rectifying tunneling diodes," *Journal of vacuum science & technology. B, Microelectronics and nanometer structures,* Vol 28, No 6, p. C6O50, 2010.

[176] Ragnar Fleischmann, and Theo Geisel, "Mesoscopic rectifiers based on ballistic transport," *Physical review letters,* Vol 89, No 1, p. 016804, 2002.

[177] George W Hanson , "Dyadic Green's functions and guided surface waves for a surface conductivity model of graphene," *Journal of Applied Physics,* Vol 103, No 6, p. 064302, 2008.

[178] Mircea Dragoman, Martino Aldrigo, Adrian Dinescu, Daniela Dragoman, and Alessandra Costanzo, "Towards a terahertz direct receiver based on graphene up to 10 THz," *Journal of Applied Physics,* Vol 115, No 4, p. 044307, 2014.

[179] Daniela Dragoman, and Mircea Dragoman, "Geometrically induced rectification in two-dimensional ballistic nano devices," *Journal of Physics D: Applied Physics,* Vol 46, No 5, p. 055306, 2013.

[180] Zixu Zhu, Saumil Joshi, and Garret Moddel, "High Performance Room Temperature Rectenna IR Detectors Using Graphene Geometric Diodes," *IEEE Journal of Selected Topics in Quantum Electronics,* Vol 20, No 6, pp. 70-78, 2014.

[181] L Friedman, Greg Sun, and Richard A. Soref, "SiGe/Si THz laser based on transitions between inverted mass light-hole and heavy-hole subbands," *Applied Physics Letters,* Vol 78, No 4, pp. 401-403, 2001.

[182] Rüdeger Köhler, Alessandro Tredicucci, Fabio Beltram, Harvey E. Beere, Edmund H. Linfield, A. Giles Davies, and David A. Ritchie, "High-intensity interminiband terahertz emission from chirped superlattices," *Applied Physics Letters,* Vol 80, p. 1867, 2002.

[183] V. G. Dmitriev, G. G. Gurzadyan, and D. N. Nikogosyan, Handbook of Nonlinear Crystals, Berlin: Springer-Verlag, 1999.

[184] F. Sizova, and A. Rogalski, "THz detectors," *Progress in Quantum Electronics,* Vol 34,

No 5, pp. 278-347, 2010.

[185] R. Lai, X. B. Mei, W.R. Deal, W. Yoshida, Y. M. Kim, P.H. Liu, J. Lee, J. Uyeda, V. Radisic, M. Lange, T. Gaier, L. Samoska, and A. Fung, "Sub 50 nm InP HEMT Device with Fmax Greater than 1 THz," *IEEE International Electron Devices Meeting,* pp. 609-611, 2007.

[186] W. R. Deal, X. B. Mei, V. Radisic, K. Leong, S. Sarkozy, B. Gorospe, J. Lee, P. H. Liu, W. Yoshida, J. Zhou, M. Lange, J. Uyeda, and R. Lai, "Demonstration of a 0.48 THz amplifier module using InP HEMT transistors," *IEEE Microwave and Wireless Components Letters,* Vol 20, No 5, pp. 289-291, 2010.

[187] W. R. Deal, K. Leong, V. Radisic, S. Sarkozy, B. Gorospe, J. Lee, P. H. Liu, W. Yoshida, J. Zhou, M. Lange, R. Lai, and X. B. Mei, "Low noise amplification at 0.67 THz using 30 nm InP HEMTs," *IEEE Microwave and Wireless Components Letters,* Vol 21, No 7, pp. 368-370, 2011.

[188] W. Stillman, F. Guarin, V. Yu. Kachorovskii, N. Pala, S. Rumyantsev, M.S. Shur, and D. Veksler, "Nanometer Scale Complementary Silicon MOSFETs as Detectors of Terahertz and Sub-terahertz Radiation," *6th IEEE Sensors Conference,* Vol %1，共 %2 Vol1-3, pp. 934-937, 2007.

[189] V. R. Almeida, C. A. Barrios, R. R. Panepucci, and M. Lipson, "All-optical control of light on a silicon chip," *Nature,* Vol 431, pp. 1081-1084, 2004.

[190] Q. Xu, and M. Lipson, "All-optical logic based on silicon micro-ring resonators," *Optics Express,* Vol 15, No 3, pp. 924-929, 2007.

[191] Y. Zhang, Y. Zhang, and B. Li, "Optical switches and logic gates based on self-collimated beams in two-dimensional photonic crystals," *Optics Express,* Vol 15, No 15, pp. 9287-9292, 2007.

[192] J. Xu, X. Zhang, Y. Zhang, J. Dong, D. Liu, and D. Huang, "Reconfigurable all-optical logic gates for multi-input differential phase-shift keying signals Design and experiments," *Journal of Lightwave Technology,* Vol 27, No 23, pp. 5268-5275, 2009.

[193] H. Wei, Z. Wang, X. Tian, M. Käll, and H. Xu, "Cascaded logic gates in nanophotonic plasmon networks," *Nature Communications,* Vol 2, p. 387, 2011.

[194] Y. Fu, X. Hu, C. Lu, S. Yue, H. Yang, and Q. Gong, "All-optical logic gates based on nanoscale plasmonic slot waveguides," *Nano Letters,* Vol 12, No 11, pp. 5784-5790, 2012.

[195] J. Hardy, and J. Shamir, "Optics inspired logic architecture," *Optics Express,* Vol 15, No 1, pp. 150-165, 2007.

[196] A. I. Zavalin, J. Shamir, C. S. Vikram, and H. J. Caulfield, "Achieving stabilization in interferometric logic operations," *Applied Optics,* Vol 45, No 2, pp. 360-365, 2006.

[197] Y. A. Zaghloul, and A. R. M. Zaghloul, "Complete all-optical processing polarization-based binary logic gates and optical processors," *Optics Express,* Vol 14, No 21, pp. 9879-9895, 2006.

[198] J. N. Roy, and D. K. Gayen, "Integrated all-optical logic and arithmetic operations with the help of a TOAD-based interferometer device—alternative approach," *Applied Optics,* Vol 46, No 22, pp. 5304-5310, 2007.

[199] J. N. Roy, "Mach–Zehnder interferometer-based tree architecture for all-optical logic and arithmetic operations," *Optik,* Vol 120, No 7, pp. 318-324, 2009.

[200] D. K. Gayen, J. N. Roy, C. Taraphdar, and R. K. Pal, "All-optical reconfigurable logic operations with the help of terahertz optical asymmetric demultiplexer," *Optik,* Vol 122, No 8, pp. 711-718, 2011.

[201] Q. Xu, and R. Soref, "Reconfigurable optical directed-logic circuits using microresonator-based optical switches," *Optics Express,* Vol 19, No 6, pp. 5244-5259, 2011.

[202] J. Wang, E. Katz, "Digital biosensors with built-in logic for biomedical applications—biosensors based on a biocomputing concept," *Analytical and Bioanalytical Chemistry,* Vol 398, pp. 1591-1603, 2010.

[203] Y. Jia, R. Duan, F. Hong, B. Wang, N. Liu, F. Xia, "Electrochemical biocomputing: a new class of molecular-electronic logic devices," *Soft Matter,* Vol 9, pp. 6571-6577, 2013.

[204] K. Song, and P. Mazumder, "Active Terahertz Spoof Surface Plasmon Polariton Switch Comprising the Perfect Conductor Metamaterial," *IEEE Transactions on Electron Devices,* Vol 56, pp. 2792-2799, 2009.

[205] J. Wang, and E. Katz, "Digital biosensors with built-in logic for biomedical applications—biosensors based on a biocomputing concept," *Analytical and Bioanalytical Chemistry,* Vol 398, pp. 1591-1603, 2010.

[206] Y. Jia, R. Duan, F. Hong, B. Wang, N. Liu, and F. Xia, "Electrochemical biocomputing: a new class of molecular-electronic logic devices," *Soft Matter,* Vol 9, pp. 6571-6577, 2013.

[207] Yanjun Ma, Mengchen Huang, Sangwoo Ryu, Chung Wung Bark, Chang-Beom Eom, Patrick Irvin, and Jeremy Levy, "Broadband terahertz generation and detection at 10 nm scale," *Nano Letters,* Vol 13, No 6, pp. 2884-2888, 2013.

[208] Y. He, J.-Y. Chen, J. R. Knab, W. Zheng, and A. G. Markelz, "Evidence of Protein Collective Motions on the Picosecond Timescale," *Biophysical Journal,* Vol 100, pp. 1058-1065, 2011.

[209] N. Rodríguez-Ezpeleta, M.Hackenber, A. M. Aransay, Bioinformatics for High Throughput Sequencing, Springer, 2012.